Helsinki University of Technology Laboratory of Space Technology Publications
Teknillisen korkeakoulun Avaruustekniikan laboratorion julkaisuja
Espoo 2007 REPORT 70

Development, Calibration and Applications of Polarimetric Microwave Radiometers for Remote Sensing

Andreas Colliander

Dissertation for the degree of Doctor of Science in Technology to be presented with due permission of the Department of Electrical Engineering, for public examination and debate in Auditorium S4 at Helsinki University of Technology (Espoo, Finland) on the 26th of October, 2007, at 12 noon.

Helsinki University of Technology
Department of Electrical and Communications Engineering
Laboratory of Space Technology

Teknillinen korkeakoulu
Sähkö- ja tietoliikennetekniikan osasto
Avaruustekniikan laboratorio

Distribution:
Helsinki University of Technology
Laboratory of Space Technology
P.O.Box 3000
FIN-02015 TKK
Finland

Tel. +358 9 451 2378
Fax +358 9 451 2898

Email: andreas.colliander@tkk.fi
http://www.space.tkk.fi

ISBN-978-951-22-8895-3 (printed)
ISBN-978-951-22-8896-0 (electronic)
ISSN 0786-8154

Picaset Oy
Helsinki 2007

ABSTRACT OF DOCTORAL DISSERTATION	HELSINKI UNIVERSITY OF TECHNOLOGY P.O. BOX 1000, FI-02015 TKK http://www.tkk.fi

Author Andreas Colliander

Name of the dissertation
Develpoment, Calibration and Applications of Polarimetric Radiometers for Remote Sensing

Manuscript submitted 5.2.2007	Manuscript revised 22.7.2007

Date of the defence 26.10.2007

☐ Monograph	☒ Article dissertation (summary + original articles)

Department	Department of Electrical and Communications Engineering
Laboratory	Laboratory of Space Technology
Field of research	Space Technology, Microwave Remote Sensing
Opponent(s)	Dr. David Le Vine, NASA Goddard Space Flight Center, USA
Supervisor	Prof. Martti Hallikainen
Instructor	Prof. Martti Hallikainen

Abstract

This doctoral thesis describes (1) the development and calibration principles of a fully polarimetric radiometer, which is developed for the reference radiometer of a spaceborne synthetic aperture radiometer; (2) a study of an improvement of the most important application of the polarimetric radiometry, maritime wind vector measurement; (3) and a numerical simulation method for modeling the electromagnetic radiation from ocean surface.

The fundamental part of passive microwave remote sensing is the development of the measurement instruments, radiometers. Over the past two decades significant amount of work has been focused on the development of so-called interferometric synthetic aperture radiometry. The first spaceborne radiometer using aperture synthesis is scheduled for launch in 2008. This radiometer operates at 1.4 GHz and aims for global measurement of soil moisture and ocean salinity; hence, the mission is named as SMOS. This radiometer and its airborne prototype use reference radiometers for calibration purposes. The development and calibration of both of these polarimetric reference radiometers is described in this work; they provide accurate enough measurements to calibrate the noise distribution network and absolute average brightness temperature, while being a part of the receiver constellation of the synthetic aperture radiometer.

For the applications of polarimetric radiometry, the main focus over the past two decades has been the measurement of the maritime wind vector. In this work, a set of measurements is analyzed in order to solve the incidence angle dependency of the wind vector measurements. The results show clear dependency for all measured parameters, and a model for the dependency is introduced. As a part of this study, a theoretical method for calculation of scattering from dielectric rough surface, like ocean surface, was also developed. This method can be used for simulation of the wind vector measurements in any kind of ocean surface conditions. The feasibility and efficiency of the method for this purpose is demonstrated.

Keywords polarimetric radiometry, radiometer, calibration, remote sensing, wind, rough surface scattering

ISBN (printed) 978-951-22-8895-3	ISSN (printed) 0786-8154
ISBN (pdf) 978-951-22-8896-0	ISSN (pdf)
Language English	Number of pages 128

Publisher Helsinki University of Technology / Laboratory of Space Technology

Print distribution Helsinki University of Technology / Laboratory of Space Technology

☒ The dissertation can be read at http://lib.tkk.fi/Diss/

VÄITÖSKIRJAN TIIVISTELMÄ	TEKNILLINEN KORKEAKOULU PL 1000, 02015 TKK http://www.tkk.fi

Tekijä Andreas Colliander

Väitöskirjan nimi

Polarimetristen mikroaaltoradiometrien kehittäminen, kalibrointi sekä sovellukset kaukokartoitukseen

Käsikirjoituksen päivämäärä 5.2.2007	Korjatun käsikirjoituksen päivämäärä 22.7.2007

Väitöstilaisuuden ajankohta 26.10.2007

☐ Monografia	☒ Yhdistelmäväitöskirja (yhteenveto + erillisartikkelit)

Osasto	Sähkö- ja tietoliikennetekniikan osasto
Laboratorio	Avaruustekniikan laboratorio
Tutkimusala	Avaruustekniikka, Mikroaaltokaukokartoitus
Vastaväittäjä(t)	Tri David Le Vine, NASA Goddard Space Flight Center, USA
Työn valvoja	Prof. Martti Hallikainen
Työn ohjaaja	Prof. Martti Hallikainen

Tiivistelmä

Tämä väitöskirja kuvaa polarimetrisen radiometrin kehittämisen ja kalibrointiperiaatteet. Radiometeri toimii avaruuskäyttöisen synteettisen apertuurin radiometrin referenssiradiometrinä. Lisäksi väitöskirjassa kuvataan tärkeimmän polarimetrisen radiometrian sovelluskohteen, merialueiden tuulivektorimittauksen, parannuksen, sekä uuden numeerisen simulointimenetelmän merenpinnan sironnalle tuulivektorimittauksen jatkokehitykseen.

Yksi passiivisen mikroaaltokaukokartoituksen tärkeimmistä asioista on mittauslaitteiden, eli radiometrien, kehittäminen. Synteettisen apertuurin interferometristen radiometrien kehittämiseen on panostettu huomattavasti viimeisen kahden vuosikymmenen aikana. Ensimmäinen avaruuskäyttöinen synteettisen apertuurin radiometri laukaistaan vuonna 2008. Tämä interferometrinen radiometri toimii 1,4 GHz taajudellla ja sillä on tarkoitus mitata maan kosteutta sekä merenpinnan suolaisuutta. Tästä tulee nimi SMOS (Soil Moisture and Ocean Salinity). Interferometrinen radiometri ja sen lentokäyttöinen prototyyppi käyttävät kalibrointiin referenssiradiometria. Näiden referenssiradiometrien kehittäminen sekä kalibrointi kuvataan tässä työssä. Niillä voidaan mitata tarkasti interferometrisen radiometrin sisäinen kohinalähde ja vastaanotettu keskimääräinen säteily sekä ne voivat toimia osana interferometristä mittausta.

Polarimetrisen radiometrian sovellusten kehityksen pääpaino viimeisen kahden vuosikymmenen aikana on ollut merialueiden tuulivektorimittauksessa. Tässä työssä lentomittauksissa kerätystä mittausaineistosta on määritetty tuulivektorimittauksen riippuvuutta mittauskulmasta. Tulokset osoittavat selvää riippuvuutta kaikille mitatuille parametreille. Työssä esitetään malli tämän riippuvuuden huomioonottamiseen. Tuulivektorimittauksen jatkokehitystä varten työssä on myös kehitetty uusi numeerinen menetelmä, jota voidaan käyttää merenpinnan mittauksen simuloimiseen. Tämä menetelmä on osoitettu tarkaksi ja erittäin tehokkaaksi.

Asiasanat polarimetrinen radiometria, radiometri, kalibrointi, kaukokartoitus, tuuli, karkean pinnan sironta

ISBN (painettu)	978-951-22-8895-3	ISSN (painettu)	0786-8154
ISBN (pdf)	978-951-22-8896-0	ISSN (pdf)	
Kieli	Englanti	Sivumäärä	128

Julkaisija Teknillinen korkeakoulu / Avaruustekniikan laboratorio

Painetun väitöskirjan jakelu Teknillinen korkeakoulu / Avaruustekniikan laboratorio

☒ Luettavissa verkossa osoitteessa http://lib.tkk.fi/Diss/

PREFACE

The work presented in this Doctoral Thesis has been carried out in the Laboratory of Space Technology of the Helsinki University of Technology under the supervision of Professor Martti Hallikainen. The work was conducted in the frame of European Space Agency's (ESA) MDPP-2 project (MIRAS Demonstrator Pilot Project 2) and SMOS Payload Module project, Phases B and C/D (Soil Moisture and Ocean Salinity), and Academy of Finland's EMRES project (Electromagnetic Modeling of the Earth's Surface and Atmospheric Targets for Microwave Remote Sensing). Additionally, the work was supported by the National Graduate School for Remote Sensing (was funded by Academy of Finland and Finnish ministry of education), and also, in form of grants, by Ulla Tuominen, Jenny and Antti Wihuri, Walter Ahlström and Finnish Cultural Foundations.

Essentially, my work for this Thesis was divided in two parts: the first part concerns the reference, or zero-baseline, radiometer developed for the MIRAS instrument (Microwave Imaging Radiometer using Aperture Synthesis), the payload of the SMOS mission, and the second part concerns passive polarimetric remote sensing of oceans. For the first part, the SMOS mission has worked as a great inspiration for me personally. Having the chance to be part of the development of a satellite instrument, all the way from the prototyping to the flight model, was professionally very fulfilling experience. On the other hand, the more scientific second part, gave me an opportunity to see and explore the possibilities on the data analysis and theoretical side of microwave remote sensing.

I have been working with a great number of great people during the close-to 5-year period I used for the work presented in this Thesis. To be more presice, I started the work already in the frame of my Master's Thesis in 2001, when I was hired to the Laboratory by Prof. Hallikainen to work on the MDPP-2 project. At that time Mr. Simo Tauriainen was managing the project, and after his attention was more critically required in the operation of the Laboratory's aircraft, more responsibilites flowed in my direction. In MDPP-2, the team was composed of, besides Simo and me, Mr. Tuomo Auer from the Laboratory, Mr. Josu Uusitalo from Ylinen, and Mr. Martti Toikka from Toikka Oy. I owe deep gratitude to these individuals for the success we have had with the developed prototype, and without the team, the work could have never been accomplished.

Following MDPP-2, the Laboratory signed a contract for supporting the development of the reference radiometer, or Noise Injection Radiometer Subsystem, first in Phase B and then in Phase C/D of the SMOS Payload Module project. The support included reviewing the prototyped design, developing the calibration and test plan, carrying out the tests and implementing the control chip. My duties consisted of all these and project managing, excluding the implementation of the control chip, which was a feat for Mr. Aleksi Aalto, who ruled the task. In addition to Aleksi and me, the team for

Phases B and C/D consisted of Mr. Tuomo Auer, Mr. Jani Suomela, Mr. Jani Kettunen, Ms. Katriina Veijola, Mr. Pasi Vormisto and Mr. Kimi Forsberg. Again, without the team my work would have been impossible. And furthermore, as the team made my work very easy as a project manager in an extremely challenging project in many respects, therefore leaving me time for doing research, my gratitude is on the absolutely highest level!

Most of the duration of Phases B and C/D the Laboratory acted as a subcontractor for a Finnish company called Ylinen, which was responsible for the design, manufacturing and product assurance of the subsystem. Our co-operation was very close, and I had the pleasure to work with Dr. Janne Lahtinen, Mr. Ville Kangas, Mr. Lasse Ruokokoski, Ms. Heli Greus and Mr. Mikael Levander. I want to extend a big thank you to these people for the co-operation – the completion of this subsystem was a significant achievement by all of us!

The prime contractor in MDPP-2 and SMOS Phase B and Phase C/D was EADS-CASA Espacio from Spain. From this company, at the far corner of Europe, I would like to specially thank Mr. Marc Bergada, Mr. Joan Capdevila, Mr. Javier Benito, Mr. Andres Solana and Mr. Andres Borges. On the other hand, our work was naturally supervised by ESA, the funding agency, and there the father of MIRAS, Dr. Manuel Martin-Neira, provided, literally, an infinite amount of comments helping my work to a success; there would have been no substitution for Manuel! Also another man from ESA had an especially positive impact on my work, by extending his support to and confidence in me, SMOS Payload Manager Mr. Kevin McMullan – Thank You!

Within the frame of airborne campaigns flown using the Laboratory's aircraft in 2003 and 2004, I had again the pleasure to work with Simo. The successful measurements carried out with the polarimetric radiometer, designed by Dr. Janne Lahtinen, was a group effort by, in addition to Simo (and his unrivaled piloting skills), Janne and me, Mr. Jörgen Pihlflyckt, Mr. Juha Lemmetyinen, and Mr. Anselmi Pyy. My special thanks go to Janne, who performed the preprocessing of the data and helped in the analysis of the results.

In 2003, I attended Professor Jukka Sarvas' integral equation course, which inspired me to pursue the calculation of rough sourface scattering for the simulation of the response of the abovementioned airborne measurements. I am grateful that Prof. Sarvas very generously supervised an exercise aiming for this, and then later on assigned Dr. Pasi Ylä-Oijala to work with me in the frame of EMRES project. I would like to thank Pasi for his great assistance and patience in carrying out this work, which was many times pushed down on the priority list by the SMOS project.

As stated above, my work for this Thesis was performed in the Laboratory of Space Technology in TKK. I enjoyed tremendously working in the Laboratory. In addition to those mentioned above, I would like to especially recognize the following individuals from the Laboratory for their help and company: Prof. Jouni Pulliainen, Mr. Kimmo Rautiainen, Mr. Kari Luojus, Mr. Juha Kainulainen, Mr. Pekka

Rummukainen, Mr. Sami Kemppainen, Mr. Jaan Praks, Mr. Matias Takala, Dr. Marko Mäkynen, Dr. Sampsa Koponen, Mr. Teemu Tares and Mr. Mike Laaksonen. And of course, I would like to express my gratitude to secretaries Irja Kurki and Irma Planman for making many practical issues very easy for me to handle.

Finally, I would like to thank my supervisor Prof. Hallikainen for giving me this opportunity and his support for carriying out this work. And naturally, the pre-examiners Professors Niels Skou and Christopher Ruf and the opponent Dr. David Le Vine are acknowledged for reviewing and commenting the Thesis. Furthermore, thanks to the twenty or so editors and reviewers who gave their time and effort for the review process of the appended papers.

I consider myself as a very lucky person, to have had the opportunity to work with such a great individuals during the past five years, unfortunately not all mentioned here, in such interesting projects. But even luckier I felt in 2004 when I met my wife-to-be; Katri changed my life and never left, nor will leave, my thoughts – no matter how interesting things might seemingly get…

Leiden, the Netherlands, August 22, 2007

Andreas Colliander

TABLE OF CONTENTS

LIST OF ACRONYMS AND SYMBOLS

Acronyms

2-D	Two-Dimensional
3-D	Three-Dimensional
AIM	Adaptive Integral Method
AMIRAS	Airborne MIRAS
BSC	Bistatic Scattering Coefficient
CDTI	Centro para el Desarrollo Tecnológico Industrial
CFIE	Combined Field Integral Equation
CNES	Centre National D’Etudes Spatiales
EBM	Elektrobit Microwave
EFIE	Electrical Integral Equation
EM	Engineering Model
ESA	European Space Agency
ESTAR	Electronically Steered Thinned Array Radiometer
FFT	Fast Fourier Transform
FM	Flight Model
FPGA	Field Programmable Gate Array
FPoR	TKK Fully Polarimetric Radiometer
GEO	Geosynchronous Earth Orbit
GMRES	Generalized Residual method
HUT-2D	TKK 2-dimensional interferometric radiometer
HUTRAD	TKK multi-frequency radiometer
IF	Intermediate Frequency
JPL	Jet Propulsion Laboratory
LEO	Low Earth Orbit
LICEF	Light-weight Cost-effective Receiver
LINP	Length of Injection Noise Pulse
MDPP-2	MIRAS Demonstrator Pilot Project 2
MFIE	Magnetic Field Integral Equation
MIRAS	Microwave Imaging Radiometer using Aperture Synthesis
NDN	Noise Distribution Network
NIR	Noise Injection Radiometer
NOAA	National Oceanic and Atmospheric Administration (USA)
NRL	Naval Research Laboratory (USA)
RCS	Radar Cross Section
RF	Radio Frequency
RMS	Root Mean Square
RWG	Rao-Wilton-Glisson
SMCG	Sparse Matrix Canonical Grid
SMFIE	Single Magnetic Field Integral Equation

SMOS	Soil Moisture and Ocean Salinity
SRI	Space Research Institute (Russia)
TKK	Helsinki University of Technology
TUD	Technical University of Denmark

Symbols

γ_{pq}	Scattering coefficient of incident and reflected polarization *p* and *q* [-]
Δf	Frequency range, bandwidth [Hz]
$\Delta\eta$	Difference of noise injection, when add-on noise is on and off [-]
$\Delta\Theta$	*H-V* phase imbalance of front-end [deg]
ΔT	Difference of noise temperature, when add-on noise is on and off [-]
ΔT_A	Radiometric resolution [K]
ΔT_G	Radiometric error caused by gain fluctuations [K]
$\varepsilon_1 , \varepsilon_2$	Permittivity of region 1 and 2 [C^2/Jm]
$\varepsilon_{r1} , \varepsilon_{r2}$	Relative permittivity of region 1 and 2 [-]
ϕ	Azimuth angle [deg]
η	Impedance of a medium [Ω]
η	Length of noise injection pulse [-]
η_A	Length of noise injection in NIR-A mode [-]
η_R	Noise injection length in NIR-R mode [-]
η_{AR}	Noise injection length in NIR-AR mode [-]
η^{off} , η^{on}	Length of noise injection, when add-on noise is on and off [-]
φ	Phase difference [deg]
λ	Wavelength [m]
μ	Normalized correlation coefficient [-]
μ_1 , μ_2	Permeability of region 1 and 2 [N/A^2]
μ_1 , μ_2	Normalized correlation coefficient measured in measurement 1 and 2 [-]
μ_p	Normalized correlarion coefficient of Dicke step *p* [-]
ω	Angular frequency [rad/s]
Ω_t	Solid angle subtended by the transmitting area [srad]
Π	Size of AIM grid
θ	Elevation angle, incidence angle [deg]
Θ	End-to-end *H-V* phase imbalance [deg]
Θ_{rec}	*H-V* phase imbalance of receivers [deg]
ρ	Charge density [C/m^3]
σ_1 , σ_2	Conductivity of region 1 and 2 [1/Ω/m]
τ	Integration time [s]
τ_A	Integration time of antenna measurement [s]
τ_N	Integration time of noise injection [s]
τ_{ref}	Integration time of reference measurement [s]
ξ,η	Direction cosines [-]
ζ_1,ζ_2	Energy levels [J]
χ_{VH}, χ_{HV}	Cross-coupling factors between channels [-]

$\mathcal{D}_{1/2}^{\mathcal{F}}$	Operator denoting matrix-vector products in regions 1 and 2 with FFT
$\mathcal{K}_{1/2}^{\mathcal{F}}$	Operator denoting matrix-vector products in regions 1 and 2 with FFT
a_C	Coefficient for the sensitivity of harmonic coefficient C, to wind speed [m/s/deg/K]
A	Gain calibration parameter of the NIR in NIR-A mode [K]
$\overline{A}_{2x,y,z}$	Vector $(N\times 1)$ of x, y, and z components of vector potential in region 2 [A/m^2]
$\overline{A}'_{2x,y,z}$	Curl of the vector $(N\times 1)$ of x, y, and z components of vector potential in region 2 [A/m^2]
$A_j^{\pm}$	Area of triangles of jth basis function [m^2]
A_R	Gain calibration parameter of the NIR in NIR-R mode [K]
A_r, A_t	Receiving and transmitting area [m^2]
$\overline{b}$	Excitation vector $(N\times 1)$ [A/m^2]
b_C	Coefficient for the sensitivity of harmonic coefficient C, to wind speed [m/s/K]
B	Offset calibration parameter of the NIR in NIR-A mode [K]
$\vec{B}$	Magnetic flux density vector [T]
B_f	Spectral brightness [J/m^2]
B_R	Offset calibration parameter of the NIR in NIR-R mode [K]
c	Speed of light, $2.998\cdot 10^8$ [m/s]
c	Non-linearity correction coefficient [-]
c_C	Coefficient for the sensitivity of harmonic coefficient C, to wind speed [m/s/deg]
C	Harmonic coefficient [K]
d	Non-linearity correction coefficient [1/K]
d_C	Coefficient for the sensitivity of harmonic coefficient C, to wind speed [m/s]
$\vec{D}$	Electric flux density vector [C/m^2]
$\underline{\underline{\mathbf{D}}}_1$, $\underline{\underline{\mathbf{D}}}_2$	Integral operator for regions 1 and 2
$\overline{\overline{D}}_1$, $\overline{\overline{D}}_2$	System matrix $(N\times N)$ components for regions 1 and 2
D_i, D_j	Directivities of the antennas of radiometers i and j [-]
$\vec{E}$	Electric field vector [V/m]
$\vec{E}_1$	Total electric field in region 1 [V/m]
$\vec{E}_1^{inc}$	Incident electric field in region 1 [V/m]
$\vec{E}_1^{scat}$	Scattered electric field in region 1 [V/m]
E_v, E_h	Vertically polarized electric field component [V/m]
f	Frequency [Hz]
f_0	Center frequency of the radiometers [Hz]
f_D	Dicke frequency [Hz]
$\vec{f}_j$	jth basis function vector[-]
$F_n(\theta,\phi)$	Normalized radiation pattern [-]
F_{ni}, F_{nj}	Normalized radiation patterns of antennas of radiometers i and j [-]
g	Gain factor of radiometer [depends on the instrument]
g	Defines the tapering of field amplitude on surface [-]

$\tilde{g}$	Modulus term of correlation [-]
$\tilde{g}_p$	Modulus term of Dicke step p [-]
g_{xy}	Gain factor from channel x to channel y [depends on the instrument]
$\overline{\overline{g}}$	Gain matrix (4×4) [depends on the instrument]
G	Gain [-]
G_1, G_2	Green's function for regions 1 and 2 [1/m]
h	Planck's constant, $6.634 \cdot 10^{-34}$ [Js]
$\vec{H}$	Magnetic field vector [A/m]
$\vec{H}_1$	Total magnetic field in region 1 [A/m]
$\vec{H}_1^{inc}$	Incident magnetic field in region 1 [A/m]
$\vec{H}_1^{scat}$	Scattered magnetic field in region 1 [A/m]
$\overline{\overline{I}}$	Unity matrix $(N \times N)$
I_i^{eff}	Coefficients of effective surface current [J/m^2]
I_i^e	Coefficients of electric surface current [J/m^2]
I_i^m	Coefficients of electric surface current [J/m^2]
$\vec{J}$	Electric current density vector [A/m^2]
$\vec{J}^{eff}$	Effective surface current density [A/m^2]
k_1	Slope of non-linearity correction model [1/K]
k_2	Offset of non-linearity correction model [-]
k_B	Boltzmann's constant, $1.38 \cdot 10^{-23}$ [J/K]
$\overline{\overline{K}}_1, \overline{\overline{K}}_2$	System matrix $(N \times N)$ components for regions 1 and 2
$\mathbf{K}_1$, $\mathbf{K}_2$	Integral operator for regions 1 and 2
$\overline{\overline{K}}_1^{\Delta}$, $\overline{\overline{K}}_2^{\Delta}$	Matrix $(N \times N)$ of difference of the near interaction elements between MoM and AIM solutions in regions 1 and 2
$K_{2,ij}^{AIM}$	AIM solution for system matrix component between ith and jth testing and basis function, respectively, in region 2
$\hat{l}_i$	Unit vector in direction of ith testing function [m]
L	Loss [-]
L_1	Loss of antenna patch [-]
L_2	Loss of intermediate section of antenna [-]
L_{ant}	Loss of antenna [-]
L_A	Loss of antenna branch connecting cable [-]
L_C	Front-end loss determined using radiometric measurement [-]
L_{DA}	Loss of antenna branch in Dicke switch [-]
L_{DC}	Loss of CAS branch in Dicke switch [-]
L_{DR}	Loss of reference branch in Dicke switch [-]
L_{NC}	Loss of controller (coupler) [-]
L_R	Loss of reference branch connecting cable [-]
L_S	Front-end loss determined using S-parameters [-]
L_S^A	Loss of antenna branch cable determined using S-parameters [-]
L_S^{NC}	Loss of controller determined using S-parameters [-]
M	Quadrature-corrected normalized correlation [-]
M	Expansion order of AIM coefficients [-]

M'	Quadrature-corrected correlation coefficient withot offset [-]
$\vec{M}$	Magnetic current density vector [V/m^2]
M_{+45}, M_{-45}	Quadrature-corrected correlation coefficients measured with +45° and -45° rotation with respect to reference transmitter [-]
M_{off}	Offset of quadrature-corrected correlation coefficient [-]
M_p	Quadrature-corrected normalized correlation coefficient of Dicke step p [-]
$\bar{n}$	Noise vector (4×1) [depends on the instrument]
N	Number of samples being correlated [-]
N	Number of interior edges of the mesh [-]
N_p	Amount of samples to be correlated in Dicke step p [-]
o	Offset factor of a radiometer [depends on the instrument]
$\bar{o}$	Offset vector (4×1) [depends on the instrument
o_3, o_4	Offset of the channel measuring 3rd and 4th Stokes parameter [depends on the instrument]
o_v, o_h	Offset of V-and H-channel [depends on the instrument]
$p_j^{\pm}$	Opposite vertices of jth basis function [m]
P	Received power [W]
P_A	Noise power from antenna [W]
P_R	Noise power from receiver [W]
$\overline{\overline{Q}}_d$	Matrix $(N\times \Pi)$ of AIM coefficients of differential components of the basis functions [-]
$\overline{\overline{Q}}_{x,y,z}$	Matrix $(N\times \Pi)$ of AIM coefficients of x, y and z components of the basis functions [-]
r	Reflectivity [-]
r	Response of the radiometer [depends on the instrument]
$\tilde{r}$	Fringe-washing factor [-]
$\vec{r}$	Vector of a three-dimensional space [m]
$\bar{r}$	Response vector (4×1) [depends on the instrument]
r_3, r_4	Responses of the channels measuring 3rd and 4th Stokes parameter [depends on the instrument]
r_{hot}, r_{cold}	Response of radiometer during measurement of hot and cold load [depends on the instrument]
r_v, r_h	Responses of V- and H-channels [depends on the instrument]
R	Distance [m]
$\vec{S}$	Energy flux [J/s/m^2]
S_{22}	S-parameter measured from port 2 to port 2 [-]
S_{21}	S-parameter measured from port 2 to port 1 [-]
S_{21}^{NC}	S-parameter of controller measured from port 2 to port 1 [-]
S_{22}^{NC}	S-parameter of controller measured from port 2 to port 2 [-]
S_{21}^{A}	S-parameter of antenna branch cable measured from port 2 to port 1 [-]
S_{22}^{A}	S-parameter of antenna branch cable measured from port 2 to port 2 [-]
T	Input noise temperature [K]
T'	Output noise temperature [K]

T_{+45}, T_{-45}	+45° and -45° polarized brightness temperature [K]
T_3, T_4	Brightness temperature of 3rd and 4th Stokes parameter [K]
T_{31}, T_{32}	First and second term of Fourier expansion for 3rd Stokes parameter [K]
T_{41}, T_{42}	First and second term of Fourier expansion for 3rd Stokes parameter [K]
T_A	Antenna brightness temperature [K]
$\hat{T}_A$	Non-linearity corrected antenna brightness temperature [K]
$T_{A\|ON}^{LCIP}$, $T_{A\|OFF}^{LCIP}$	Noise temperature of antenna branch, when noise injection is ON and OFF, at Dicke switch output [K]
$T_{A,v}$,$T_{A,h}$	Antenna brightness temperatures of V- and H-polarization [K]
$T_{A,v}^{c}$,$T_{A,h}^{c}$	Brightness temperatures of the correlated noise of V- and H-polarization [K]
T_{A0}	Known antenna brightness temperature [K]
T_{ANA}	Noise temperature of antenna branch when noise injection is on [K]
T_B	Brightness temperature [K]
$\bar{T}_B$	Brightness temperature vector (1×4) [K]
T_{cab}	Physical temperature of cable [K]
T_{CAS}	Noise temperature of noise distribution network (CAS) [K]
T_{cl}, T_{cr}	Left- and right-hand circularly polarized brightness temperature [K]
T_{DN}	Downwelling atmospheric brightness temperature [K]
T_e	Equivalent noise temperature [K]
T_{hot}, T_{cold}	Noise temperature of hot and cold load during calibration procedure [K]
T_{h0}, T_{h1}, T_{h2}	Zeroth, first and second term of Fourier expansion for H-polarization [K]
T'_{ij}	Equivalent noise temperature relative to the visibility measured with radiometers i and j [K]
$T_j^{\pm}$	Triangles of jth basis function [-]
T_I	Sum of vertically and horizontally polarized brightness temperature, 1st Stokes parameter [K]
T_{lin}	Non-linearity correction [K]
T_M	Measured brightness temperature after compensating for aircraft roll [K]
T_N	Noise temperature of the noise injection [K]
T_{NA}	Noise temperature of antenna injection [K]
$T_{NA,v}$, $T_{NA,h}$	Noise temperature of injection in antenna branch of V- and H-channel [K]
T_{NDN}	Noise temperature of noise distribution network [K]
T_{NR}	Noise temperature of reference injection [K]
T_{p1}	Physical temperature of noise source [K]
T_{p3}	Physical temperature of reference load [K]
T_{p6}	Physical temperature of intermediate section of antenna [K]
T_{p7}	Physical temperature of antenna patch [K]
T_{phys}	Physical temperature [K]
T_{pU}	Physical temperature of U-load [K]
T_Q	Difference of vertically and horizontally polarized brightness temperature, 2nd Stokes parameter [K]
T_{rec}	Receiver noise temperature [K]
$T_{rec,v}$,$T_{rec,h}$	Receiver noise temperatures of V- and H-channel [K]

T_{rec1}, T_{rec2}	Receiver noise temperature in measurement 1 and 2 [K]
T_{ref}	Noise temperature of a reference load [K]
$T_{ref\|ON}^{LCIP}$, $T_{ref\|OFF}^{LCIP}$	Noise temperature of reference branch, when noise injection is ON and OFF, at Dicke switch output [K]
T_S	Surface brightness temperature [K]
T_{t1}	Thermal noise coming from antenna [K]
T_{t2}	Thermal noise coming from antenna connection [K]
T_{t3}	Thermal noise coming from reference connection [K]
T_U	Noise temperature of U-load [K]
T_U^{LCIP}	Noise temperature of U-load at Dicke switch output [K]
T_{UP}	Upwelling atmospheric brightness temperature [K]
T_v, T_h	Brightness temperature of vertical and horizontal polarization [K]
T_{v0}, T_{v1}, T_{v2}	Zeroth, first and second term of Fourier expansion for V-polarization [K]
u, v	Antenna spacing between antennas of radiometers i and j [λ]
$\overline{\overline{U}}_{x,y,z}$	Matrix $(\Pi \times N)$ of AIM coefficients of x, y and z components of testing function [-]
$\widetilde{V}$	Amplitude-corrected complex correlation [-]
V	Output voltage [V]
$\overline{\overline{V}}_1$, $\overline{\overline{V}}_2$	System matrix $(N \times N)$ components for regions 1 and 2
V_{ij}	Visibility measured with radiometers i and j [K]
V_U	Visibility of residual offset [K]
V_C	Visibility of Corbella correlation [K]
$\overline{\overline{W}}_1$, $\overline{\overline{W}}_2$	System matrix $(N \times N)$ components for regions 1 and 2
$x(t)$, $y(t)$	Input signals being digitized and correlated [V]
$\overline{X}$	Vector $(N \times 1)$
Z	Digital correlation coefficient [-]
Z_p	Digital correlation coefficient of Dicke step p [-]

LIST OF APPENDED PAPERS

The thesis is based on the work published in the following six refereed scientific journal papers:

[P1] I. Corbella, F. Torres, A. Camps, A. Colliander, M. Martín-Neira, S. Ribó, K. Rautiainen, N. Duffo, M. Vall-llossera, “MIRAS End-to-End Calibration. Application to SMOS L1 Processor”, IEEE Transactions on Geoscience and Remote Sensing, vol. 43, no. 5, pp. 1135-1143, May 2005.

[P2] A. Colliander, S. Tauriainen, T. Auer, J. Kainulainen, J. Uusitalo, M. Toikka, M. T. Hallikainen, "MIRAS Reference Radiometer: A Fully Polarimetric Noise Injection Radiometer", IEEE Transactions on Geoscience and Remote Sensing, vol. 43, no. 5, pp. 1135-1143, May 2005.

[P3] A. Colliander, L. Ruokokoski, J. Suomela, K. Veijola, J. Kettunen, V. Kangas, M. Levander, H. Greus, M.T. Hallikainen, J. Lahtinen, ”Development and Calibration of SMOS Reference Radiometer”, IEEE Transactions on Geoscience and Remote Sensing, vol. 47, no. 7, pp. 1967-1977, July 2007.

[P4] A. Colliander, J. Kettunen, M.T. Hallikainen, “Calibration of End-to-end Phase Imbalance of Polarimetric Radiometer”, IEEE Transactions on Geoscience and Remote Sensing, vol. 44, no. 10, pp. 2635-2641, Oct. 2006.

[P5] A. Colliander, J. Lahtinen, S. Tauriainen, J. Pihlflyckt, J. Lemmetyinen, M.T. Hallikainen, ”Sensitivity of Airborne 36.5 GHz Polarimetric Radiometer’s Wind Speed Measurement to Incidence Angle”, IEEE Transactions on Geoscience and Remote Sensing, vol. 47, no. 7, pp. 2122-2129, July 2007.

[P6] A. Colliander, P. Ylä-Oijala, “Electromagnetic scattering from Rough Surface using Single Magnetic Field Integral Equation and Adaptive Integral Method”, IEEE Transactions on Antennas and Propagation, in press.

In Publication [P1] A. Colliander provided the technical information of the operation of the reference radiometer of MIRAS.

For Publication [P2] A. Colliander was responsible for the designing, carrying out and analyzing the tests. S. Tauriainen laid out the operational plan with assistance from A. Colliander, J. Uusitalo and M. Toikka, and M. Toikka designed the electronics with help from T. Auer, who was responsible for the software. A. Colliander implemented the post-processing software with help from J. Kainulainen. A. Colliander wrote the manuscript, and Prof. M. Hallikainen served as a scientific supervisor in the project and in the preparation of the manuscript.

In publication [P3], A. Colliander laid out the calibration plan. He had help from J. Suomela, K. Veijola and J. Kettunen for designing, carrying out and analyzing the tests. L. Ruokokoski designed the NIR subsystem (Flight Model) with help from V.

Kangas and M. Levander. H. Greus was responsible for Product Assurance and production of the NIR subsystem. Dr. J. Lahtinen managed the project. The manuscript was written by A. Colliander with assistance from Dr. J. Lahtinen who was responsible for Section II.A and who provided editorial assistance. Prof. M. Hallikainen served as a scientific supervisor in NIR testing and in the preparation of the manuscript.

The end-to-end calibration method presented in Publication [P4] was developed by A. Colliander, and he wrote the manuscript. J. Kettunen was responsible for the design and manufacturing of the polarizer grid used in the experiments. Prof. M. Hallikainen served as a scientific supervisor in the preparation of the manuscript.

For Publication [P5], A. Colliander analyzed the measurement results and collected the data in experiment flights no 3, 4, and 5 with assistance from J. Pihlflyckt and J. Lemmetyinen. Dr. J. Lahtinen was responsible for the processing of the measurement data, and he collected the data in experiment flights no 1 and 2. The flight experiments no 1 and 2 were planned and conducted in close cooperation with J. Lahtinen and S. Tauriainen, the flight experiments no 3, 4, and 5 in close cooperation with A. Colliander and S. Tauriainen. The manuscript was outlined by A. Colliander with some assistance from Dr. J. Lahtinen, and prepared by A. Colliander with editorial assistence from Dr. J. Lahtinen.

Publication [P6] was written by A. Colliander; he implemented the method, and he had help from Dr. P. Ylä-Oijala for developing the method, debugging the implementation and writing the manuscript. Analysis of the effect of the boundary truncation of a surface and the verification of the formulation was carried out by Dr. P. Ylä-Oijala.

1 INTRODUCTION

Remote sensing of environment, earth and atmosphere, is a field of science, which aims to improve the coverage of *in situ* measurements of certain parameters. The benefits of remote sensing are good temporal and spatial coverage of large areas and cost-effectiveness of the measurements. The field is typically divided in optical and microwave remote sensing depending on the wavelength used in the instrumentation (e.g. [1]). Also, powerful combinations of these two have been developed (e.g. [2]). The benefit of the optical remote sensing is high resolution. On the other hand, the benefit of the microwave region is the fact that clouds, fog and light rain do not disturb the measurements. In addition to this, the penetration depth of the microwave region makes it possible to measure sub-surface parameters of the target (e.g. [3]).

In the microwave region the instruments are divided into two main types: active and passive. Active instruments, like radars and scatterometers, transmit and then receive the signal carrying the information on the target that reflected the signal, whereas passive instruments, like radiometers, measure the thermal noise emitted by the target itself (e.g. [3]).

Passive microwave remote sensing is focused on the measurement of the properties of land, water, snow, ice and atmosphere: for example, in the case of land, the soil moisture (e.g. [4]-[6]) or forest stem volume (e.g. [7]) can be retrieved; in the case of water, the sea surface salinity (e.g. [8]) or the wind speed and direction can be measured (e.g. [9],[10]); in the case of snow, the snow water equivalent can be measured (e.g. [11],[12]); and in the case of ice, the ice concentration can be determined (e.g. [13]). Passive measurements have also been successfully combined with active as is done, for example, in [14] and [15].

The radiometers, as they measure low-power noise-like thermal emission, are very sensitive receivers. In comparison to radars, radiometers are simple in structure, they are cost-effective and they use less electrical power for operation (e.g. [3]). The development of radiometers for remote sensing is considered to have been initiated by Dicke *et al.* with their measurements of the atmosphere [16],[17] in the 1940's. Straiton *et al.* reported the first measurement on terrestrial materials [18]. Depending on the application, radiometers can also be airborne or spaceborne. The first airborne systems are reported in [19]-[21], and one of the first spaceborne radiometers is discussed in [22].

Polarimetric radiometers can measure, not only the power of the electromagnetic emission, as conventional radiometers, but also the phase state of the emission [23]. This information can be utilized in several applications. The first polarimetric radiometers were developed for radio astronomy in the 1950's [24],[25] and the first instruments for microwave remote sensing were in use in the beginning of the 1990's [26]-[28]. The first spaceborne polarimetric radiometer is the WindSat, which was launched in January 2003 and remains operational to date [29].

Interferometric, or synthetic aperture, radiometers use several receivers to electrically form an image of a target [30],[31]. The benefit is the fact that the spatial resolution can be enhanced without introducing one respective large antenna aperture, but spreading small antennas over an array [30]. As polarimetric radiometers, also interferometric radiometers were first utilized in radio astronomy [32],[33]. The first airborne one-dimensional interferometric radiometer, ESTAR (Electronically Steered Thinned Array Radiometer), was completed in 1988 [34],[35]. The first airborne two-dimensional interferometric radiometer, HUT-2D (Helsinki University of Technology Two Dimensional Interferometric Radiometer), was completed in 2006 [36], as was AMIRAS (Airborne Microwave Imaging Radiometer using Aperture Synthesis), also an airborne two-dimensional interferometric radiometer [37]. The first spaceborne two-dimensional interferometric radiometer, MIRAS (Microwave Imaging Radiometer using Aperture Synthesis) [38] on board ESA's (European Space Agency) SMOS (Soil Moisture and Ocean Salinity) mission [39], is scheduled for launch in 2008. In the abovementioned concepts the goal has been to achieve imaging with good spatial resolution without a large mechanically scanning antenna in a low-frequency (1.4 GHz) system on the Low Earth Orbit (LEO). Currently, there are prototypes under development, which aim at good spatial resolution from Geosynchronous Earth Orbit (GEO) without a large mechanically scanning antenna at 50 GHz and above [40],[41]. Also other applications have been proposed, but no prototypes have been reported [42],[43].

The measurement of soil moisture and ocean salinity with the relatively low frequency of 1.4 GHz, or L-band, has become the center of the focus of passive microwave remote sensing community since late 1990's. For global measurement of these parameters ESA decided to launch the SMOS satellite [44],[45]. Calibration of an interferometric radiometer is a complex issue [46]-[49]. In principle, calibration can be divided in relative and absolute calibration, and for the absolute calibration an external reference is required [50]. In AMIRAS and MIRAS the approach adopted is such that some of the elements of the receiver constellation are especially accurate receivers, so that the measurement interval of the external reference can be limited [P1]. For this purpose a reference radiometer, a fully polarimetric noise injection radiometer, was developed for both AMIRAS [P2] and MIRAS [P3]. In HUT-2D, the calibration relies on the well stabilized noise distribution network and over-flights of reference areas [36].

The calibration of polarimetric radiometers is an essential part of the design of the system, and the architecture of the instrument may introduce restrictions to the available calibration methods. The electromagnetic radiation measured by a polarimetric radiometer is usually described with the so-called modified Stokes parameters, which can be measured directly by the instrument [51]. A straightforward way to calibrate a polarimetric radiometer is to measure reference targets with a required amount of Stokes parameter combinations [27],[52]. However, the construction of such a target is not a trivial task, especially for low frequencies. As polarimetric radiometers using digital correlation were developed [53],[54], it became possible to calibrate the correlator separately. The equipment to achieve this was developed, but without addressing the calibration of the antenna [55], until a method to include also the antenna into the calibration was introduced [P4].

As stated earlier, polarimetric information measured with polarimetric radiometers can be used in several applications. Presently, the most important application is the measurement of the maritime wind vector (e.g. [56]-[59]), but also other possibilities have been examined, including periodic soil [60] and uniform crop fields [61],[62]. The wind vector measurement is based on the fact that the surface ripples of the sea, which modulate the microwave emission, are susceptible to the wind speed and direction [63],[64]. The measurement techniques and data analysis have been developed for this application since 1970's [9] and the launch of the polarimetric WindSat satellite in year 2003 has opened the possibilities for global applications [29]. In addition to the wind speed and direction, polarimetric emission of ocean surface is a function of physical temperature, frequency and incidence angle of the measurement [63]. The incidence angle dependency has been studied in [56],[58],[65],[66] and a model for the dependency is presented in [P5] based on airborne measurements over the Gulf of Finland.

Theoretical modeling of the oceanic microwave scattering and emission has also been under study for decades (e.g. [67],[68]). The studies include use of several methods to model the electromagnetic interaction and ocean surface geometry. The theoretical models help to achieve more accurate and efficient algorithms for wind vector retrieval (e.g. [69]). Scattering and emission can be solved from statistical models (e.g. [70]), or from exact computation using certain geometry yielding the full vector-wave scattering (e.g. [71]).

The integral equation formulations present a possibility for the calculation of rough surface scattering [72]. It has been demonstrated that the single magnetic field integral equation (SMFIE) provides very efficient convergence speed [73],[74]. The surface can be discretized using Rao-Wilton-Glisson (RWG) triangular basis functions with good accuracy [75]. The problem with triangular discretization is the fact that the basis functions are not uniformly distributed and the fast Fourier transform (FFT) cannot be directly applied to the matrix-vector multiplication. The adaptive integral method (AIM) solves this by approximating the basis functions on a uniform grid [76]. Therefore, the combination of SMFIE formulation, RWG basis functions and AIM can be used for efficient simulation of rough surface scattering and, for example, oceanic emission [P6].

The first objective of this study is to develop the polarimetric reference radiometer of SMOS and its calibration techniques [P1]-[P4]. The second objective is to improve the oceanic wind vector retrieval by analyzing airborne wind vector measurements as a function of incidence angle [P5], and by developing an efficient method for simulation of polarimetric emission from ocean surface [P6].

2 THEORETICAL BACKGROUND

The purpose of this chapter is to present the basic concepts and underlying theory of passive microwave radiometry and microwave radiometers. The first part of this chapter introduces the basic concepts of microwave radiometry, a field of science and engineering concerning measurements of electromagnetic radiation. The electromagnetic emission of objects and the properties of the fields of electromagnetic radiation are discussed. The microwave radiation is received with a piece of equipment called radiometer. The second part of this chapter presents the basic principles of radiometers, and finally, the third part describes the application possibilities of polarimetric microwave radiometry.

2.1 Microwave radiometry

2.1.1 Passive microwave remote sensing

Every object in our universe radiates electromagnetic radiation. The energy comes from the heat of the object, absorbed radiation of other objects or scattered radiation of other objects. Passive microwave remote sensing is about receiving that radiation of objects and thus making conclusions about the properties of the objects [3]. In Figure 2-1 typical circumstances of passive remote sensing situation are presented. The radiation to the sensor antenna, when directed towards earth, comes from multiple sources and normally only one or few of them are desired and the others are a distraction. The goal is to receive the wanted radiation with a good enough signal-to-noise ratio in such a manner that the distractive signals can be eliminated [3].

According to quantum theory, this radiation corresponds to the transition from one energy level to another. When transition is between levels with energies ζ_1 and ζ_2, the frequency, f, of the emitted photon is given by Planck's equation [77]:

$$f = \frac{\zeta_1 - \zeta_2}{h}, \tag{2-1}$$

where h is Planck's constant and is equal to $6.634 \cdot 10^{-34}$ Js. In liquids and solid materials there is so much interaction between the molecules that the frequency spectrum of the photons becomes effectively continuous, whereas in gas, the photons are emitted only at certain frequencies.

A blackbody is defined as an idealized, perfectly opaque material that absorbs all the incident radiation at all frequencies. Basically this means that while being a perfect absorber it is also a perfect emitter, because energy absorbed by an object would increase its temperature if none of the energy were emitted [3].

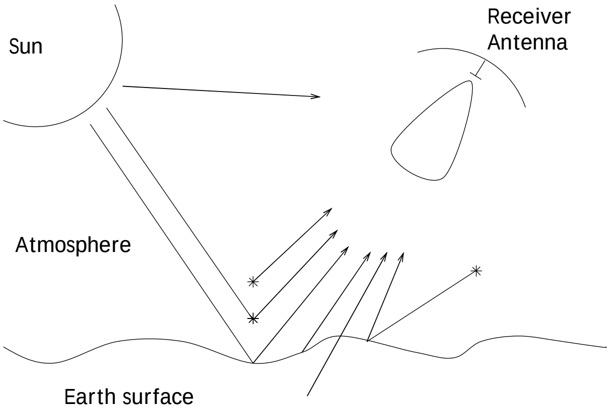

Figure 2-1. A typical passive remote sensing situation [3]. The measured radiation comes from multiple sources and the detection of the desired radiation is the main challenge.

Radiation of a blackbody is described by the Planck's radiation law, which declares that a blackbody radiates uniformly in all directions with a spectral brightness B_f given by [77]:

$$B_f = \frac{2hf^3}{c^2}\left(\frac{1}{e^{\frac{hf}{k_B T_{phys}}} - 1}\right). \tag{2-2}$$

where c is the speed of light ($2.998 \cdot 10^8$ m/s in free space); T_{phys} is the physical temperature of the object, and k_B is the Boltzmann's constant ($1.38 \cdot 10^{-23}$ J/K). The Planck's law can be approximated by the Wien radiation law when high frequencies are used, and by the Rayleigh-Jeans law when low frequencies are used. In microwave radiometry the Rayleigh-Jeans law is relevant, and is written as [3]:

$$B_f = \frac{2f^2 k_B T_{phys}}{c^2} = \frac{2k_B T_{phys}}{\lambda^2}, \tag{2-3}$$

where λ is the wavelength. In Figure 2-2 the Planck's law and Rayleigh-Jeans law are compared. The deviation of the Rayleigh-Jeans law from the Planck's law is less than 1 % if the physical temperature of the blackbody is 300 K and $f < 117$ GHz [3].

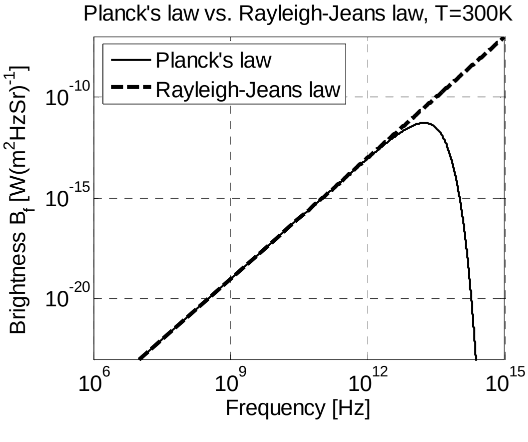

Figure 2-2. The Rayleigh-Jeans law plotted against Planck's blackbody radiation law as function of frequency, when the physical temperature of the object is 300 K.

2.1.2 Brightness temperature and Stokes parameters

Photons emitted by objects with certain spectral brightness, as described above, form an electromagnetic field, which moves away from the source. The time-harmonic electromagnetic fields can be described with the Maxwell's equations [78] (the contemporary form below can be found, for example, in [51]):

$$\begin{aligned} &\nabla \times \vec{E}(\vec{r}) = i\omega\vec{B}(\vec{r}) - \vec{M}(\vec{r}) \\ &\nabla \times \vec{H}(\vec{r}) = -i\omega\vec{D}(\vec{r}) + \vec{J}(\vec{r}) \\ &\nabla \cdot \vec{B}(\vec{r}) = 0 \\ &\nabla \cdot \vec{D}(\vec{r}) = \rho(\vec{r}) \end{aligned}, \tag{2-4}$$

where $\vec{E}$ is the electric field; $\vec{H}$ is the magnetic field; $\vec{D}$ is the electric flux; $\vec{B}$ is the magnetic flux; $\vec{J}$ is the electric current density; $\vec{M}$ is the magnetic current density; ρ is the charge density; $\vec{r}$ is a vector of a three-dimensional space, and ω is the angular frequency $\omega = 2\pi f$. This is the foundation for analysis of all electromagnetic interaction.

Electromagnetic radiation

A source with electric and magnetic current distribution, respectively, radiates electromagnetic field, which is, according to Maxwell's equations, defined as [51]:

$$\begin{aligned} \vec{E}_1(\vec{r}) &= -\frac{1}{i\omega\varepsilon_1}\mathbf{D}_1(\vec{J})(\vec{r}) - \mathbf{K}_1(\vec{M})(\vec{r}) \\ \vec{H}_1(\vec{r}) &= -\frac{1}{i\omega\mu_1}\mathbf{D}_1(\vec{M})(\vec{r}) + \mathbf{K}_1(\vec{J})(\vec{r}) \end{aligned}, \tag{2-5}$$

where ε_1 is the permittivity of the medium with $\varepsilon_1 = \varepsilon_1' + i\sigma_1/\omega$, σ_1 being the conductivity of the medium; μ_1 is the permeability of the medium; integral operators $\mathbf{D}_1$ and $\mathbf{K}_1$ are defined in Appendix A; $\vec{J}$ and $\vec{M}$ are electric and magnetic surface current densities defined as $\vec{J} = \hat{n} \times \vec{H}_1$ and $\vec{M} = -\hat{n} \times \vec{E}_1$, respectively, and $\hat{n}$ is the outer unit normal of the surface.

The power density of this field is defined by the so-called Poynting's vector, which is given by [51]:

$$\vec{S}(\vec{r}) = \frac{1}{2}\Re e\{\vec{E}(\vec{r}) \times \vec{H}^*(\vec{r})\}, \tag{2-6}$$

The purpose of microwave radiometry is to measure the electromagnetic field emitted by different targets. The measured power depends directly on the power density of the field and area of the receiving antenna, as follows [3]:

$$P = |\vec{S}|A_r, \tag{2-7}$$

where P is the received power and A_r is the area of the receiving antenna.

Brightness temperature and emissivity

As explained above, the emission of natural targets can be described with spectral brightness. This is related to the power density of electromagnetic field as [3]

$$B_f = \frac{|\vec{S}| R^2}{A_t} \frac{1}{\Delta f}, \tag{2-8}$$

where R is the distance from the source, A_t is the area of the transmitting source and Δf is the frequency range, or bandwidth. Now, the relationship between the received power and spectral brightness can be written as:

$$P = B_f \Delta f A_r \frac{A_t}{R^2} = B_f \Delta f A_r \Omega_t , \tag{2-9}$$

where Ω_t is the solid angle subtended by the transmitting area. For receiving antenna, with normalized radiation pattern, $F_n(\theta,\phi)$, where θ and ϕ are the elevation and azimuth angles, respectively, the received power can be solved by integrating over frequency range and hemisphere, yielding [3]:

$$P = A_r \int_f^{f+\Delta f} \iint_{4\pi} B_f(\theta,\phi) F_n(\theta,\phi) d\Omega df , \tag{2-10}$$

As the relationship between spectral brightness and physical temperature is given by Rayleigh-Jeans law in Equation (2-3) and if a blackbody surrounds the receiving antenna completely, the power can be related to the physical temperature with simple formula [3]:

$$P = k_B T_{phys} \Delta f . \tag{2-11}$$

It is very important to note that the same power is also obtained from a resistor at temperature T_{phys} [3].

Rayleigh-Jeans law in Equation (2-3) is given for a blackbody. However, the spectral brightness of a material, which is not a blackbody, can be defined with a blackbody equivalent radiometric temperature, which is called brightness temperature:

$$B_f(\theta,\phi) = \frac{2k_B}{\lambda^2} T_B(\theta,\phi), \tag{2-12}$$

where T_B is the brightness temperature. On the other hand, the emissivity of the material describes the relation of its brightness to the brightness of a blackbody at the same temperature [3],[79]:

$$e(\theta,\phi) = \frac{B(\theta,\phi)}{B_{bb}} = \frac{T_B(\theta,\phi)}{T_{phys}} = 1 - r(\theta,\phi), \tag{2-13}$$

which is also the ratio of the brightness temperature of the material to that of a blackbody, and also complementary to the reflectivity, r. Thus, the brightness temperature can be given by:

$$T_B(\theta,\phi) = e(\theta,\phi) T_{phys} , \tag{2-14}$$

which makes the emissivity of materials a very critical quantity for the passive microwave remote sensing, since the brightness temperature is the measured quantity. The brightness temperature of an object is always smaller than or equal to the physical temperature of the object.

The reflectivity, r, is defined as the integral of the scattering coefficients of the surface over the upper hemisphere [79]:

$$r_{pq}(\theta,\phi)=\frac{1}{4\pi}\int\left[\gamma_{pp}(\theta_s,\phi_s;\theta,\phi)+\gamma_{pq}(\theta_s,\phi_s;\theta,\phi)\right]d\Omega_s\ , \tag{2-15}$$

where subscripts p and q denote the polarization of the incidence and reflected field, respectively (polarization will be addressed in the next paragraph); γ is the scattering coefficient of the surface, which is a function of the polarization, incident field direction (θ,ϕ) and scattered field direction (θ_s,ϕ_s), and $d\Omega_s=\sin\theta_s\ d\theta_s\ d\phi_s$.

Stokes parameters

In general, the electromagnetic waves emitted by natural objects consist of a superposition of many statistically independent waves of different polarizations. This kind of a wave is said to be incoherent or unpolarised [3]. However, there are structures in natural objects, which may cause the electromagnetic field to polarize. In passive microwave remote sensing the so-called Stokes parameters are used for the complete description of the electromagnetic field and its polarization

The source of the electric field measured in passive remote sensing is generally so far away from the receiver antenna that the field, described by Equation (2-5), can be approximated to be planar [51]. This makes the description of the field considerably simpler. A planar electric field propagating in the direction of z-axis can be described with two orthogonal components perpendicular to the direction of propagation, x- and y-components in Cartesian space, as:

$$\bar{E}(z,t)=E_x e^{i(\omega t-\beta z)}\hat{x}+E_y e^{i(\omega t-\beta z+\varphi)}\hat{y}\ . \tag{2-16}$$

The phase difference of these components, φ, defines the polarization of this wave. If φ is 0° the field is linearly polarized, and if φ is 90° the field is circularly polarized; otherwise, it is elliptically polarized.

In microwave remote sensing, the use of vertical and horizontal components of electromagnetic field is most common; the naming comes from the geophysical orientation of the components. The Stokes parameters in brightness temperature, with horizontal and vertical polarization, are written as [23]:

$$\bar{I}=\begin{bmatrix}T_I\\T_Q\\T_3\\T_4\end{bmatrix}=\frac{\lambda^2}{k_B\eta\Delta f}\begin{bmatrix}\left\langle|E_v|^2+|E_h|^2\right\rangle\\\left\langle|E_v|^2-|E_h|^2\right\rangle\\2\Re e\left\langle E_vE_h^*\right\rangle\\2\Im m\left\langle E_vE_h^*\right\rangle\end{bmatrix}=\begin{bmatrix}T_v+T_h\\T_v-T_h\\T_{45}-T_{-45}\\T_{cl}-T_{cr}\end{bmatrix}=\begin{bmatrix}T_v+T_h\\T_v-T_h\\2\sqrt{T_vT_h}\,\Re e\{\tilde{V}\}\\2\sqrt{T_vT_h}\,\Im m\{\tilde{V}\}\end{bmatrix}, \tag{2-17}$$

where T_v and T_h are the brightness temperatures of the vertically and horizontally polarized radiation and T_I and T_Q are their sum and difference, respectively; T_3 and T_4 are the third and fourth Stokes parameter, respectively; E_v and E_h are the electric field components of the vertically and horizontally polarized fields, respectively; η is the impedance of the medium; T_{45} and T_{-45} are +45° and -45° polarized radiation, respectively; T_{cl} and T_{cr} are circularly left and right hand polarized radiation, respectively, and $\widetilde{V}$ is the complex correlation between the orthogonal electric fields. The brackets stand for infinite time average. Note that the phase of the complex correlation $\widetilde{V}$ is the phase difference of the vertical and horizontal components of the field:

$$\arg\left(\widetilde{V}\right) = \varphi . \tag{2-18}$$

In passive microwave radiometry the modified Stokes parameters in brightness temperature are used more commonly. They are defined as [23]:

$$\overline{T} = \begin{bmatrix} T_v \\ T_h \\ T_3 \\ T_4 \end{bmatrix} = \frac{\lambda^2}{k_B \eta \Delta f} \begin{bmatrix} \left\langle \left|E_v\right|^2 \right\rangle \\ \left\langle \left|E_h\right|^2 \right\rangle \\ 2\Re e\left\langle E_v E_h^* \right\rangle \\ 2\Im m\left\langle E_v E_h^* \right\rangle \end{bmatrix} = \begin{bmatrix} T_v \\ T_h \\ T_{45} - T_{-45} \\ T_{cl} - T_{cr} \end{bmatrix} = \begin{bmatrix} T_v \\ T_h \\ 2\sqrt{T_v T_h}\,\Re e\left\{\widetilde{V}\right\} \\ 2\sqrt{T_v T_h}\,\Im m\left\{\widetilde{V}\right\} \end{bmatrix}, \tag{2-19}$$

where the first and second Stokes parameter are the vertical and horizontal components of the field, which can be measured directly with a radiometer.

2.2 Microwave radiometers

2.2.1 Basic concept, resolution and accuracy of radiometers

A radiometer is a very sensitive microwave instrument to measure the power of the electromagnetic radiation of an object. This radiation is a noise-like signal with very low power, and thus the basic problem in radiometers is to distinguish the noise of the receiver from the received noise signal. The key elements of a radiometer are an antenna for capturing the electromagnetic radiation and a receiver for amplifying the signal up to a detectable level [3].

Conventional radiometers

Conventional radiometer means here a radiometer, which measures a single polarization of electromagnetic radiation. Figure 2-3 shows a block diagram of a standard total power superheterodyne receiver for a radiometer. It consists of an antenna; an isolator; a low-noise amplifier; a mixer mixing the incoming signal to intermediate frequency (IF); IF-filter, the bandwidth of which determines the bandwidth of the receiver; IF-amplifier; a square law detector, the output voltage of which is proportional to its input power, and an integrator.

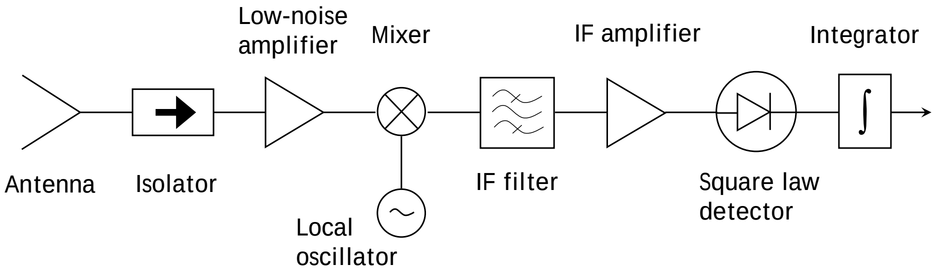

Figure 2-3. The principle of a total power radiometer with a superheterodyne receiver, meaning that the input signal is mixed down to a lower frequency, or intermediate frequency, using a mixer [3].

If the antenna is pointed to a scene with a brightness temperature T_A, the antenna power will be $P_A=k_BT_A\Delta f$, yielding from Equations (2-11) and (2-14). The noise power of the receiver is $P_R=k_BT_{rec}\Delta f$, where T_{rec} is the noise temperature of the receiver. Thus, the output voltage of the radiometer can be written as [3]:

$$V_0 = G\left(T_A + T_{rec}\right)k_B\Delta f\ , \tag{2-20}$$

where G is the gain of the receiver.

The receiver noise temperature of a radiometer can be determined by measuring two reference loads of different noise temperatures. This is often called as the Y-factor method [3]. However, this method assumes that the detector of the radiometer has no offset, which is not always the case. In order to solve the offset, an additional attenuator can be placed in front of the detector, so that the measurement can be performed either with the attenuator on or off (nominal measurement is performed with the attenuator off). Now, making the Y-factor measurements with attenuator on and off yield four results, from which the offset and receiver noise temperature can be solved. The method is often referred to as four-point method (introduced in [98] and explained e.g. in [99]; see also Appendix B).

There are two major sources of error in a radiometer. Due to the random nature of noise the power of the noise varies from one integration period to the next. It is shown in [80] that this ΔT_A has a value of

$$\Delta T_A = \frac{T_A + T_{rec}}{\sqrt{\Delta f\,\tau}}\ , \tag{2-21}$$

where τ is the integration time. Obviously, when τ is increased the error decreases. This value is also called the radiometric resolution of a radiometer.

The second error comes from the random gain fluctuations of the receiver, due to the instability of the amplifiers, filter and mixer. These variations take place over a period of about one second or longer. So, if the radiometer is calibrated with a certain value of G, which will change by the time a measurement is made, the error will be [80]

$$\Delta T_G = \left(T_A + T_{rec}\right)\frac{\Delta G}{G}\ , \tag{2-22}$$

where ΔG is the rms change in the system gain G.

The effect of the second error can be minimized by introducing a reference load to the front-end of the radiometer. As the radiometer is switched for the half of the measurement time to this known reference load the effect of the gain and receiver noise temperature variations can be cancelled out. This kind of a radiometer is called a Dicke radiometer. The switching frequency has to be fast enough to compensate the varying gain of the radiometer.

When the radiometer sees the reference load, T_A of Equation (2-20) becomes T_{ref}. Thus, when the measurements of the antenna and reference are subtracted, the output voltage becomes [3]

$$V_o = G(T_A + T_{rec})k_B\Delta f - G(T_{ref} + T_{rec})k_B\Delta f = G(T_A - T_{ref})k_B\Delta f\,, \qquad (2\text{-}23)$$

and the receiver noise temperature T_{rec} is eliminated. However, as shown in [3], the true benefit of Equation (2-23) is achieved only when $T_A = T_{ref}$, since only then the gain fluctuations are completely cancelled out. A method for acquiring this has to be utilized.

It is said that a Dicke radiometer is balanced when the reference load noise temperature is equal to that of the antenna. This balancing can be made with four methods [3]: (1) reference-channel control method, (2) antenna-channel noise-injection method, (3) pulsed noise-injection method, and (4) gain-modulation method. The second method is relevant for this work. In the antenna-channel noise-injection method, noise is injected to the antenna signal so that the level of the antenna signal equals the reference signal.

The radiometric resolution for a noise injection radiometer is determined so that the injected noise and reference load measurements are taken into account:

$$\begin{aligned}\Delta T_A &= \sqrt{\left(\eta\frac{T_A + T_{rec}}{\sqrt{\Delta f\tau_A}}\right)^2 + \left((1-\eta)\frac{T_A + T_N + T_{rec}}{\sqrt{\Delta f\tau_N}}\right)^2 + \left(\frac{T_{ref} + T_{rec}}{\sqrt{\Delta f\tau_{ref}}}\right)^2}\\ &\approx \frac{2(T_{ref} + T_{rec})}{\sqrt{\Delta f\tau}}\end{aligned}\,, \qquad (2\text{-}24)$$

where η is the length of the noise injection; $\tau_A + \tau_N + \tau_{ref} = \tau$, and T_N is the level of the noise injection.

Polarimetric radiometers

A radiometer measuring all Stokes parameters, a polarimetric radiometer, can be implemented using several different approaches. They can be classified, based on the technique used to solve the 3rd and 4th Stokes parameters, into two categories: instruments using incoherent and instruments using coherent detection. This classification originates from the definition of Stokes parameters: in Equation (2-17) the 3rd and 4th Stokes parameters can be solved either by differentiation, which is called incoherent detection, or by using correlations, which is called coherent detection.

Incoherent detection can be implemented by a quasi-optical device in-front of the antenna of a conventional radiometer [81]; using a phase modulator between the antenna and a conventional receiver [82]; time-multiplexing the direct measurement of the principal polarizations [28]; using parallel channels [29], or using a polarization combining network [83].

Coherent detection can be implemented by direct measurement of vertical and horizontal polarizations and their complex correlation using the adding techniques [27] or direct cross-correlation [84]. Furthermore, there are several different techniques demonstrated over the years for implementing either adding or cross-correlation correlators (for example [54],[58],[85],[86]).

Figure 2-4 shows a schematic diagram of the principle of a correlating polarimetric radiometer. One channel changes the phase of the signal by 90° degrees; this is called the quadrature channel, and its deviation from 90° is called quadrature error.

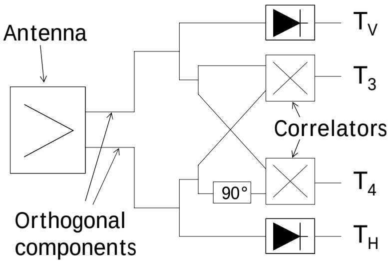

Figure 2-4. The principle of correlating polarimetric radiometers.

When the normalized complex correlation of the two receivers is measured using 1-bit/2-level digital correlators, the correlation value is given according to the following equation [53]:

$$Z = \frac{1}{N}\sum_{i=1}^{N} \operatorname{sign}(x(t_i))\operatorname{sign}(y(t_i)) \tag{2-25}$$

in which $x(t)$ and $y(t)$ are the input signals being digitized and correlated and N is the number of samples being correlated. This digital correlation value is related to the analogue correlation value, when it is applied to the signal which has a limited spectrum, as [87]

$$\mu = \sin\left(\frac{\pi}{2}Z\right) \tag{2-26}$$

where μ is called here as the normalized correlation coefficient. After the normalized correlation coefficient μ is corrected for digitizer offset and quadrature error (as explained e.g. in [P3]) the correlation coefficient is called the quadrature-corrected normalized correlation and denoted with M.

The amplitude correction of the measured correlation coefficient is done using the so-called modulus term as follows:

$$M = \tilde{g}\tilde{V} \tag{2-27}$$

where $\tilde{V}$ is the amplitude-corrected correlation and $\tilde{g}$ is the modulus term defined as

$$\tilde{g} = \tilde{r}_{vh}\sqrt{\frac{T_{A,v}}{T_{A,v} + T_{rec,v}}}\sqrt{\frac{T_{A,h}}{T_{A,h} + T_{rec,h}}} \tag{2-28}$$

where $\tilde{r}_{vh}$ is the fringe-washing factor of V- and H-channel, which accounts for the differences in the frequency responses of the receivers; $T_{A,v}$ and $T_{A,h}$ are the antenna brightness temperatures of V- and H-polarization, respectively, and $T_{rec,v}$ and $T_{rec,h}$ are the receiver noise temperatures of V- and H-channel, respectively.

In the case of noise injection radiometers, additional noise is injected to the measurement signal. This can be accounted for as an increase of respective amount in the system noise temperature i.e. in the denominator of Equation (2-28) [P2].

Interferometric radiometers

The brightness temperature image of a target can also be created using a technique called interferometry. It was first developed for radio astronomy [32],[33], but in late 1980’s it was also applied for the Earth remote sensing [34],[35],[88],[89].

The principle of the method is to form a synthetic aperture with a thinned array of radiometers, which measure the so-called visibilities by correlating pair-wise the outputs of all the radiometers in the array [30]. The brightness temperature can then be solved from the visibilities using the following relationship [48]:

$$V_{ij}(u,v) = \iint_{\xi^2+\eta^2\le 1} T'_{ij}(\xi,\eta)\tilde{r}_{ij}\left(-\frac{u\xi+v\eta}{f_0}\right)e^{-j2\pi(u\xi+v\eta)}\,d\xi\,d\eta \tag{2-29}$$

where V_{ij} is the visibility measured with radiometers i and j; u and v denote the antenna spacing between antennas of radiometers i and j; $(\xi,\eta) = (\sin\theta\cos\phi, \sin\theta\sin\phi)$ are the direction cosines; $\tilde{r}_{ij}$ is the fringe-washing factor of radiometers i and j; f_0 is the center frequency of the radiometers, and T'_{ij} is the equivalent noise temperature relative to the visibility, defined as:

$$T'_{ij}(\xi,\eta) = \frac{\sqrt{D_i D_j}}{4\pi}\frac{T_B(\xi,\eta) - T_{ph}}{\sqrt{1-\xi^2-\eta^2}}F_{ni}(\xi,\eta)F^*_{nj}(\xi,\eta) \tag{2-30}$$

in which D_i and D_j are the directivities of the antennas of the radiometers i and j; T_B is the brightness temperature received from direction (ξ,η); T_{ph} is the physical temperature of the receivers, and F_{ni} and F_{nj} are the normalized radiation patterns of the antennas of radiometers i and j. Given by the above expression, the brightness temperature can be solved from the visibilities by applying Fourier transform; in practice Fast Fourier Transformation (FFT) is applied. The resulted brightness temperature image is then coordinate-transformed and geo-located to give the final image.

The shape and density of the constellation of the thinned array used for aperture synthesis depends mostly on the desired resolution and field of view [30]. Note also, that depending on the application, the array can be formed from the antennas alone and the receiver units are located separately.

2.2.2 Calibration of radiometers

Conventional calibration

Usually the detector of a radiometer is assumed to behave in a liner manner i.e. the output of the radiometer has a straight-line relationship to the received power [3]. In this situation one has to know only two points from the line, which is called the calibration line, to know the brightness temperature of the measured target for every output in a certain range (see Figure 2-5).

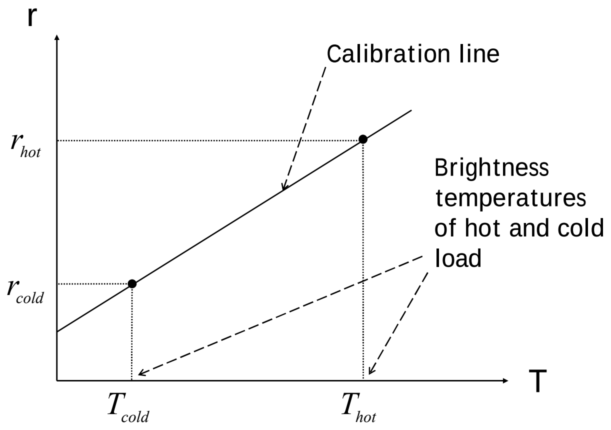

Figure 2-5. The calibration line of a radiometer in principal. The detection of the radiometer is assumed to behave in a linear manner.

There has to be at least two targets brightness temperatures of which are known for defining the calibration line. These calibration targets are often called the hot and cold load. The response of a linear radiometer can be defined as [3]

$$r = gT_B + o, \tag{2-31}$$

where g is the gain factor and o is the offset describing the response of the radiometer, and r is the output response of the radiometer. g and o can be calculated from calibration measurements in the following manner:

$$\begin{aligned} g &= \frac{r_{hot} - r_{cold}}{T_{hot} - T_{cold}} \\ o &= \frac{r_{cold}T_{hot} - r_{hot}T_{cold}}{T_{hot} - T_{cold}} \end{aligned} \tag{2-32}$$

where T_{hot} and T_{cold} are the hot and cold noise temperatures coming into the radiometer during calibration procedure, respectively, and r_{hot} and r_{cold} are the respective responses.

In the calibration of a noise injection radiometer, the so-called noise amplitude calibration can be utilized. The calibration requires only one known target, with which the injection noise temperature, T_N, can be accurately determined. The principle can be formulated as follows [3]:

$$T_N = \frac{T_{ref} - T_{A0}}{\eta}, \tag{2-33}$$

where T_{ref} is the known reference load noise temperature, T_{A0} is the known antenna temperature for calibration, and η is the length of the noise injection pulse. Now the antenna temperature can be solved, using T_N and η. This method, however, requires very accurate characterization of the loss of the antenna and its connection.

For the calibration of the non-linearity of a radiometer, few methods have been demonstrated in the literature. However, in [90] two robust and accurate methods were presented. One is based on adding a constant amount of noise on top of a varying amount noise, which is fed in to the radiometer. This way, the change in the detected add-on noise reveals the non-linearity of the radiometer.

Polarimetric calibration

The calibration of polarimetric radiometers requires additionally the calibration of the third and fourth Stokes parameters. This can be done in several ways depending on the design of the radiometer. The fundamental approach is to do an end-to-end calibration for each Stokes parameter. This includes also the cross-talk between all parameters, and can be formulated as follows [27],[52]:

$$\bar{r} = \begin{bmatrix} r_v \\ r_h \\ r_3 \\ r_4 \end{bmatrix} = \bar{\bar{g}}\bar{T}_B + \bar{o} + \bar{n} = \begin{bmatrix} g_{vv} & g_{vh} & g_{v3} & g_{v4} \\ g_{hv} & g_{hh} & g_{h3} & g_{h4} \\ g_{3v} & g_{3h} & g_{33} & g_{34} \\ g_{4v} & g_{4h} & g_{43} & g_{44} \end{bmatrix} \begin{bmatrix} T_v \\ T_h \\ T_3 \\ T_4 \end{bmatrix} + \begin{bmatrix} o_v \\ o_h \\ o_3 \\ o_4 \end{bmatrix} + \bar{n}, \tag{2-34}$$

where $\bar{r}$ is the output response vector; $\bar{g}$ and $\bar{o}$ consist of the radiometer gain and offset, respectively, and $\bar{n}$ is the random noise of the instrument referred to the outputs. The calibration parameters $\bar{g}$ and $\bar{o}$ can be solved by introducing linearly independent sets of precisely known Stokes parameters [52].

However, as discussed in the previous section, in the case of digital 1-bit/2-level correlations, the correlation coefficient is measured separately from the correlated amplitude. This can be utilized in the calibration, so that the 1st and 2nd Stokes parameter is calibrated by conventional means and a correlated noise source is introduced to calibrate the correlations (for example [47]), yielding the calibration of the 3rd and 4th Stokes parameters, see Equation (2-19). The calibration of the correlations requires also the knowledge of the receiver noise temperature and fringe-washing factor, see Equation (2-28).

Calibration of interferometric radiometer

The calibration of the interferometric radiometer is a significantly more complex issue than the calibration of conventional or polarimetric radiometers. The calibration can be divided into phase and amplitude calibrations, and also relative and absolute calibration. Relative calibration includes calibration of the differences between the radiometers in the array, whereas absolute calibration includes the calibration of the actual values retrieved with the instrument. The calibration can also be performed by measuring the so-called G-matrix, which means in practice an end-to-end calibration for each pixel in the image [46].

The properties of the antennas are critical for the image construction, as can be seen in Equation (2-30). The normalized antenna patterns needs to be known with certain accuracy [91],[92],[93]. This can be considered as an absolute calibration parameter of the amplitude and phase calibration.

With certain built-in techniques, offsets of the correlation coefficients and quadrature errors can be solved relatively easily and accurately [P1],[40],[94]. The phase differences, or phase delays, between the receivers need a correlated calibration source. This is a relative calibration parameter of phase calibration. Internal noise distribution network can be used to provide a common noise reference to all receivers [47],[95],[96]. The correlated noise with delayed correlations, implemented in the correlator, can also be used to solve the fringe-washing function [97].

The receivers can cause small residual offsets to the correlations. This can be measured by pointing the receiver to measure an uncorrelated load, which can be a simple matched load at the same physical temperature as the front-end [47], [P1]. This is an absolute calibration parameter of amplitude and phase calibration.

An important absolute amplitude calibration parameter is the receiver noise temperature of the receivers [47],[95]. In a nominal case, the receiver noise temperature cannot be assumed to remain constant, and the internal noise distribution network can be used to retrieve it, together with the uncorrelated reference load. In this case the noise temperatures of both of these sources need to be known [47]. The noise distribution network can also have two levels, which are used for this purpose [99]. The level, or levels, of the noise distribution networks need to be known. Either the network needs to be very stable, or the level is measured with a dedicated radiometer [P1].

Finally, the average brightness temperature level incident to the instrument needs to be known accurately, being an absolute calibration parameter of the amplitude calibration. This can also be measured with a dedicated very accurate radiometer in order to relax some of the requirements of the rest of the radiometers [P1].

2.3 Applications of polarimetric radiometry

The emission of natural materials is unpolarised, but the geometric shape of some natural targets is such that the emitted radiation may be partially polarized. This can be utilized when the properties of these targets are measured using polarimetric radiometers.

The potential applications include the measurements of maritime winds, plied fields, corn fields, atmosphere and ice. In the case of maritime winds, the surface geometry causes the emission to polarize; that is, the wind modulates the surface, which in turn can be detected with a polarimetric radiometer [26]. Similarly, the shape of the plied fields can be detected [100]. In the case of the corn fields, the uniformly aligned corn straws cause the emission to polarize [61],[62]. In the case of the atmosphere, the temperature profile of the mesosphere can be optimally measured using all Stokes parameters due to the changes in geomagnetic viewing conditions [101]. Also, in rain events, non-spherical rain drops and scattering from ice crystals cause polarization [102]-[104]. And in the case of ice, two phenomena have been predicted: the surface of the ice sheets may be shaped by streams over glaciers, especially in Greenland [105],[106], and the c-axis orientation of ice may cause polarization in the emitted signal [107].

By far, the most studied phenomenon is the maritime wind vector. The first results with H- and V-polarization were retrieved already in the beginning of 1970's [108], but the first polarimetric measurements were reported only in the beginning of 1990's [26]. The fundamental result have been the establishment of an approach using second order Fourier series to describe the Stokes parameters as a function of the azimuth angle (for example [109],[110]):

$$T_v \cong T_{v0} + T_{v1}\cos\phi + T_{v2}\cos 2\phi, \tag{2-35}$$

$$T_h \cong T_{h0} + T_{h1}\cos\phi + T_{h2}\cos 2\phi, \tag{2-36}$$

$$T_3 \cong T_{31}\sin\phi + T_{32}\sin 2\phi, \tag{2-37}$$

$$T_4 \cong T_{41}\sin\phi + T_{42}\sin 2\phi, \tag{2-38}$$

where ϕ is the wind direction. The first harmonics account for the upwind/downwind asymmetry of the surface and the second harmonics account for the upwind/crosswind asymmetry of the surface. The Fourier coefficients of the two harmonic components as well as the zero order terms, or offsets, of the first and second Stokes parameters are functions of several parameters.

The most significant uncertainty in the wind determination is in the establishment of the relationship between the wind and surface geometry (for example [68],[70], [112]). In principle, the wind causes ripples on the surface of water but, for example, the larger scale waves modulate these ripples manifesting additional uncertainty to the assumption of the behavior of polarimetric emission [111].

A very important aspect in the wind vector measurement techniques is the development of numerical simulation methods, in order to predict and understand the measurement results. These simulations involve both simulation of the wind modulated surface geometry (e.g. [68],[109],[112]) and simulation of the electromagnetic interaction (e.g. [71],[113],[114]). Techniques involve both statistical simulation based on certain characteristic parameters and, more and more often as computing power has increased, deterministic methods based on exact geometries.

3 RECENT ADVANCES AND TOPICS IN POLARIMETRIC RADIOMETRY

The purpose of this chapter is to present recent advances in polarimetric radiometry in order to illuminate the background and impact of the research described in this work. The first part describes the advances in the development of polarimetric radiometers and their calibration, the second part concentrates on the maritime wind vector retrieval, and finally, in the third part the progress in the simulation of the electromagnetic scattering from ocean surface is discussed.

3.1 Polarimetric radiometers

Over the last two decades both incoherent and coherent detection polarimetric radiometers have been constructed and used for remote sensing measurements and experiments. The main application area has been the measurement of maritime wind vector.

Currently, the developed polarimetric radiometers tend to use either coherent detection with cross-correlating correlators [54],[58],[84], or incoherent by combining topology [29],[83],[115]. The first spaceborne polarimetric radiometer, WindSat, uses incoherent detection by parallel channels for each principal polarization. This type of detection was chosen for this application due to reliability of the available components in spaceborne environment and straightforward calibration [29]. As the integration time is limited in typical remote sensing applications, the time multiplexing polarimetric radiometers have not become popular.

The digital correlators have become common up to frequencies of several gigahertz making it possible to implement digital correlators for radiometers operating at millimeter wave frequencies [40],[54]. One defining parameter in digital correlators is the number of bits used; i.e., how many bits are used for the sampling of the signal and then to be correlated. Only one bit, the sign bit, can give enough information, but this reduces the sensitivity compared to the use of two or more bits [53]. However, the degradation is not seen as a problem and one-bit correlators have been applied in many instruments including L-band interferometric synthetic aperture radiometers [36],[37],[P2],[P3].

In the measurement of the principal polarizations, the digitally controlled front-ends are common. This makes it feasible to develop more enhanced Dicke-type switching configurations; combinations of noise source and reference loads have been demonstrated [116],[P2],[P3]. This also benefits the flexibility of polarimetric calibration providing, for example, a phase reference.

Furthermore, direct digital sampling of the measured signal without mixing to the intermediate frequency has already been demonstrated at L-band [117], and it is expected that this type of instruments will also be developed for higher frequencies.

The frequency of the developed polarimetric radiometers was first concentrated on about 10 GHz, 18 GHz and 37 GHz [26] due to the wind vector applicability, but 1.4 GHz, 6 GHz and 90 GHz instruments have also been introduced for various applications, such as study of polarimetric ocean signatures at 1.4 GHz and atmospheric signatures at 90 GHz (e.g. [117],[86],[P1],[P2]) Table 3-1 lists the reported airborne and spaceborne polarimetric radiometers.

As discussed in previous Chapter, calibration techniques of polarimetric radiometers, and especially that of the third and fourth parameter, depend greatly on the design of the instrument. Incoherent radiometers can usually be calibrated using conventional means, but correlating radiometers require a method that includes also calibration of the correlator.

Table 3-1. A summary of reported airborne and spaceborne polarimetric radiometers. A/S indicates whether the instrument is airborne (A) or spaceborne (S).

Name	**Developer, Year** [1]	**Frequency [GHz]**	**Pol. chan.**	**Detection method**	**Architecture**	**A/S**	**Reference**
MIRAS NIR	Ylinen and TKK, 2006	1.4	$T_{3,4}$	Coherent, digital corr.	Noise injection	S	[P3]
WindSat	NRL, 2003	10.7; 18.7; 37.0	$T_{3,4}$	Incoherent, parallel channels	Total power	S	[29]
AMIRAS NIR	TKK, Ylinen, Toikka, 2003	1.4	$T_{3,4}$	Coherent, digital corr.	Noise injection	A	[P2]
APMIR	NRL, 2003	10.7; 18.7; 19.35; 37.0	$T_{3,4}$	Incoherent, combining	Total power	A	[83]
EMIRAD	TUD, 1999	1.4; 16.0; 34.0	$T_{3,4}$	Coherent, digital corr.	Dicke	A	[84] [117]
PSR-C	NOAA, 1999	6.92; 10.7	$T_{3,4}$	Coherent, adding analog corr.	Total power	A	[118] [86]
FPoR	TKK, 1997	36.5	$T_{3,4}$	Coherent, analog corr.	Dicke	A	[119] [58]
PSR-A	NOAA, 1996	10.7; 18.7	$T_{3,4}$	Coherent, adding analog corr.	Total power	A	[120] [86]
		37.0; 89.0	T_3				
-	NRL, 1996	10.8	$T_{3,4}$	Incoherent, no further data avail.	-	A	[121]
PSR-D	Ga. Tech., 1996	10.7; 18.7; 37.0; 89.0	T_3	Coherent, digital corr.	Total power	A	[86] [54]
WINDRAD	JPL, 1994	19.35	$T_{3,4}$	Incoherent, time multiplex.	Dicke	A	[10]
		37.0	T_3				
NAMR	SRI, 1985	20.0; 37.0	T_3	Incoherent, time multiplex.	Dicke	A	[26],[124] [125]

1) This referes to the reported year of completion or first measurement

An important step in the development of the calibration techniques was the development of the fully polarimetric calibration standard, which generates required amount of targets of linearly independent Stokes vectors for calibrating each Stokes parameter [52]. However, the construction of such a target is not a trivial task, especially for low frequencies, which would require large mechanical size. As polarimetric radiometers using digital correlation were developed [53],[54], it became possible to calibrate the correlator separately. The equipment to achieve this was developed, but without addressing the calibration of the antenna [55], until a method to include also the antenna into the calibration was introduced [P4].

3.2 Retrieval of wind vector

Several studies have reported airborne polarimetric measurements of oceans in order to establish the relationship between the wind speed and direction and the Stokes parameters. Table 3-2 lists these measurements. In general, all experiments show similar behavior for the harmonic coefficients of Stokes parameters, see Equations (2-35)-(2-38), with respect to the wind speed and direction. Some of these studies have considered the dependence of the harmonic coefficients on incidence angle. The dependence is predicted theoretically, and also observed in measurements [69], but in detail measured incidence angle variations of the harmonic coefficients of the third Stokes parameter were studied in [P5]. Note that Table 3-2 lists only those airborne and spaceborne reports that include polarimetric results; for example, airborne campaigns of APMIR (see Table 3-1, [83]) have been reported but no polarimetric results have been included [132],[133].

The global measurements of WindSat have created a huge amount of data, which have been investigated in numerous studies (e.g. [59],[66],[126]). The latest results show that the high-accuracy methodology is still to be consolidated, although good results have been retrieved when compared to buoy and other instrument measurements [59]. One of the main problems remaining is the flagging of the rain without over flagging, which means that signals, resembling those obtained during rain events, are measured also when no rain has been observed by validation.

Additional issues in the wind vector retrieval include modeling of the atmospheric attenuation and scattering (e.g. [127],[128]), and effects of braking waves and foam over the surface (e.g. [129]-[131]). Both of these phenomena have received plenty of attention, but still require further study, both theoretical and experimental.

Table 3-2. Reported airborne and spaceborne polarimetric measurements of maritime winds. Column Parameters shows those parameters that are addressed in the study; f is the frequency used; θ is the incidence angle (off nadir); Location is the region where the study was made, and Year indicates the time when the measurements were made.

Parameters	f [GHz]	θ	Location	Year	Reference
$T_{v,h,3}$	10.7	53°	Labrador Sea	1997	[56]
$T_{v,h,3,4}$	10	50°	Global	2003-	[29]^1
T_3, T_Q	20	0°	Pacific Ocean^2	1991	[26]
$T_{v,h,3}$, T_Q	19.35	30,40,50°	NDBC^3	1993	[28]
$T_{v,h,3,4}$, T_Q	19.35	45,55,65°	NDBC	1994-96	[10],[65]
T_3, T_Q	16.26	45°	Danish Coast	1996	[123]
$T_{3,4}$, T_Q	16	55°	North Sea	1998	[57]
$T_{v,h,3,4}$	18	55°	Global	2003-	[29]^1
T_3,T_Q	34	0°	Pacific Ocean^2	1991	[26]
T_3,T_Q	37	0°	Atlantic Ocean	1992	[124],[125]
$T_{v,h,3}$,T_Q	37	45,55,65°	NDBC	1994-96	[10],[65]
$T_{v,h,3}$	37	53°	Labrador Sea	1997	[56]
$T_{3,4}$,T_Q	37	50°	North Sea	1998	[57]
$T_{v,h,3,4}$	36.5	43-58°	Baltic Sea	2002-04	[58],[P5]
$T_{v,h,3,4}$	37	53°	Global	2003-	[29]^1

1) Several publications, for example [59],[66],[126]
2) North Western Pacific Ocean
3) National Data Buoy Center, Californian Coast

3.3 Simulation of rough surface scattering

The simulation of electromagnetic scattering from dielectric rough surfaces is very important for the development of applications in remote sensing of ocean, soil and ice. Especially, the modeling of ocean is tempting due to its relatively simple structure compared to, for example, vegetation covered layered ground.

The studies of ocean scattering and emission include the use of several methods to model the electromagnetic interaction and ocean surface geometry. The theoretical models have helped to achieve more accurate and efficient algorithms for wind vector retrieval (e.g. [65],[66],[69],[71],[126]). Scattering and emission can be solved from statistical models (e.g. [69],[134]) or calculated from the electromagnetic interaction of certain geometry and material properties yielding the full vector-wave scattering (e.g. [71]). However, the calculation of full vector-wave scattering from a large surface is a very demanding task. The difficulties in the problem lie on the large surface size and on the magnitude of the surface roughness. Solving a problem of this kind requires a lot of unknowns in order to get accurate and meaningful results. Thus, reduction on both computation time and data storage requirement has been continuously sought with increasing computation power.

There have been two dominating methods for solving a full vector-wave scattering from a two-dimensional (2-D) rough dielectric surface. One of these methods is based on the sparse matrix canonical grid method (SMCG) (e.g. [135]-[137]) and the other is based on the fast multipole method (e.g. [113],[138],[139]). The SMCG method has also been extended to a three-dimensional (3-D) case, which is called multilevel SMCG [114]. The solution in 3-D allows more accurate results with a high magnitude of surface roughness. Both methods distinguish the strong near field interaction and weak far field interaction between field point and source point. This has the advantage that only the near interaction matrix is stored and the far interaction matrix is not stored but its multiplication with a solution vector is calculated by fast means.

The surface integral equations [140] have been widely used to solve problems of electromagnetic scattering and their formulation is one way to make the simulation more efficient. One of the formulations that has been observed to converge very fast is the single magnetic field integral equation (SMFIE) [73],[141],[142]. More classical formulations are magnetic and electric field integral equation (MFIE and EFIE, respectively), and combined field integral equation (CFIE) [143]. Figure 3-1 shows a comparison between the convergence speed of single integral equation formulations based on MFIE, EFIE and CFIE, and formulation based on coupled integral equations (the figure is schematic plot of the results reported in [73]). SMFIE shows superior performance. A very common method is to solve the scattering problem iteratively (using, for example, generalized residual method GMRES [144]), which makes it desirable to have the problem converge fast to its solution.

As it is desired to model the surface as accurately as possible, the so-called Rao-Wilton-Glisson (RWG) triangular basis functions are very suitable for this purpose [75]. On the other hand, Fourier transform has been proved to be efficient tool for solving integral equations with respect to memory use and also processing time, and hence, Fast Fourier Transform has been used in multiple methods (e.g. [145]). In order to overcome the problem that the RWG functions do not form a uniform grid, to which FFT can be applied, two methods have been presented: adaptive integral method (AIM) [76] and precorrected-FFT method [146].

The field of scattering theory and computational techniques develops enormously fast, and new more efficient techniques are invented continuously. This happens simultaneously with increasing computation power, outdating many techniques as soon as they are developed.

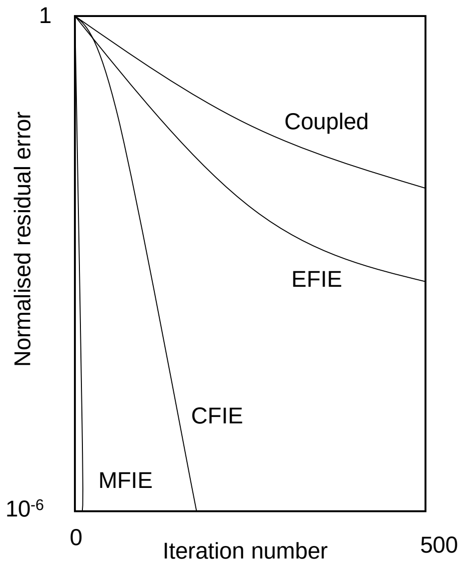

Figure 3-1. Convergence speeds of the single integral equation formulations based on the MFIE, EFIE, and CFIE, respectively, compared with the convergence speed of the coupled integral equations formulation, for a dielectric sphere with $\varepsilon_{r2} = 4.0$ *and* $k_1a = 0.5$ *(wave number times radius). The schematic diagram is based on the results presented in [73].*

4 POLARIMETRIC RADIOMETER AS A REFERENCE FOR SYNTHETIC APERTURE RADIOMETER

As discussed in previous Chapters, L-band remote sensing radiometers can be used to measure soil moisture and sea surface salinity [147],[148]. In general, brightness temperature decreases with increasing soil moisture and sea surface salinity. Both of these parameters are valuable in improving weather forecasting and climate monitoring. ESA, in co-operation with CNES of France and CDTI of Spain, has initiated the SMOS project [39] to develop a spaceborne interferometric synthetic aperture radiometer (see Section 2.2.1) for global measurement of these parameters [44],[45]. The instrument is called MIRAS (Microwave Imaging Radiometer using Aperture Synthesis) [38]. Figure 4-1 shows an artist's view of the SMOS in the orbit. The development of MIRAS was preceded by the development of an airborne demonstrator, AMIRAS [37]. Figure 4-2 shows a photograph of AMIRAS.

Both MIRAS and AMIRAS include polarimetric reference radiometers, which have three purposes:

1) to measure the noise temperature of the two output noise levels of the CAS subsystem, a noise distribution network used for the internal calibration of AMIRAS and MIRAS (see Section 2.2.2 and [149] for a description of CAS subsystem of MIRAS),
2) to measure the average polarimetric brightness temperature of the measurement scene, which is used for the calibration of the offset in the AMIRAS and MIRAS brightness temperature image (see Section 2.2.2), and
3) to form so-called mixed baselines with LICEF-units for interferometric image generation.

The reference radiometers use noise injection method (see Section 2.2.1); hence called NIR. The LICEF-units (Light-weight Cost-effective Receiver) are the regular receivers, which form the array of receivers, together with NIR-units, for interferometric image creation (see Section 2.2.1). In MIRAS, there are sixty-six LICEF-units and three NIR-units.

AMIRAS has one NIR-unit[1] in the center of the Y-shaped array, as shown in Figure 4-2, whereas MIRAS has three NIR-units[2] in the hub section of the instrument, as shown in Figure 4-3. In the block diagram level, the design of the airborne NIR is the

---

[1] The NIR-unit of AMIRAS was developed in MDPP-2 project by TKK with Ylinen Electronics (currently part of DA-Design Oy) and Toikka Oy as subcontractors.

[2] The NIR-units of MIRAS were developed in the SMOS project, phase C/D by Ylinen Electronics (currently part of DA-Design Oy) with TKK as subcontractor.

same as the design of the spaceborne NIR. However, in the detailed design the spaceborne unit is completely different due to application of space qualified components and manufacturing processes, reduced mechanical and mass envelope, and enhanced EMC and environmental requirements.

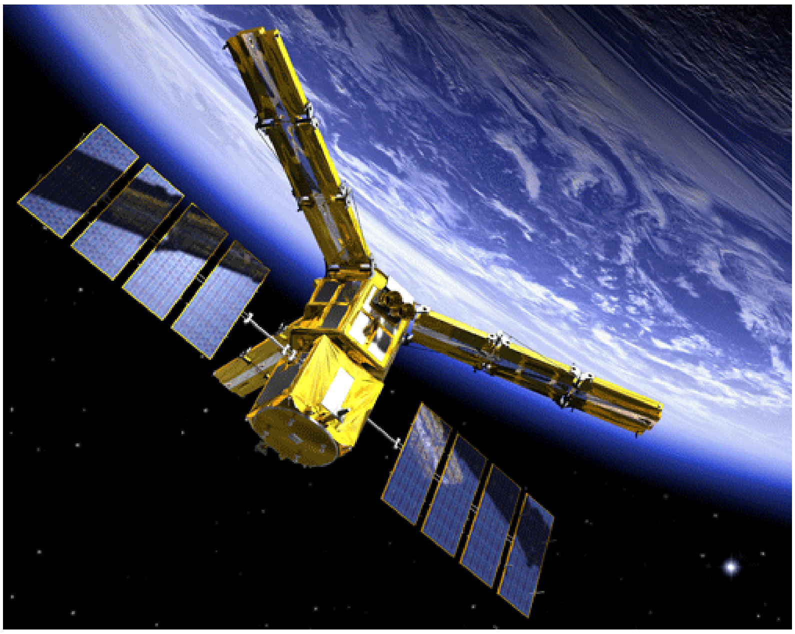

Figure 4-1. An artist's view of the SMOS in the orbit. Courtesy of CNES.

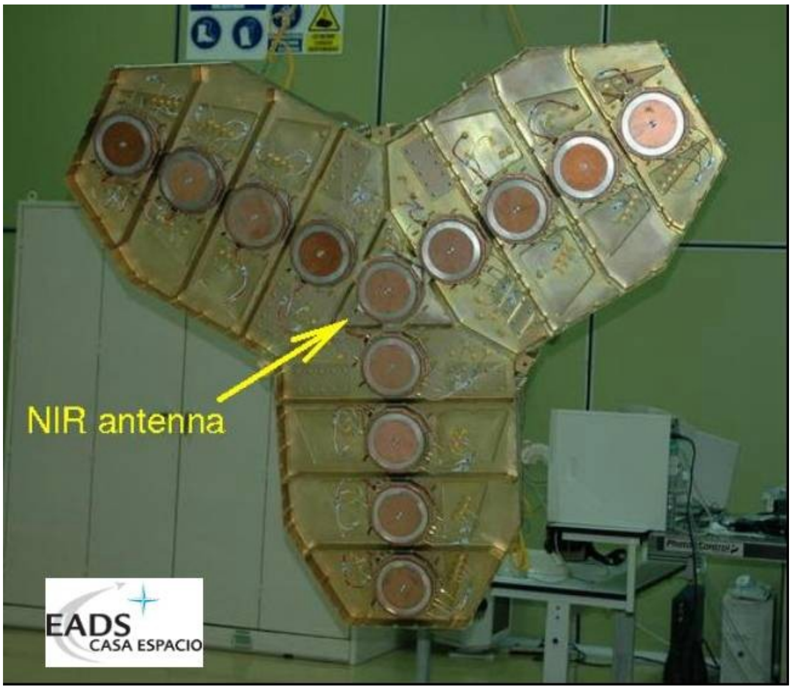

Figure 4-2. A photograph of the AMIRAS instrument, with the NIR in the center. Courtesy of EADS-CASA Espacio.

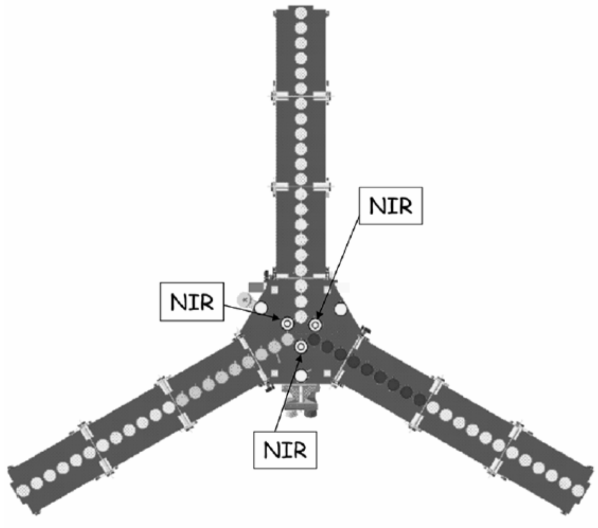

Figure 4-3. The mechanical configuration of the MIRAS instrument. The reference radiometers are located in the center, or the hub, of the satellite. Courtesy of EADS-CASA Espacio.

Figure 4-4 shows a schematic diagram of the V-channel of the NIR. The basic blocks of the controller are bias circuitry, which generates the required voltages and provides EMC protection (omitted in the figure); two noise injection circuitries with couplers (for vertical and horizontal polarization channels), and an FPGA circuitry, which controls the noise injection circuitry and front-end switches of the NIR receivers. Appendix B shows a more detailed description of the planes and connections of NIR Flight Model.

In Figure 4-4, 1B/2L stands for one-bit/two-level digital output for the correlator; PWR is a detector signal to retrieve system temperature, and LINP stands for Length of Injected Noise Pulse. Note that there are two alternative paths for the noise injection into the receivers: one through the antenna branch, for antenna temperature measurement, and one directly to the front-end switch of the receivers, for the CAS noise temperature measurement. There is a switch in the receivers to select between different input signals, namely (1) the noise injection signal for the CAS measurement, (2) the antenna signal, (3) the matched load (U- or Dicke load), and (4) the CAS signal.

A NIR-unit consists of (1) two radiometer receivers, one for vertical and one for horizontal polarization, (2) a controller, (3) four phase-stable low-loss RF cables that connect the controller to the receivers, and (4) an antenna that receives the target noise. The NIR receivers are almost identical to the other receivers of AMIRAS and MIRAS, and have been manufactured by MIER Telecomunicaciones, Spain. Also, the antenna is identical to those of the other antennas of AMIRAS and MIRAS (manufactured by RYMSA, Spain). Figure 4-5 shows a schematic diagram of the placement of a NIR-unit in the payload with the rest of MIRAS.

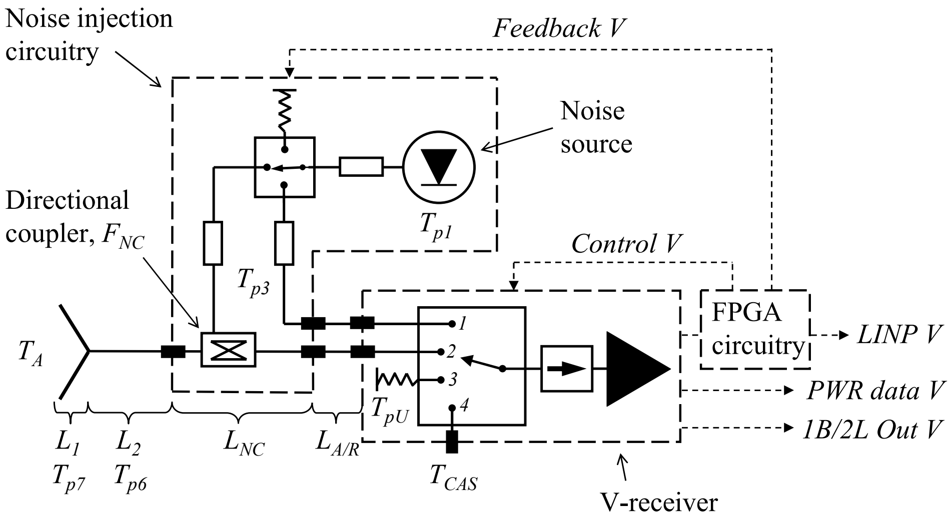

Figure 4-4. Schematic diagram of the V-channel of the NIR. The H-channel is identical. In the diagram, L stands for loss, T_p for physical temperature, T_A for antenna temperature and T_{CAS} for CAS noise temperature. The symbols are discussed in detail in Sections 4.1.1.1 and 4.1.2. Note that in the space flight model there are actually two switches in series to control the noise injection, in order to improve the isolation of the switching; one of the switches is excluded in the schematic for clarity.

The NIR has a set of requirements that are based on the SMOS mission requirements. Table 4-1 lists some of the key performance parameters. Especially noteworthy is the requirement for stability; 0.02 K/°C is a very stringent value, considering the absence of an active thermal stabilization system at subsystem level, as well as the budgetary and schedule constraints set for the development.

In this Chapter the operation of the reference radiometer, or the NIR, is first discussed. Both the operation of the antenna measurement and the CAS measurement are presented. Then, the calibration of the reference radiometer is discussed in detail. Special attention is paid to the method for end-to-end phase imbalance calibration. Finally, the contribution of this work on the polarimetric and interferometric radiometer technology and calibration is evaluated.

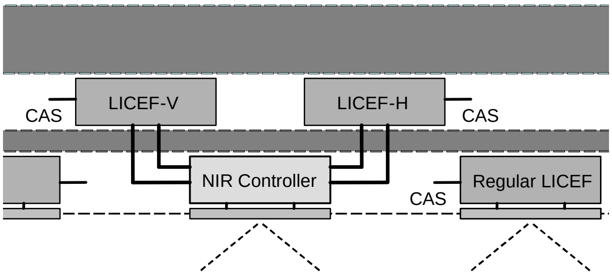

Figure 4-5. A schematic diagram of a NIR unit on-board MIRAS. One NIR radiometer consists of two LICEF units, phase-stable low-loss cables, a controller and an antenna that is identical to those in the regular LICEF-units.

Table 4-1.Key performance requirements of the space flight model of the NIR (resolution is defined at 1.2 s integration time)

Parameter	Value
Receiver noise temperature	275 K
Resolution, H and V	0.25 K
Resolution, 3rd and 4th	0.55 K
Stability	0.2 K/°C
Stability (with compensation)	0.02 K/°C
Channel isolation	> 40 dB

4.1 Operation of the reference radiometer

This Section presents the operational principles and equations of a NIR-unit. First the general aspects are addressed, then equations of the retrieval of fully polarimetric antenna temperature are presented and, finally, the equations for the measurement of CAS noise levels are laid out.

The NIR operates by injecting, or adding, a known and constant amplitude noise temperature pulse to the antenna signal. The level of the combined antenna signal and the injected noise is adjusted to achieve a balance with respect to a reference, or Dicke, load. This adjustment is accomplished by adjusting the length of the pulse. Both Dicke half cycles being balanced, the method removes the effect of the receiver gain and offset variations, as explained in Section 2.2.1. The length of the noise injection pulse is then proportional to the antenna temperature. The amount of the injected noise is controlled by the FPGA, i.e. the feedback loop is controlled digitally. The control is based on the calculation of the noise difference between the two Dicke half cycles, and adjusting the change of the noise injection level based on this. One important benefit of the digitally controlled loop is the fact that there is practically no possibility for the control loop to start oscillating.

The NIR has several operational modes for measuring the antenna and CAS noise temperature and for calibration. The antenna temperature is measured using a noise injection mode called NIR-A mode, and the CAS noise level is measured using a noise injection mode called NIR-R mode. The NIR-R mode is in turn calibrated using a mode called NIR-AR. Figure 4-6 presents a schematic diagram of the power detector output of one receiver in NIR-A, NIR-R and NIR-AR modes; this demonstrates how the noise injection balances the input of the radiometer. Furthermore, total power modes are used, for example, for solving the receiver noise temperature. Table 4-2 lists the operational modes of the NIR. For the measurement of the receiver noise temperature, two modes are used: one has the intermediate frequency (IF) attenuator on (LICEF-LC2) and the other has it off (LICEF-LC) in order to apply the so-called four-point method (see Section 2.2.1). The calibration is discussed in more detail in Section 4.2.

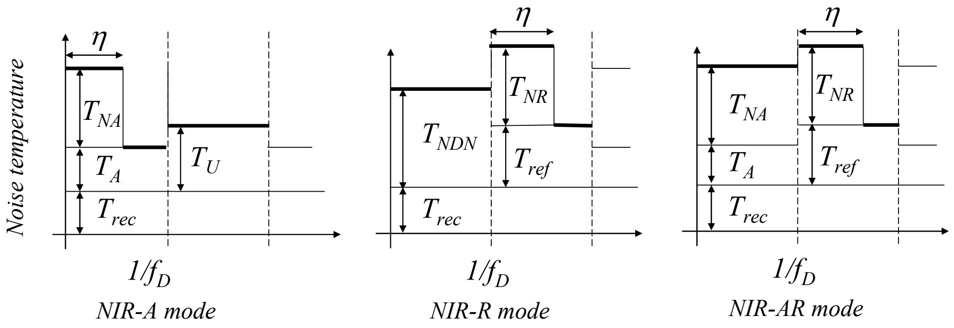

Figure 4-6. Operational modes of the NIR for one receiver. NIR-A mode is for measuring the antenna temperature, NIR-R mode for measuring the noise temperature of CAS, and NIR-AR mode is for calibration of the NIR-R mode. One Dicke cycle is the period 1/f_D, and η is the length of the noise injection. See text for explanation of other symbols.

Table 4-2.The operational modes of the NIR (M/C stands for measurement mode or calibration mode).

Mode	**M/C**	**Purpose**
NIR-A	M+C	Measurement of antenna temperature, T_A, and calibration of antenna injection, T_{NA}
NIR-R	M	Measurement of CAS noise level, T_{CAS}
NIR-AR	C	Calibration of reference injection, T_{NR}
LICEF-LC	C	Measurement of receiver noise temperature (IF-attenuator OFF), T_{rec}, and receiver phase imbalance Θrec
LICEF-LC2	C	Measurement of receiver noise temperature (IF-attenuator ON), T_{rec}
LICEF-LU	C	Measurement of residual offset, V_U
LICEF-LA	C	Measurement of Corbella correlation (see Section 4.2.1), V_C

The equations for NIR operation are presented in the following subsections. The model for the loss characterization of the front-end of the NIR follows the principle of the theory of the radiative transfer, i.e. [3],[51]:

$$T' = \frac{T}{L} + \left(1 - \frac{1}{L}\right) T_{phys} , \tag{4-1}$$

where T is the input noise temperature of a passive network, T' is the output noise temperature, T_{phys} is the physical temperature of the loss L, which is the loss causing the equivalent noise temperature of the passive network. This is defined at the input of the network as: [3],[150],[151]:

$$T_e = (L-1)T_{phys} = \left(\frac{1-|S_{22}|^2}{|S_{21}|^2} - 1\right)T_{phys}, \tag{4-2}$$

where S refers to the scattering parameters of the network. This yields for the relation between the loss parameter and the scattering parameters:

$$L = \frac{1-|S_{22}|^2}{|S_{21}|^2}, \tag{4-3}$$

This definition is used for the loss, L, in the subsequent sections (as opposed to using S_{21} directly) in order to take the matching of the components into account. In order to solve the antenna temperature, the front-end and the antenna are divided in sections, as shown in Figure 4-4. This is done to account for the facts that the noise injection level, T_{NA}, needs to be determined in the calibration, and that the controller, cables and receivers are located in different thermal environments, as can be seen in Figure 4-5.

4.1.1 Polarimetric measurement with noise injection radiometer

In this Subsection, the measurement of the polarimetric brightness temperature with the reference radiometer is described. First, the measurement of the principal polarizations is described, then the method for solving the 3rd and 4th Stokes parameters is laid out, and finally, an experiment validating the polarimetric operation is presented.

4.1.1.1 Measurement of brightness temperature

As explained above, the measurement operation of the NIR is based on injecting noise so that the output is balanced on average to the level of the U-load, T_U [3]. This can be written as follows:

$$T_U^{LCIP} = \eta T_{A|ON}^{LCIP} + (1-\eta) T_{A|OFF}^{LCIP}, \tag{4-4}$$

where T_U^{LCIP} is the noise temperature of the U-load at the output plane of the Dicke switch (LCIP; see Figure 4-4 and Appendix A); $T_{A|ON}^{LCIP}$ and $T_{A|OFF}^{LCIP}$ are the noise temperatures of the antenna branch at the output plane of the Dicke switch, when the noise injection is on and off, respectively. The antenna noise temperature can be solved from this equation using the following formulation:

$$T_A = A\tau_A + B, \tag{4-5}$$

where A and B are called the calibration parameters of the NIR-A mode. The definition of A and B depends on which characteristics of the front-end are accounted for in the calculation. In the processing of the NIR prototype the effect of the coupler was taken into account explicitly. However, in the case of the NIR Flight Model (FM) an approximation was used for the coupler, since the calibration also includes the non-linearity correction, which accounts for this. Below, the equations are written as they are formulated for the NIR FM. Appendix A shows the formulation used for the NIR prototype. The parameter *A* is defined as:

$$A = -L_1 L_2 T_{NA}, \tag{4-6}$$

where L_1 is the loss of the antenna patch and L_2 is the loss of the intermediate layer of the antenna. The parameter *B* is defined as:

$$B = L_1 L_2 \left[L_{NC} L_A L_{DA} \left(T_{pU} - T_{t2} \right) - T_{t1} \right], \tag{4-7}$$

where L_{NC} is the insertion loss of the coupler (including the connections inside the NIR Controller); L_A is the loss of the cable between the coupler and the receiver; L_{DA} is the loss of the Dicke switch; T_{pU} is the physical temperature of the internal reference load; T_{t2} is the thermal noise of the path from the coupler to the output of the Dicke switch and T_{t1} is the thermal noise of the antenna defined as follows:

$$T_{t1} = \left(1 - \frac{1}{L_1} \right) \frac{T_{p7}}{L_2} + \left(1 - \frac{1}{L_2} \right) T_{p6}, \tag{4-8}$$

where T_{p7} is the physical temperature of the antenna patch and T_{p6} is the physical temperature of the intermediate layer of the antenna, and

$$T_{t2} = \left(1 - \frac{1}{L_{NC}} \right) \frac{T_{p3}}{L_A L_{DA}} + \left(1 - \frac{1}{L_A} \right) \frac{T_{cab}}{L_{DA}} + \left(1 - \frac{1}{L_{DA}} \right) T_{pU}, \tag{4-9}$$

where T_{p3} is the physical temperature of the coupler and T_{cab} is the physical temperature of the cable between the coupler and the receiver approximated with

$$T_{cab} = \frac{T_{p3} - T_{pU}}{2}. \tag{4-10}$$

The level of the noise injection is determined by measuring a known target, T_{A0}, which is the cold sky in the case of the NIR, yielding

$$T_{NA} = \frac{1}{L_1 L_2} \left(\frac{B - T_{A0}}{\eta_A} \right). \tag{4-11}$$

Note that, as analysed in [152], the lower the brightness temperature of the calibration is the more accurate this method is. This is due to the fact that the noise injection length is longer when the target is cold, and hence the uncertainties of the equation above remain smaller. Therefore, the cold sky, with approximately 2.7 K brightness temperature [153], is an ideal calibration target.

4.1.1.2 Measurement of correlation coefficient with blind correlation

Since the NIR uses the noise injection technique to measure the antenna brightness temperature, the so-called blind correlation method was developed and demonstrated in the NIR prototype project in order to denormalize the correlation, while using the noise injection technique. The denormalization of the correlation is done using the so-called modulus term, as explained in Section 2.2.1. When using the noise injection method for the antenna brightness temperature retrieval, additional noise is injected on top of the measured antenna signal. As mentioned in Section 2.2.1, this increases the system noise temperature, and has to be taken into account in the modulus term.

In the noise injection measurement, the Dicke cycle is divided into four steps, in order to take into account the varying amount of noise present during the measurement of correlation. The time steps are defined here as follows:

1. Antenna measurement with the noise injection to both channels
2. Antenna measurement with the noise injection to one channel
3. Antenna measurement without the noise injection
4. Measurement of the Dicke load (resulting in zero correlation)

The measured correlation coefficient, see Equation (2-26), is now written for every time step $p = 1,2,3,4$ yielding:

$$\mu_p = \sin\left(\frac{\pi}{2} Z_p\right), \tag{4-12}$$

where μ_p is the measured correlation coefficient, and Z_p follows Equation (2-25) as:

$$Z_p = \frac{1}{N_p}\sum_{i=1}^{N_p} \operatorname{sign}(x(t_i))\operatorname{sign}(y(t_i)), \tag{4-13}$$

in which N_p is the number of the samples being correlated during the time step.

The ideal correlation coefficient of a time step is retrieved from the measured one using the subsequent relation, which follows Equation (2-27):

$$M_p = \tilde{g}_p \tilde{V}, \tag{4-14}$$

since M_p is written for every time step, the total correlation coefficient can be written as:

$$M = \sin\left(\frac{\pi}{2}\sum_{p=1}^{4}\frac{N_p}{N} Z_p\right), \tag{4-15}$$

which, using Equation (4-12), can be written as

$$M = \sin\left(\sum_{p=1}^{4}\frac{N_p}{N}\arcsin\left(\tilde{g}_p \tilde{V}\right)\right), \tag{4-16}$$

from which $\tilde{V}$ can be solved numerically. Finally, the modulus terms are written for each time step as follows:

$$\tilde{g}_1 = \tilde{r}\sqrt{\frac{T_{A,v}}{T_{A,v} + T_{rec,v} + T''_{NA,v}}}\sqrt{\frac{T_{A,h}}{T_{A,h} + T_{rec,h} + T''_{NA,h}}}, \tag{4-17}$$

$$\tilde{g}_2 = \tilde{r}\sqrt{\frac{T_{A,v}}{T_{A,v}+T_{rec,v}}}\sqrt{\frac{T_{A,h}}{T_{A,h}+T_{rec,h}+T''_{NA,h}}}, \tag{4-18}$$

$$\tilde{g}_3 = \tilde{r}\sqrt{\frac{T_{A,v}}{T_{A,v}+T_{rec,v}}}\sqrt{\frac{T_{A,h}}{T_{A,h}+T_{rec,h}}}, \tag{4-19}$$

where $T''_{NA,v}$ and $T''_{NA,h}$ are the noise injection level in the antenna branch of V- and H-channel, respectively, transformed from the injection point to the antenna input plane. See Appendix B for the details of the plane transformation of the injection and receiver noise temperatures. The equations hold when the noise injection is longer in the V-channel. If the noise injection is longer in the horizontal receiver, the subscript v is interchanged with the subscript h in Equation (4-18).

4.1.1.3 Blind correlation experiment

This Paragraph is focused on the presentation of an experiment to validate the blind correlations concept. The setup, specifically designed for this purpose, is first described, and then measurement results are presented together with simulated theoretical values.

Measurement setup

The goal of the measurement is to create a situation where the NIR can see different Stokes parameters in any of its operational modes. For the experiment, a load producing correlated noise is required. Additionally, the load is required to have noise temperature lower than that of the reference load of the radiometer, in order to have a situation where the length of the noise injection is significant. Figure 4-7 shows a setup fulfilling these requirements. The setup utilizes the fact that a load, which is common for both channels of the radiometer and in a physical temperature different from that of the radiometer, produces correlated noise, which is based on the so-called Bosma theorem [154].

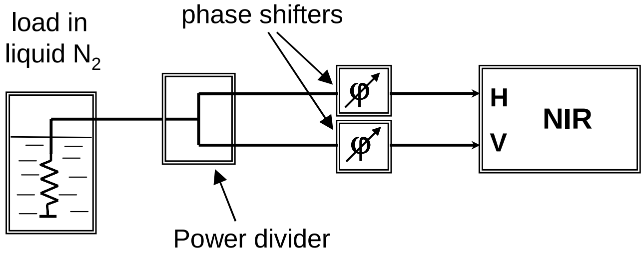

Figure 4-7. A schematic diagram of the measurement setup for the correlation measurements.

The noise temperature emitted by the cold load was determined by measuring the physical temperature distribution of the cable with five temperature sensors. Also, the physical temperatures of the power divider and phase shifters were measured. In this way the input noise temperature could be determined at all times during the measurements. Note that the knowledge of the exact phases of the phase shifters is not required, since the idea is to compare the results obtained in different operational modes, not the absolute value.

Simulated result

The results were also compared to the simulated correlation coefficient values calculated using the theory presented in [96]. This theoretical model predicts the amount of correlated noise in the outputs of a noise distribution network using the S-parameters of the network. In order to do the simulation, the scattering parameters of the connecting network were measured with a VNA and the phase shift values of the phase shifters were determined using the correlator in-phase calibration.

Measured Stokes parameters

The correlation coefficients were obtained in two different measurement modes as presented in Figure 4-8. Furthermore, the Stokes parameters were solved using the previously presented equations yielding the results presented in Figure 4-9.

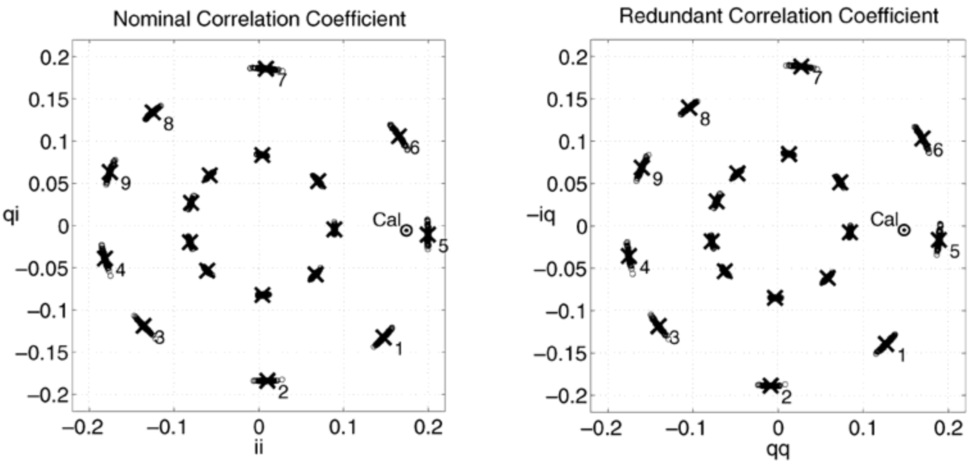

Figure 4-8. Nominal and redundant correlation coefficient (on the left- and right-hand side, respectively) measured at different phase shifts between horizontal and vertical channels. The measurement used for offset and phase calibration is marked with text Cal. The coefficients on the outmost circle are measured in the total power mode (NIR-TP mode) and those on the innermost in the noise injection mode (NIR-A mode).

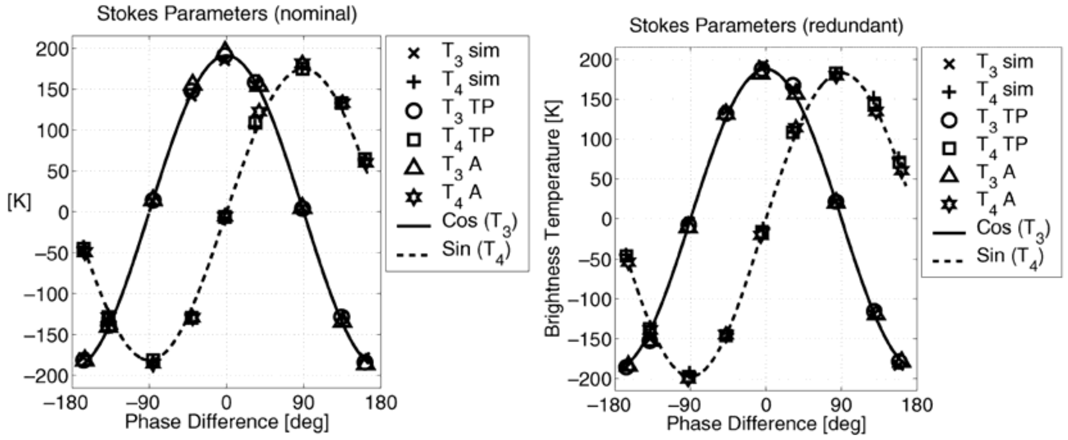

Figure 4-9. Measured third and fourth Stokes parameters in the total power mode (TP), noise injection mode (A), and the simulated Stokes parameters (sim) with Sine and Cosine functions for illustration.

In Figure 4-8 the effect of the so-called blind correlation can be clearly seen. The coefficients on the outmost circle are measured in the total power mode (NIR-TP mode) and those on the innermost in the noise injection mode (NIR-A mode), which is logical, since the magnitudes (i.e., the different radii in the figure) of the correlation coefficients depend on the ratio of the correlated noise and the total noise.

Figure 4-9 shows that the simulations and the results obtained both in the total power mode (NIR-TP mode) and in the noise injection mode (NIR-A mode) are in good agreement. The value of the third and fourth Stokes parameters varies between -200 K and 200 K. For the higher values of the third and fourth Stokes parameters there is some difference between the blind correlation result and the other results. However, note that the value of the third and fourth Stokes parameter that is measured from natural targets is only in order of a few Kelvins, hence making the result acceptable.

4.1.2 Measurement of internal noise source of synthetic aperture radiometer

In this Subsection, the equations for retrieval of the magnitude of an internal noise source, or a noise distribution network, of a synthetic aperture radiometer using the NIR are described. The method was developed in MDPP-2 project [P2]. First, the measurement mode is analysed, and then the equations of a dedicated calibration mode are presented.

Measurement mode

The measurement of the levels of the internal distributed noise source, CAS, is done by injecting noise to the reference channel so that the input is balanced to the level of CAS. This can be formulated as follows:

$$T_{CAS} = \eta_R \, T_{ref|ON}^{LCIP} + \left(1 - \eta_R\right) T_{ref|OFF}^{LCIP} , \qquad (4\text{-}20)$$

where η_R is the noise injection length in NIR-R mode; $T_{ref|ON}^{LCIP}$ and $T_{ref|OFF}^{LCIP}$ are the noise temperatures of the reference branch at the output plane of the Dicke switch when the noise injection is on and off, respectively. The CAS noise temperature can be solved from this equation using the following formulation:

$$T_{CAS} = A_R \eta_R + B_R , \tag{4-21}$$

where A_R and B_R are the calibration parameters of the NIR-R mode. The definition of A_R and B_R depends again on the characteristics that are accounted for in the calibration. In the case of the NIR prototype, for example, the loss and isolation of the noise injection switch was explicitly taken into account, but in the case of the NIR space flight model, a more straightforward model is used; the loss and isolation did not prove to have significant impact on the accuracy of the measurement. The formulation used for the NIR prototype is presented in Appendix A, and the formulation of the space flight model is shown here. The calibration parameter A_R is written as

$$A_R = \frac{T_{NR}}{L_R} \frac{L_{DC}}{L_{DR}} , \tag{4-22}$$

where T_{NR} is the level of the noise injection; L_{DC} and L_{DR} are the loss of the Dicke switch in CAS measurement and noise injection positions, respectively, and L_R is the loss of the cable through which the noise is injected. The calibration parameter B_R is written as

$$B_R = \frac{T_{p3}}{L_R} \frac{L_{DC}}{L_{DR}} + T_{t3} , \tag{4-23}$$

where T_{p3} is the physical temperature of the reference load used in the NIR-R mode and the thermal noise of the noise injection channel, T_{t3}, can be written as:

$$T_{t3} = \left(1 - \frac{1}{L_R}\right) \frac{L_{DC}}{L_{DR}} T_{cab} + \left(1 - \frac{L_{DC}}{L_{DR}}\right) T_{pU} . \tag{4-24}$$

Calibration mode

The calibration of the NIR-R mode includes the determination of the noise injection temperature T_{NR}. This is done in the NIR-AR mode [P2]. The mode uses the reference channel noise injection to balance the input to the level of the antenna branch, which is pointing to a known target and having full-length noise injection, T_{ANA}:

$$T_{ANA} = \eta_{AR} T_{ref|ON}^{LCIP} + \left(1 - \eta_{AR}\right) T_{ref|OFF}^{LCIP} , \tag{4-25}$$

where τ_{AR} is the noise injection length in the NIR-AR mode. The noise injection level can now be determined from the following equation:

$$T_{NR} = \frac{L_R L_{DR}}{\eta_{AR}} \left(T_{ANA} - \frac{T_{p3}}{L_R L_{DR}} - T_{t3} \right) . \tag{4-26}$$

4.2 Calibration of the reference radiometer

This Section presents the approach used for the calibration of the NIR, details the principles used especially for the ground calibration, and finally, shows the ground calibration results.

4.2.1 Calibration approach

The calibration approach for the reference radiometer includes two steps; (1) certain parameters are characterized on the ground and (2) these parameters are applied during orbital calibration, which is carried out frequently. The orbital calibration is based on the measurement of the cold sky, which has a well-known brightness temperature level. The cold background noise of space is measured during the external calibration procedure of SMOS, in which the entire satellite is pointed to measure the cold space for a period of about half an orbit.

Figure 4-10 shows a block diagram of the orbital calibration of the NIR. In the figure, black rectangles depict measurements in the various modes of the targets. The key measurements (cold sky in the NIR-A and NIR-AR modes) are shown at the top of Figure 4-10. These measurements are made in order to determine the noise injection levels T_{NA} and T_{NR}. This process involves ground calibration parameters, which are depicted in the figure with gray circles using dashed lines. The black ellipses indicate the solving of the end products: polarimetric antenna temperature, CAS noise level and correlations for the mixed baselines (which are not discussed in detail here). These steps also include the application of ground calibration parameters (gray circles with dashed lines).

Furthermore, there are measurements in the LICEF-LC and -LC2 modes, which measure the two levels of CAS (with the IF-attenuator off and on, respectively, in order to apply the four-point method, see Section 2.2.1 and Appendix B) for the receiver noise temperature and phase imbalance measurements (for the phase imbalance measurement only one noise level is required). The measurement of the cold sky is also performed in the LICEF-LA mode. This is for determining the so-called Corbella correlation, which is due to the finite isolation between the channels over antenna ([P2],[48]). Finally, there is a measurement in LICEF-LU mode, in which both channels of the NIR measure the matched loads, also known as the Dicke loads or uncorrelated loads, inside the receivers, in order to determine the residual correlation offset. Each of these steps also includes the application of the ground calibration parameters.

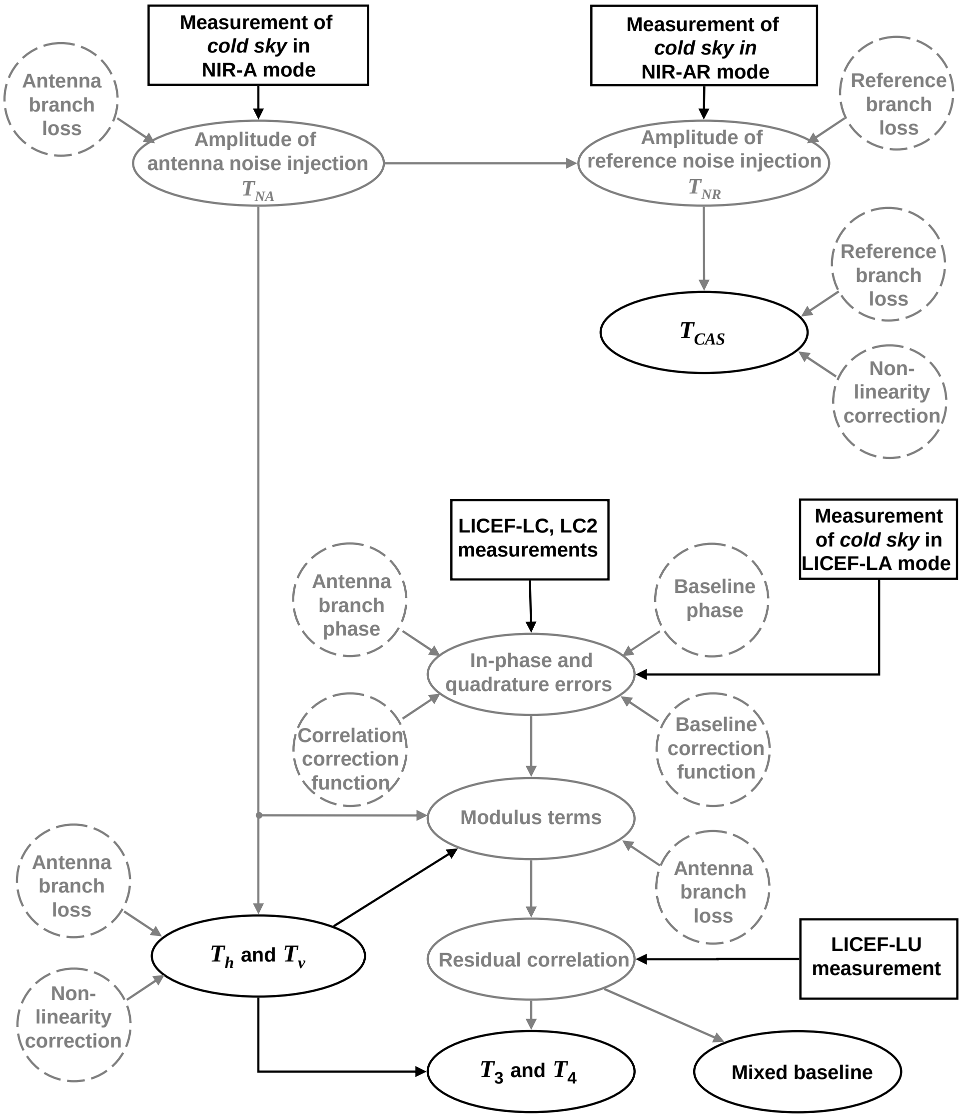

Figure 4-10. The calibration flow chart for the reference radiometer. The black rectangles depict measurements, gray ellipses depict the solving of intermediate parameters, black ellipses depict the solving of the end products, and the gray circles using dashed lines depict the application of the ground calibration values. Certain operational modes are mentioned in the black rectangles; NIR-A mode for solving the noise injection level for antenna measurement (and for solving antenna temperature), NIR-AR mode for solving the noise injection level for CAS measurement, LICEF-LC and LICEF-LC2 modes for measuring the CAS so that the IF-attenuator of the receiver is off and on, respectively, LICEF-LA for measuring the antenna temperature in total power mode and LICEF-LU for measuring the uncorrelated load.

The ground calibration was performed on each NIR-unit individually. The following parameters were solved: (1) antenna and front-end loss, (2) the phase imbalance between V- and H-channels (or *V-H* phase imbalance) of the antenna and front-end, (3) non-linearity correction, and (4) the temperature dependency of the noise injection level. These parameters are applied during orbital calibration when the level of the noise injection, receiver noise temperature and *V-H* phase imbalance of the channels are solved. After this, the correction for the non-linearity is applied to the measured level of brightness temperature. The calibration of the mixed baselines is out of the scope of this work.

4.2.2 Calibration principles

This Section presents the details of the calibration principles of the NIR. The focus is on the calibration of the correlation, front-end phase parameters, front-end loss parameters, non-linearity parameters, and temperature dependency.

Correlation

The measurement of the correlations requires the calibration of following parameters before the 3rd and 4th Stokes parameters can be solved: (a) normalized quantizer offset voltages, (b) quadrature error, (c) in-phase error, (d) residual offset, (e) fringe-washing factor, and (f) self-interference or Corbella correlation.

The calibration of (a) and (b) is done as shown in [94] [3], and (c) is solved as presented in [47] [4]. Parameter (d) is solved using the denormalized correlation obtained from the U-load [94]. For the calibration of (e), the method introduced in [97] [5] is used, and (f) is solved by a measurement of an uncorrelated target [P2] [6].

Phase imbalance

Two separate setups are needed for solving the *V-H* phase imbalance of the front-end and the antenna. The difference of the phases of the correlations measured with the two setups yields the *V-H* phase imbalance of the front end. See Figure 4-11 for clarification. The *V-H* phase imbalance of the section in front of the receivers can be solved as:

$$\Delta\Theta = \arg(\mu_2) - \arg(\mu_1), \tag{4-27}$$

where $\Delta\Theta$ is the *V-H* phase imbalance of the front-end section (between *Plane 1* and *Plane 2*), and μ_2 and μ_1 are the correlations measured with and without the front-end section, respectively. Note that, in order for this formulation to work, either the correlations μ_1 and μ_2 have to be measured using the same source or the correlations have to be in-phase calibrated (see, for example, [47]).

---

[3] The quantizer offset is solved using the correlations against pure "1" or pure "0" signal, and the quadrature error is solved from the self-correlations of the receivers, i.e., the correlation between in-phase and quadrature channel of the same receiver.

[4] The in-phase error is solved using the distribution of a reference signal to all receiving channels.

[5] The method introduced in [97] includes correlation measurements at three different time lags in order to estimate the shape of the fringe-washing function.

[6] The uncorrelated target, with a physical temperature different from that of the receiver, gives by definition the magnitude of the Corbella correlation [48].

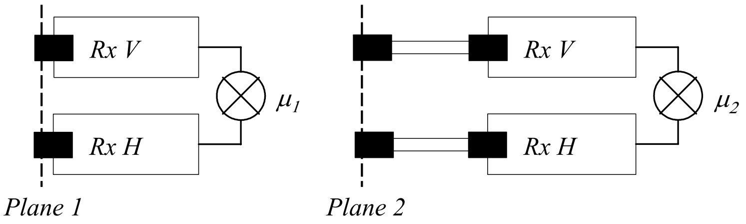

Figure 4-11. The principle for solving the V -H phase imbalance between Plane 1 and Plane 2 is based on measuring a correlated source connected to these planes.

A correlated noise source connected to the two receivers of the radiometer can be used for the measurement when the antenna is not included. However, when the antenna is included, the measurement of the *V-H* phase imbalance on this plane is more complicated. The so-called dual-angle method, presented in detail in Section 4.3, can be used for this.

Loss parameters

In order to solve the loss of the different sections of the front-end, the receiver noise temperature is measured in two planes; in the incoming plane and in the outgoing plane of this particular section of the front-end. See Figure 4-12 for clarification.

For the measurement of the receiver noise temperature, ambient and cold loads are used; either matched coaxial loads or reference antenna targets, depending on the type of the section under study. The return loss of the coaxial loads is measured to be over 30 dB. The cold coaxial load is cooled down with liquid nitrogen and the temperature distribution in the connecting cable is measured and compensated for using the loss of the cable [155]. The return loss of the antenna targets is estimated to be better than 30 dB, based on the reflection coefficient of the applied absorber material (with 25 cm pyramids), which is specified to be 35 dB at the frequency band.

The loss is solved as follows using the definition for the equivalent noise temperature and receiver noise temperature [3]:

$$T_{rec2} = T_e + LT_{rec1} = (L-1)T_{phys} + T_{rec1}, \tag{4-28}$$

yielding

$$L = \frac{T_{rec2} + T_{phys}}{T_{rec1} + T_{phys}}, \tag{4-29}$$

where L is the loss, T_{rec2} and T_{rec1} are the receiver noise temperatures with and without the loss in front of the receiver, respectively, and T_{phys} is the physical temperature of the loss element.

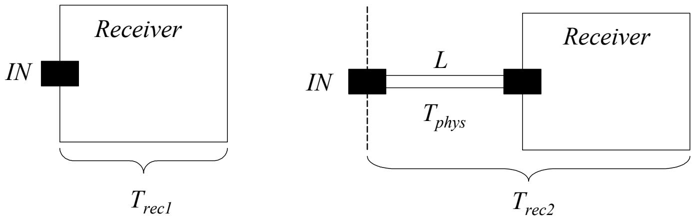

Figure 4-12. The principle for solving the loss of the front-end connections of the radiometer.

Non-linearity

There are two sources of error that are taken into account in the so-called non-linearity correction. The first is the non-linearity of the detector of the receiver and the second is the fact that the coupling of the directional coupler is assumed to be an ideal adder in the equations of operation. To this end, the technique presented in [90], and modified in [156], is applied here to the case of a noise injection radiometer.

Figure 4-13 shows a schematic diagram of the measurement setup used in this technique. The idea is to add a constant amount of noise on top of a noise level that can be varied. The benefit of this method is the fact that the only critical parameter for the accuracy of the measurement is the stability of the added noise, which is achieved relatively easily.

The linear and quadratic correction is applied to the antenna temperature as follows:

$$\hat{T}_A = T_A + T_{lin}, \tag{4-30}$$

where $\hat{T}_A$ is the corrected antenna temperature, T_A is the antenna temperature before the correction is applied, and

$$T_{lin} = c(T_A - T_{A0}) + d(T_A - T_{A0})^2, \tag{4-31}$$

in which c is the linear correction term, d is the quadratic term and T_{A0} is the antenna temperature during calibration.

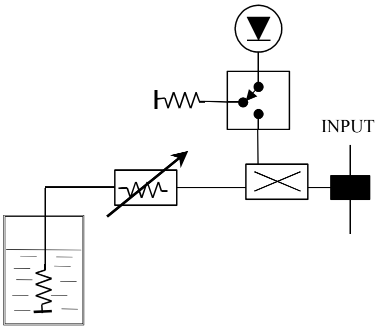

Figure 4-13. The setup for measuring the non-linearity. The noise from the noise diode is added on top of the noise coming from the cold load cooled with liquid nitrogen. The noise level from the cold load can be varied using the controllable attenuator.

Using Equations (4-5) and (4-31) the length of noise injection can be written as:

$$\eta^{off} = \left[\hat{T}_A - B - c\left(T_A - T_{A0}\right) - d\left(T_A - T_{A0}\right)^2\right]\frac{1}{A}, \tag{4-32}$$

where η^{off} is the length of the noise injection when the additional noise is off. When the additional noise is on the length of the noise injection is written as

$$\eta^{on} = \left[\hat{T}_A - B - c\left(T_A + \Delta T - T_{A0}\right) - d\left(T_A + \Delta T - T_{A0}\right)^2\right]\frac{1}{A}, \tag{4-33}$$

in which ΔT is the amount of the additional noise. Now, the difference between the situations when the noise injection is off and on can be solved. This equation allows us to write the difference in the form of a straight line:

$$\Delta\eta = \eta^{off} - \eta^{on} = \frac{2d\Delta T}{A}\left(T_A - T_{A0}\right) + \frac{1}{A}\left(d\Delta T + c - 1\right) = k_1\left(T_A - T\right) + k_2, \tag{4-34}$$

where k_1 and k_2 are the slope and offset of the line, respectively. Now, using these coefficients the parameters c and d can be solved:

$$c = \frac{A}{\Delta T}k_2 - d\Delta T + 1, \tag{4-35}$$

and

$$d = \frac{1}{2}\frac{A}{\Delta T}k_1, \tag{4-36}$$

The slope of the line, k_1, determines the quadratic term, and parameters k_1 and k_2 together determine the linear term. Note that A is actually the level of the noise injection, and that its changes cause only second-order uncertainty to the correction. A similar set of equations is derived for the CAS measurement.

Temperature dependency

A study of the temperature sensitivity of the prototype of the NIR is presented in [155]. Some results for the Engineering Model are presented in [157] (note, however, that the conclusion on the effect of the antenna patch was overruled in the Flight Model test campaign). The results showed that the fit of a linear correction model to the data points was very good (i.e. low scatter and good repeatability). The applied linear model accounts also for all the changes of loss and matching of every component correcting the fixed-loss model. Several correction models, with respect to the fixed-loss model, were studied with the prototype [155], which took the temperature changes of different components into account independently. The results showed that the model based only on the temperature of the noise source was as accurate as the models based on several measured temperatures.

The correction model is acquired by measuring a known noise source connected to the antenna output plane (which excludes the antenna from the measurement) while the physical temperature of the NIR is cycled. Additionally, the effect of the antenna and its connection is modeled in orbit during the commissioning phase of the mission. However, their effect is expected to be very small, or even negligible.

4.2.3 Ground calibration results

In this Subsection, the ground calibration results, obtained in the ground characterization and calibration campaign, are presented. The results include antenna and front-end phase imbalance; antenna and front-end loss parameters; non-linearity correction, and temperature dependency of the noise injection.

Antenna and front-end phase imbalance

Table 4-3 shows the *V-H* phase imbalance of the front-end (between antenna output plane and input plane of LICEF-units) and of the antenna for nominal and redundant correlations. For comparison, the *V-H* phase imbalance of the front-end was also measured with a VNA showing very similar results. However, the absolute phase measurement accuracy of the VNA measurement (>1°) is worse than the accuracy of the characterization measurement that uses correlations (<0.1°).

The results for NIR-1 and NIR-2 *V-H* phase imbalance are relatively equal, but the result for NIR-3 is different. A potential explanation lies in the manual manufacturing processes. Note that the fact that the loss imbalance in NIR-3 is significant (see the next Paragraph) can explain the different *V-H* phase imbalance as well.

Table 4-3. V-H phase imbalance (for nominal and redundant correlations) of the antennas and the front-end connections

	Receiver Plane Nominal (Redundant) Θ_{rec} [°]	**Antenna Plane Nominal (Redundant)** Θ [°]	**Difference Nominal (Redundant)** $\Delta\Theta$ [°]
NIR-1	-49.7 (40.3)	-38.0 (-37.6)	11.7 (11.7)
NIR-2	-49.3 (-48.3)	-41.9 (-40.3)	7.4 (8.0)
NIR-3	-29.1 (-30.2)	-11.1 (-11.3)	18.0 (18.9)

Antenna and front-end loss

Table 4-4 lists the loss parameters of the antenna and the connection between the antenna output planes and the input planes of the LICEF-units. For comparison, the loss was also measured with a vector network analyzer (VNA), also shown in Table 4-4. The accuracy of the VNA measurement is specified to be 0.05 dB for normal range measurements, but for this kind of low-loss measurements it is worse than that; the accuracy of the radiometric characterization measurement is in the order of 0.01 dB. However, the results of Table 4-4 show very similar values (within 0.02 dB) for every other channel except H-channel of NIR-3 (0.06 dB). The result shows that the radiometric measurement also accounts for the matching of the front-end, which is critical. Furthermore, the measured loss is in agreement with the requirement for the receiver noise temperature and radiometric resolution.

In general, the front-end losses show very similar values for the V- and H-channels; the only exception is NIR-3, which shows a small (0.10 dB) difference. A potential explanation for the loss imbalance of NIR-3 is the manufacturing process, which includes many manual steps. These are prone to small variations, which can lead to imbalance if summed up.

Table 4-4. Loss of the front-end connections and antennas derived with radiometric measurement and also loss of the front-end connections derived from S-parameters

	S_{21}^{NC} [dB]	S_{22}^{NC} [dB]	S_{21}^{A} [dB]	S_{22}^{A} [dB]	L_S [1] [dB]	L_C [2] [dB]	L_{ant} [3] [dB]
NIR-1 V	-0.28	-18.8	-0.16	-29	0.38	0.38	0.20
NIR-1 H	-0.24	-19.2	-0.16	-29	0.34	0.36	0.17
NIR-2 V	-0.27	-19.4	-0.16	-29	0.37	0.35	0.17
NIR-2 H	-0.30	-18.0	-0.16	-29	0.38	0.36	0.12
NIR-3 V	-0.32	-17.0	-0.16	-29	0.38	0.38	0.12
NIR-3 H	-0.32	-18.3	-0.16	-29	0.42	0.48	0.16

1) Front-end loss $\left(L_S = L_S^{NC} + L_S^{A}\right)$ determined using Equation (4-3).

2) Front-end loss $\left(L_C = L_{NC} + L_A\right)$ determined in one piece using the radiometric measurement (Section 4.2.2).

3) Antenna loss $\left(L_A = L_1 + L_2\right)$.

Non-linearity correction

Table 4-5 presents the non-linearity correction parameters for all three NIR units. V- and H-channels have a systematic difference, which is explained by the different layout of the channels. Figure 4-14 shows the non-linearity correction for V- and H-channels of NIR-1 as an example. A calibration target of about 120 K, which is the output noise temperature of the coaxial reference load used in the measurement, is assumed. The correction is, at maximum only slightly over 1 K, V- and H-channels having very similar curves.

Figure 4-15 shows examples of the fitted lines of Equation (4-34) with slope of k_1 and offset of k_2 for V- and H-channels of NIR-1. The deviations from the line are small, indicating the reliability of the method.

Table 4-5. Non-linearity correction parameters for the antenna measurement

	c (10^{-3})	d (10^{-5})
NIR-1 V	4.69	-2.74
NIR-1 H	7.29	-4.28
NIR-2 V	4.30	-2.47
NIR-2 H	10.4	-6.09
NIR-3 V	4.86	-2.92
NIR-3 H	8.34	-5.01

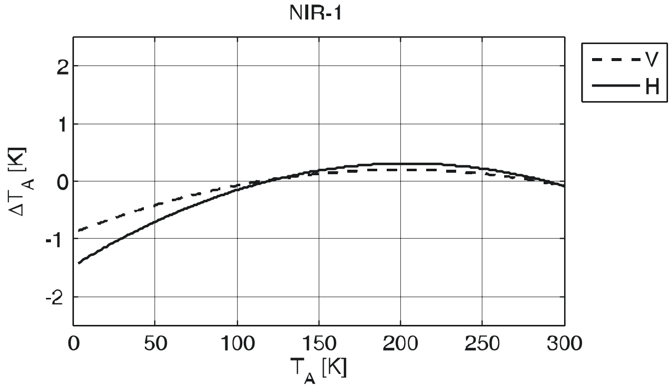

Figure 4-14. A plot of the non-linearity correction of NIR-1 for V- and H-channels as a function of antenna temperature.

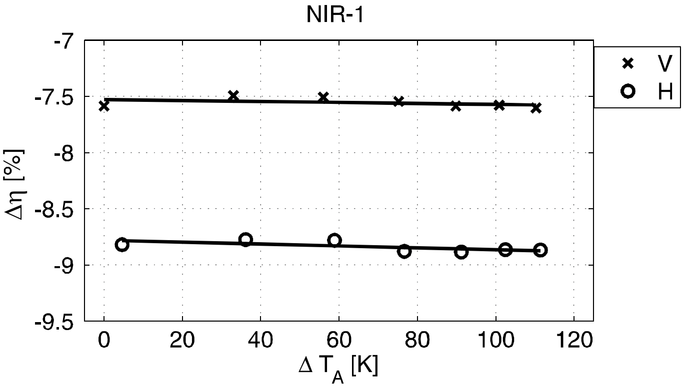

Figure 4-15. The coefficients for the non-linearity correction are solved by fitting the lines, defined by k_1 and k_2, to the measurement points as shown in this figure.

Temperature dependency of noise injection

The thermal cycling for each unit consisted of at least two cycles ranging from +10°C to +40°C, which is the operational range of the subsystem. The results showed that the temperature dependency of the antenna and reference noise injection of both channels of all units is under 0.1%/°C. Due to the fact that the noise injection length (expressed as a fraction of the half of the Dicke cycle) is typically 10% to 40%, the effect of the noise injection variation on the measured antenna temperature is in the order of 0.025%/°C. This can be reduced further by a factor of 5 to 10 using the linear model for the variation of the noise injection level with temperature.

Furthermore, it is important to note that the temperature variation in the orbit is expected to be less than the operational range. Based on the payload level thermodynamical simulations carried out by EADS-CASA Espacio, Spain, the thermal variation of the antenna patch, during one orbit, is around 15°C, that of the controller and the intermediate layer of the antenna is around 2°C and that of the LICEF units is around 1°C. Also, the thermal gradient is expected to be very constant between the different components.

Calibration experiment with Engineering Model

An experiment to validate the calibration approach was conducted with the engineering model using the sky and a cold antenna target as references. During the experiment sky was clear, and the sun in the horizon. The cold target was an absorber load cooled down with liquid nitrogen (the same target as the one used in the loss measurement).

First, the calibration was performed by a measurement of the sky, and then the cold load was measured in order to compare the measurement result to the predicted brightness temperature. During the experiment the temperature of the NIR varied strongly, and also the gradient between the components changed dramatically, which is not representative for the in-orbit case. For this reason, a dedicated thermal model was used in the analysis of the results.

Figure 4-16 shows the results of the experiment for both V- and H-channels. The down-arrow shows the calibration epoch and the up-arrow shows the epoch during which the cold load temperature is determined. The jumps in the plot are due to the positioning of the radiometer. The obtained cold load values are 77.6 K for the V-channel and 77.9 K for the H-channel. These values correspond well to the predicted values, as the brightness temperature of sky is assumed to be 6.6 K and the temperature of the liquid nitrogen is 77.35 K. This result shows that the concept of the calibration, i.e. one reference target with characterization of the front end, works.

Performance summary

Table 4-6 summarizes the performance of the NIR Flight Model. The noise temperature and radiometric resolution values are within the requirements in all cases. Also, the design of the coupler (by Ylinen Electronics) was very successful; very high isolation could be combined with extremely low loss and small size (10x10x1.3 mm). Furthermore, the isolation between orthogonal channels is very high. Note, however, that the presented figure does not include the cross-coupling of the antenna.

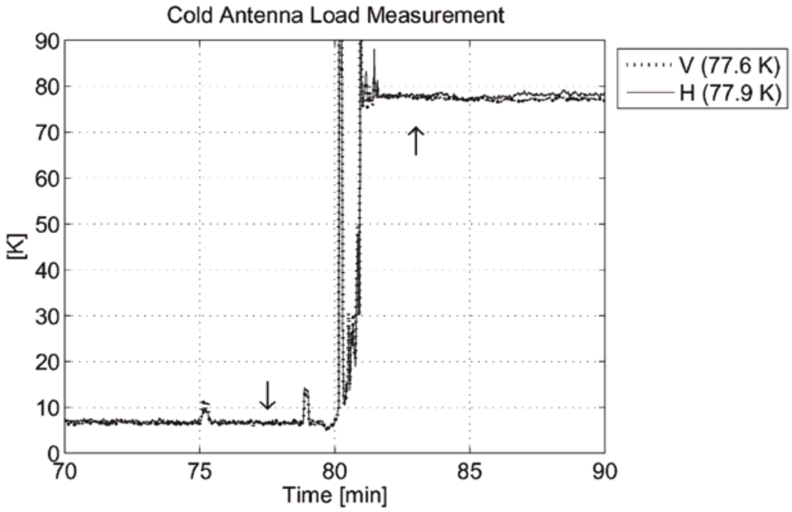

Figure 4-16. The result of the calibration experiment performed with the engineering model. The down-arrow shows the calibration epoch and the up-arrow shows the epoch during which the cold load temperature is determined. The jumps in the plot are due to the positioning of the radiometer, as the orientation of the radiometer was adjusted for the sky and cold load looks.

The stability as a function of the physical temperature does not satisfy the requirement in the cases of NIR-1 and NIR-3. However, the presented values are estimates and the measurement situation was not entirely representative. Furthermore, in the measurement the units were cycled between 10°C and 40°C relatively rapidly; in the orbit the thermal fluctuation of the units is, based on the simulations, around 2°C per orbit (excluding antenna patch surface, which experiences greater excursion). Thus, the performance is considered satisfying in this respect as well.

Table 4-6. Summary of the performance parameters of the space flight model of the NIR (the resolution is defined at 1.2 s integration time).

	NIR-1	**NIR-2**	**NIR-3**
Receiver noise temperature, V	259 K	248 K	260 K
Receiver noise temperature, H	260 K	262 K	252 K
Resolution, V	0.19 K	0.20 K	0.24 K
Resolution, H	0.22 K	0.24 K	0.24 K
Resolution, 3	0.43 K	0.41 K	0.45 K
Resolution, 4	0.43 K	0.49 K	0.41 K
Stability, V[1]	0.086 K/°C	0.007 K/°C	0.043 K/°C
Stability, H[1]	0.066 K/°C	0.007 K/°C	0.040 K/°C
Channel isolation	> 100 dB	> 100 dB	> 100 dB
Coupler[2]:			
Insertion loss V/H	0.16 dB / 0.16 dB		
Isolation V/H	50 dB / 45 dB		

1) With the compensation in the operational range from +10°C to +40°C

2) Measured from samples of the same manufacturing lot

4.3 End-to-end phase calibration method for polarimetric radiometers

For the calibration of the measurement of the 3rd and 4th Stokes parameters, the phase imbalance of the V- and H-channels of the reference radiometer of the SMOS needs to be solved. The phase imbalance means the phase difference between the end-to-end responses of the two receivers of the radiometer. In the simplest case correlated noise is fed to the receivers in-phase, so that the phase of the obtained correlation coefficient equals the phase difference of the receivers (see Section 4.2.2).

However, when the antenna is included, the solution is not this simple, and therefore a method was developed to overcome the problems utilizing measurements of a linearly polarized target at two different angles. In this Section, first the theory is summarized and then a demonstration of the method is presented.

4.3.1 Principle of end-to-end phase calibration

The phase imbalance of the receivers of a polarimetric radiometer can be solved in an ideal case by measuring a pure linearly polarized electromagnetic field at 45° angle with respect to the polarization plane of the antenna of the radiometer. This would yield a complex correlation coefficient, which has phase equal to the phase imbalance of the receivers, since there is no phase difference in the transmitted field. In reality, however, there are two sources of non-idealities, which are:

- Polarization purity of the transmitted field.
- Finite polarization separation and cross-coupling of the antenna of the radiometer.

Both of these sources create a residual offset to the measured correlation. The first is due to the fact that the non-principal polarization transmits undesired radiation and the second is due to the fact that the transmitted field leaks between receivers.

The solution is to rotate the transmitted linearly polarized field with respect to the polarization plane of the antenna of the radiometer by 90°, as is shown in Figure 4-17. By rotating the polarization plane by 90° the phase of the output signal is rotated by 180° as the field vector of one polarization (at antenna plane) changes its sign, as happens for V-polarization in Figure 4-17. The rotation of the phase is demonstrated in Figure 4-18, which shows the measured correlations, M_{+45} and M_{-45}, the offset, M_{off}, and the phase imbalance of the receivers, δ. Note that in the ideal case the amplitudes of the measurements at -45° and +45° angles are equal. With this procedure the non-idealities can be cancelled out as the offset is the same in both measurements and the imbalance can be determined from the slope between the two measurement points.

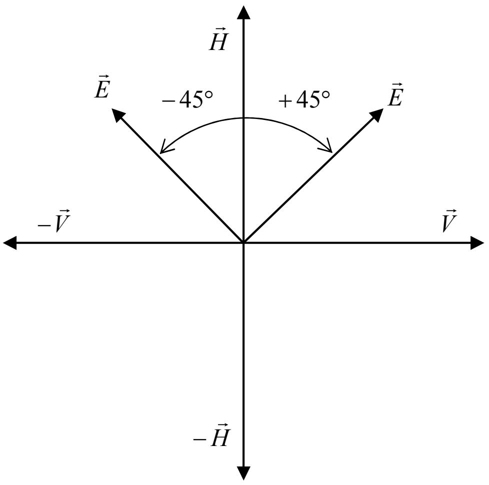

Figure 4-17. The orientation of the polarization plane of the antenna of the radiometer and the measured field E in -45° and +45° angle setups.

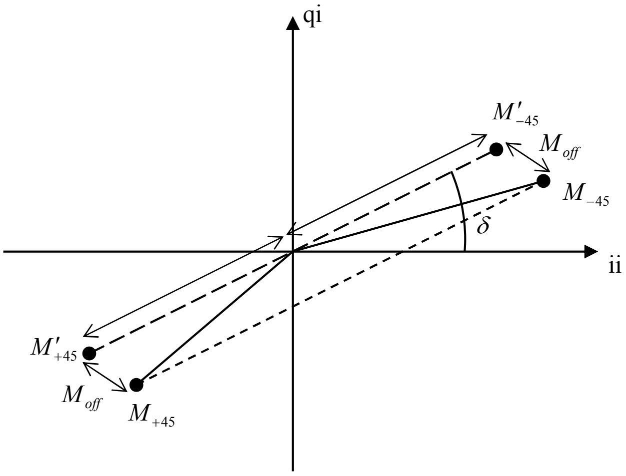

Figure 4-18. The principle of the end-to-end phase difference retrieval: the offset remains the same in the two measurements while the phase of the signal changes by 180°.

In the end-to-end phase difference measurement the measured correlation coefficient between H- and V-channel can be divided into two parts as follows:

$$M = M' + M_{off}\ , \tag{4-1}$$

where the correlation without the offset has an amplitude of

$$M' = \sqrt{\frac{T_{A,v}^{c}}{T_{A,v} + T_{rec,V}}}\sqrt{\frac{T_{A,h}^{c}}{T_{A,h} + T_{rec,h}}}\ , \tag{4-2}$$

where $T_{A,v}^{c}$ and $T_{A,h}^{c}$ are the brightness temperatures of the correlated noise of V- and H-polarization, respectively, and the offset has an amplitude of

$$\begin{aligned} M_{off} &= \sqrt{\frac{T_{A,v}^{c}}{T_{A,v}+T_{rec,V}}}\sqrt{\frac{T_{A,v}^{c}\left|\chi_{VH}\right|^{2}}{T_{A,h}+T_{rec,h}}}+\sqrt{\frac{T_{A,h}^{c}}{T_{A,h}+T_{rec,h}}}\sqrt{\frac{T_{A,h}^{c}\left|\chi_{HV}\right|^{2}}{T_{A,v}+T_{rec,v}}}, \\ &= \frac{T_{A,v}^{c}\left|\chi_{VH}\right|+T_{A,h}^{c}\left|\chi_{HV}\right|}{\sqrt{T_{A,v}+T_{rec,v}}\sqrt{T_{A,h}+T_{rec,h}}} \end{aligned} \tag{4-3}$$

in which χ_{VH} and χ_{HV} are the cross-coupling factors (complex) between channels due to the polarization non-purity, and polarization separation and cross-coupling of the antenna of the radiometer.

Under the assumption that the cross-coupling, brightness temperature of H- and V-polarization and the equivalent noise temperatures of the receivers stay constant, also the offset correlation is constant during the measurement. This makes it possible to cancel the offset out when the measurement is done at -45° and +45° (see Figure 4-18).

Hence, the phase imbalance can be solved from the measured correlation coefficients in a straightforward manner as follows:

$$\Theta = \arctan\left(\frac{M_{-45}\big|_{q,i} - M_{+45}\big|_{q,i}}{M_{-45}\big|_{i,i} - M_{+45}\big|_{i,i}}\right). \tag{4-4}$$

Furthermore, the solution for the offset in the measurement can be considered as the mean value of the two measurements yielding

$$M_{off} = \frac{M_{-45}\big|_{i,i} + M_{+45}\big|_{i,i}}{2} + j\frac{M_{-45}\big|_{q,i} + M_{+45}\big|_{q,i}}{2}. \tag{4-5}$$

4.3.2 End-to-end phase calibration experiment

The above theory was verified with an experiment. This Subsection presents the used measurement setup with a polarimetric radiometer and obtained results, which correspond to the predictions very well.

Measurement setup

The measurement setup consists of the NIR Engineering Model and a linearly polarized antenna target. The linearly polarized antenna target is composed of an absorber load, linearly polarized transmitter antenna at the bottom of the load connected to a noise source through a step attenuator, and a polarizer grid made of wires. Figure 4-19 shows a schematic diagram of the setup.

The purpose of the polarizer grid is to improve the polarization purity of the transmitter antenna, although the presented method cancels out the impurity of the transmitted load. This was confirmed in the experiment as measurements without the grid were carried out as well.

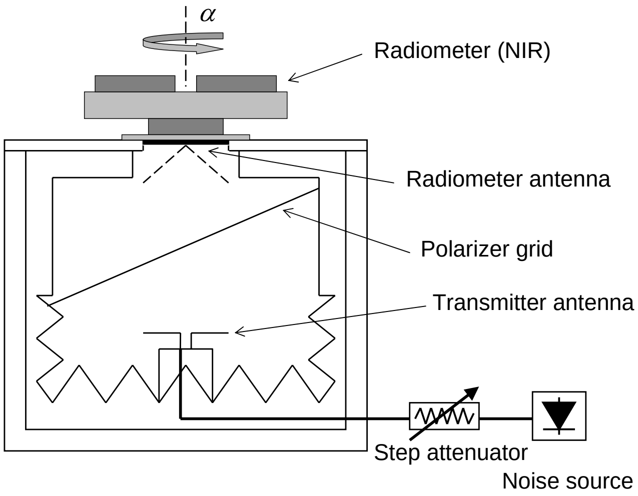

Figure 4-19. Measurement setup utilizing the linearly polarized antenna target.

The absorber load is made out of a metal box with electrically shielded cover and absorber material covering the inside walls. The cover has a hole for the antenna of the radiometer. Figure 4-19 shows a schematic diagram of the load. The return loss of the absorber is specified to be over 25 dB all around the walls of the box.

The transmitter antenna is a linearly polarized microstrip patch antenna with a cross-polarization ration of about 25 dB. It is connected to a noise source through a step attenuator, which can be adjusted in the range of 0-30 dB with one-decibel steps. The noise temperature of the transmitted field is adjusted so that the radiometer sees about 375 K in total (so that when the transmitted field is in the direction of either polarization, this polarization sees about 375 K).

The polarizer grid is a grid made out of metal wire with diameter of 3.0 mm and spacing of 9.4 mm. The total size of the grid is 540 mm by 630 mm. The attenuation of the grid at 1.4 GHz is 0.2 dB, when the electric field is perpendicular to the grid and 32.5 dB when the electric field is parallel to the grid. The grid was designed based on the theory presented in [158] and [159], which gives, among others, the spacing of the grid and the thickness of the wires.

Results

Figure 4-20 shows the obtained nominal correlations at angles α equal to -45°±5°, 0°±5°, +45°±5° and +90°±5°. The results are clearly located on a straight line. At 0° and +90° angles the effect of 5° step is large but at -45° and +45° angles it is very small as expected. There are also deviations from the line, especially at 0° and -5°, which is most probably due to the pointing inaccuracy of the radiometer, which was in order of a couple of degrees.

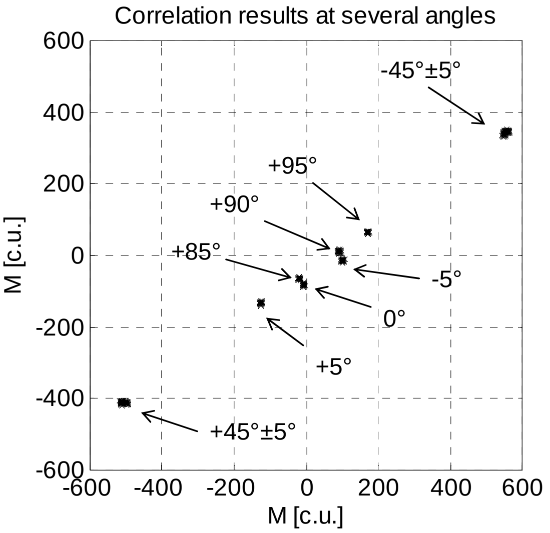

Figure 4-20. Correlation results at rotation angles -45°±5°, 0°±5°, +45°±5° and +90°±5° for nominal correlations (1 c.u. = 10^{-4}). As expected, at ±45° angles the effect of 5° steps is much smaller than in the cases of 0° and 90° angles, which makes the method more robust.

Figure 4-21 shows the correlations at -45° and +45° angle, the offset based on these calculated using Equation (4-5) and the corrected line without the offset. The angle, i.e. phase imbalance, is calculated using Equation (4-4). Table 4-7 lists the resulted phase imbalances and offset for nominal and redundant correlations.

The uncertainty of the offset is calculated according to the analysis presented in [P1], which gives for an uncertainty of 0.17 K for the third and fourth Stokes parameter; this is considered acceptable.

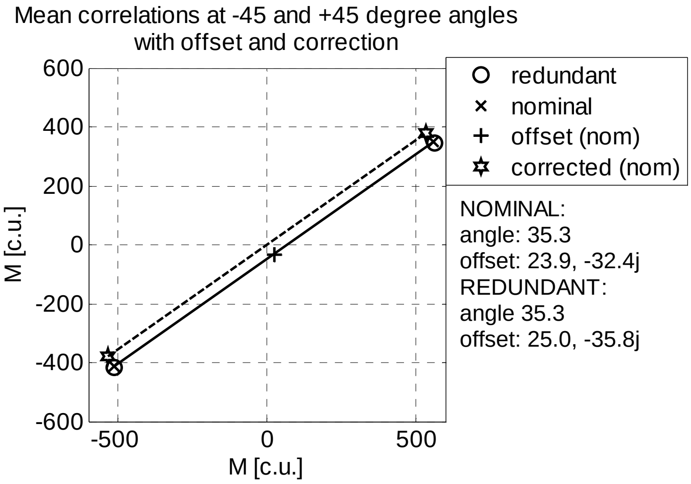

Figure 4-21. Mean correlations at -45° and +45° angles with offset and corrected values (for nominal correlations).

Table 4-7. Phase imbalance of the NIR and the offset of the measurement.

	Phase imbalance [deg]	**Offset [cu]**
Nominal	35.30	23.2-j32.4
Redundant	35.26	25.3-j35.8

The measurements were also made without the polarizer grid at rotation angles -45°, 0°, +45°, +90°. The offset was observed to be clearly lower than in the measurement with the polarizer grid and the measured phase imbalance is in good agreement with the result obtained with the polarizer grid. The lower offset may be due to the fact that the polarization impurity has opposite phase as compared to the non-idealities of the antenna of the radiometer. The cross-polarization ratio of the transmitting antenna is about 25 dB, which, based on this result, seems to be enough for the application of this technique.

4.4 Contribution of the work to the polarimetric and interferometric radiometer technology and calibration

A new spaceborne polarimetric radiometer and its prototype have been developed for the reference of a interferometric synthetic aperture radiometer [P1],[P2],[P3]. The radiometer uses the noise injection technique for the measurement of the 1st and 2nd Stokes parameters, and digital correlation to retrieve the 3rd and 4th Stokes parameter. The polarimetric measurement capability has been demonstrated in the presence of the noise injection measurement. Furthermore, as the radiometer is to measure the two levels of the internal noise distribution network, a method for this measurement and its accurate calibration was developed. These techniques can be applied in the development of any polarimetric or interferometric radiometers, to increase their accuracy, flexibility and applicability.

Due to the wide antenna lobe, the reference radiometer has only one precisely known calibration target in the orbit; hence, the calibration is planned so that the measurement precision meets the requirement using only one target. The critical part of this is accurate measurement of the loss of the front-end and antenna of the radiometer. A method was demonstrated, in which the loss is determined with great precision taking the non-idealities, i.e. mismatching, into account as well. These techniques contribute to the available calibration methods of conventional and polarimetric radiometers.

Finally, the end-to-end phase imbalance was to be measured, in order to solve the phase imbalance of the antenna and front-end. The developed method includes a measurement of a linearly polarized correlated source in two different angles with respect to the polarizations of the radiometer yielding the phase imbalance [P4]. The method opens the possibility for measurement of the end-to-end phase imbalance with simple calibration target; something that was not available before.

5 REMOTE SENSING OF SEA SURFACE WITH POLARIMETRIC RADIOMETER

As the previous Chapter was focused on the development and calibration of the instrumentation for polarimetric radiometry, this Chapter concentrates on the development of polarimetric radiometry applications. Typically applications are developed using measurement data and by examining theoretical models. Therefore, the first part of this Chapter presents a study investigating the incidence angle dependency of airborne wind vector measurements carried out using a polarimetric radiometer. The second part introduces a method for simulation of ocean surface scattering and, by definition, also the emission i.e. brightness temperature, as is given in Equations (2-13) and (2-15). The focus in the second part is on the development of the actual numerical methodology for this purpose, and the application of this method is beyond the scope of this work. The third and final part of this Chapter discusses the contribution of this work to the field of passive sea surface remote sensing.

5.1 Incidence angle dependency in wind speed measurement

In this Section the incidence angle dependency of the wind vector retrieval is studied. First the theoretical approach for the study is presented; then the instrument and the measurement campaigns are described, and finally, the results are presented and discussed.

5.1.1 Theoretical approach

The principles to retrieve the target brightness temperature, i.e., the brightness temperature of sea surface, are described in the following. The attitude data of the aircraft were applied to compensate for the mixing of the measured first three Stokes parameters due to aircraft roll (banking). The fourth Stokes parameter was not compensated for since it is the measure of the circularly polarized radiation and thus independent of the polarization basis.

Atmospheric effects

When correcting for the atmospheric effects, a radiative transfer model was applied for the orthogonal polarizations. The model includes the following components; upwelling atmospheric brightness temperature (T_{UP}), atmospheric attenuation (τ), downwelling atmospheric brightness temperature (T_{DN}), and the reflection coefficient of the sea surface as a function of the relative wind direction and incidence angle, $r(\phi,\theta)$, Equation (2-13). Scattering effects were assumed to be negligible and they were ignored. Note that the atmospheric emission and attenuation are independent of the wind speed and relative wind direction. The applied radiative transfer model (for example [51]), accounting for the azimuth dependency of the emissivity due to wind, can be written as:

$$T_M(\phi,\theta) = T_{UP} + \tau\,\varepsilon(\phi,\theta)T_S + \tau\,T_{DN}\left[1-\varepsilon(\phi,\theta)\right], \tag{5-1}$$

where $T_M(\phi,\theta)$ is the measured brightness temperature after compensating for the aircraft roll, and T_S is the physical temperature of the sea surface. Using the definition of emissivity, Equations (2-13) and (5-1) yield

$$T_B(\phi,\theta) = \frac{T_M(\phi,\theta) - \tau\,T_{DN} - T_{UP}}{\tau\left(T_S - T_{DN}\right)}T_S, \tag{5-2}$$

where $T_B(\phi, \theta)$ is the brightness temperature of the sea surface as a function of the relative wind direction and incidence angle.

In estimating the contribution of atmospheric radiation and attenuation, the principles presented in [3] were followed. According to these principles, the attenuation of the atmosphere can be determined using the pressure and kinetic temperature profiles. Pressure profile was estimated using the measured sea level pressure and assuming exponential behavior. Kinetic temperature profile was estimated using the measured surface air temperature and a statistical model. In retrieving the third and fourth Stokes parameter of the sea surface, only atmospheric attenuation was compensated for. This simplification is justified because atmospheric emissions are essentially unpolarized. The Stokes parameters of the sea surface were retrieved with the above processing steps. Finally, the signal variations manifested by incidence angle fluctuations (due to aircraft motion) were compensated for T_v and T_h, using the emissivity model presented in [162], and for T_3 using the model presented later in Table 5-4.

Wind speed model and sensitivity

The coefficients of the harmonics model in Equations (2-35)-(2-38) were retrieved from the measured data sets. Note that since no clear harmonic modulation was found for the fourth Stokes parameter as a function of wind direction, the fourth Stokes parameter is not considered in this study.

After solving the Fourier coefficients for each dataset, the coefficients were examined as a function of the incidence angle. A clear dependence for most of the coefficients can be found at each wind speed value. This dependence shows very linear behavior within the measurement range (43°-58°); therefore, a linear model was fitted to these data.

Similarly, the harmonic coefficients show a linear behavior as a function of wind speed in the 6.7 to 12.0 m/s range, when the incidence angle is kept constant. However, the slope of the coefficients w.r.t. wind speed (i.e. the sensitivity of the harmonic coefficients on wind speed) is not constant as a function of the incidence angle. These sensitivities (slopes) can be plotted as a function of incidence angle. The sensitivity is defined here as the absolute value of the slope. Because the incidence angles were never exactly the same during the measurements at different wind speeds, the incidence angles applied for this analysis were interpolated/extrapolated equal using the linear model described earlier (between Fourier coefficients and incidence angle).

Furthermore, an empirical model, as a function of the harmonic coefficients and the incidence angle, for wind speed retrieval is developed using the sensitivity (with the sign). For example, [65] and [126] presented model functions for wind speed, and [69] introduced a theoretical model for incidence angle. Based on these models, and our results, it is reasonable to assume a linear behavior in the wind speed and incidence angle range of this study. Although, semi-empirical [126] and theoretical [69] models have also been presented previously, the choice of a purely empirical model (also used previously [56]) is justified by the fact that geophysical models of windy sea surface have remained uncertain [163]. The model is formulated as follows:

$$WS(C,\theta)=(a_C\theta+b_C)C+c_C\theta+d_C, \tag{5-3}$$

where WS is the value of wind speed, C is the harmonic coefficient, θ is the incidence angle, a_C and b_C are the slope and offset of the sensitivity (with the sign) of the harmonic coefficient C and c_C and d_C are the coefficients of the offset of the sensitivity (with the sign) of the harmonic C.

In previous studies ([56],[65],[66]) sophisticated nonlinear models have been presented for the dependency of the harmonics on the wind speed over a wide range of incidence angles and/or wind speeds. As stated in the previous paragraph, for the incidence angle and the wind speed range analyzed in the current study, however, the linear model presents a simple and accurate way to describe the incidence angle dependency and, especially, the sensitivity of the coefficients to the wind speed.

5.1.2 Measurement campaigns

This Subsection describes first the platform, instrumentation and calibration method used in the measurement campaigns, and then the details of the measurement site, geometry and conditions.

Instrument description

TKK's airborne Fully Polarimetric Radiometer (FPoR) was used for this study. The radiometer operates at 36.5 GHz and it uses direct cross-correlation technique with analog correlators for solving all four Stokes parameters simultaneously. It has a radiometric resolution of about 0.2 K for the orthogonal polarizations and 0.3 K for the third and fourth Stokes parameters with an integration time of 1 second. The absolute accuracy is estimated to be 0.5 K. A detailed description of the radiometer can be found in [58].

The FPoR is integrated into the profiling subsystem of the HUTRAD radiometer system, which consists of several major assemblies including six other radiometers in the 1.4 - 94 GHz range [36],[160].

The calibration of FPoR is presented in detail in [122]. In general terms, a fully polarimetric calibration target is applied to generate linearly independent sets of precisely known Stokes parameters. The target consists of cold and hot absorber loads, a polarizer grid, a retardation plate, and a pedestal with rotary mechanism. The cold load is implemented using an absorber cooled down with liquid nitrogen.

Measurement flights

Data were collected in five measurement flights during 2002-2004. The flight dates are presented in Table 5-1. Each experiment consisted of a set of circles flown over the Kalbådagrund area on the Gulf of Finland, the Baltic Sea. Between each set of circles, the incidence angle of the antenna beam was altered by changing the roll and pitch angles of the aircraft; the obtained incidence angles ranged from 43° to 58°. Altogether, 29 datasets were collected during five experiment flights; each dataset contains data with a relatively constant incidence angle and wind speed.

Figure 5-1 illustrates the measurement geometry. The antenna footprint on the surface ranged from about 100 by 130 meters to about 130 by 250 meters. The attitude and speed of the aircraft were measured using two redundant systems; an attitude GPS navigation system and an inertial navigation system.

Table 5-1.The flight dates, wind speeds, surface temperatures and cloud conditions

Flight No.	**Date**	**WS** [*m/s*]	T_S [°*C*]	**Clouds**
1	27 Mar 2002	6.7	+1.9	clear
2	28 Mar 2002	8.6	+1.9	clear
3	5 Dec 2003	12.0	+3.1	cloudy
4	7 Apr 2004	8.1	+1.2	clear
5	22 Apr 2004	10.9	+1.0	partial

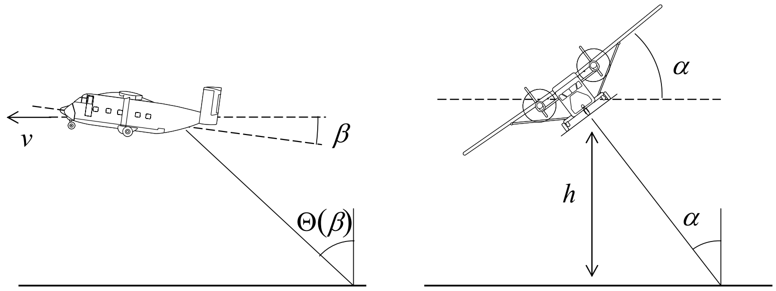

Figure 5-1. The measurement geometry. The incidence angle was varied by changing the roll, α, and pitch, β, angle of the aircraft during the circular flights: α was varied about 40° and β about 4° (nominal value of Θ being 43°). The ground speed, v, was about 55 m/s (varying between 50-60 m/s) and the flight height, h, was about 1000 m.

The ground truth data were collected by the Kalbådagrund weather station, which is an open sea station, located about 30 km off the coast in the measurement area. The collected ground truth parameters include wind speed, wind direction, air temperature and air pressure. The wind speed in the experiments ranged from 6.7 m/s to 12.0 m/s. The measured wind speed values (scaled to 10 m height above sea level [161]) during the experiments are depicted in Table 5-1. The weather station measured wind speed and direction only once in an hour, which generated some uncertainty. Therefore, the measured T_3 data were used to determine the wind direction for individual datasets. It is noted that when coincided in time, the measured wind direction was always within few degrees from that determined using T_3 data. The only exception was flight number 1; due to low wind speed, the T_3 signal was weak and determination of wind direction inaccurate. For flight number 1 in situ measurement data were used for wind direction.

The physical temperatures of the sea water and sea surface salinity were estimated from measurements performed by the Finnish Institute of Marine Research.

5.1.3 Experimental results

This Subsection presents the obtained experimental results. They are analyzed with respect to the incidence angle dependency, wind speed sensitivity and wind speed retrieval.

Table 5-2 shows all 29 obtained datasets of harmonic coefficients with wind speed values and incidence angles. In general, the measured brightness temperatures show relatively little deviation from curves given by Equations (2-35) through (2-37) with the coefficients of Table 5-2. However, during measurements flights 3 and 5 the sky was at least partially covered with clouds, which degraded the data a little bit by increasing the deviation of the data points from the fitted curve. This can be seen in Table 5-3, where the averaged standard deviations (with respect to the fitted curve) of the measurements for each of the first three Stokes parameters are listed. Note that the standard deviation includes both instrumental and geophysical noise.

Table 5-2. The datasets of the harmonic coefficients and respective wind speeds and incidence angles.

Data No.	**WS** [*m/s*]	θ [*deg*]	T_{v1} [K]	T_{v2} [K]	T_{h1} [K]	T_{h2} [K]	T_{31} [K]	T_{32} [K]
1	6.7	43.8	0.04	0.10	0.00	-0.11	-0.06	-0.19
2	6.7	46.4	0.12	0.02	0.07	-0.12	-0.01	-0.14
3	6.7	46.8	0.11	0.12	0.08	-0.01	-0.05	-0.16
4	6.7	47.6	0.05	0.13	0.05	-0.15	-0.03	-0.15
5	6.7	48.8	0.14	0.12	0.07	0.03	-0.07	-0.14
6	6.7	52.1	0.07	0.02	0.04	-0.04	-0.08	-0.02
7	6.7	52.2	-0.02	0.03	0.06	0.04	-0.09	-0.01
8	8.1	47.5	0.48	0.12	0.24	-0.71	-0.53	-0.66
9	8.1	51.4	0.63	-0.07	-0.12	-0.75	-0.68	-0.54
10	8.1	51.9	0.68	-0.02	0.33	-0.62	-0.72	-0.40
11	8.1	55.4	0.62	-0.23	0.15	-0.60	-0.61	-0.25
12	8.6	43.6	0.42	0.20	0.05	-0.73	-0.41	-0.71
13	8.6	46.0	0.49	0.16	0.13	-0.64	-0.40	-0.60
14	8.6	46.2	0.38	0.11	0.15	-0.52	-0.40	-0.52
15	8.6	47.3	0.4	0.10	0.18	-0.46	-0.41	-0.46
16	8.6	51.7	0.48	0.01	0.32	-0.67	-0.49	-0.38
17	8.6	51.8	0.54	-0.09	0.44	-0.62	-0.47	-0.38
18	8.6	52.3	0.45	-0.04	0.37	-0.41	-0.54	-0.20
19	10.9	45.4	0.78	0.26	0.02	-1.18	-0.86	-1.09
20	10.9	48.5	0.58	0.10	-0.28	-1.08	-0.86	-0.88
21	10.9	52.0	0.9	-0.05	0.55	-0.89	-0.82	-0.74
22	10.9	52.3	0.66	-0.03	0.24	-0.73	-0.75	-0.54
23	10.9	57.8	0.76	-0.35	0.21	-0.68	-0.59	-0.21
24	12	45.0	1.12	-0.11	0.02	-2.12	-1.26	-1.51
25	12	45.7	0.75	0.47	-0.48	-0.85	-1.07	-1.12
26	12	47.2	0.58	0.28	-1.04	-0.99	-1.24	-1.3
27	12	50.6	1.36	-0.07	0.17	-1.13	-1.05	-1.08
28	12	51.0	1.54	0.46	0.45	-0.26	-1.12	-0.93
29	12	54.9	0.85	-0.06	-0.75	-0.95	-1.14	-0.70

Table 5-3. The standard deviations of the measurement data with respect to the fitted curve.

Flight No.	**WS** [*m/s*]	**Clouds**	T_v [K]	T_h [K]	T_3 [K]
1	6.7	clear	0.170	0.227	0.192
2	8.6	clear	0.157	0.269	0.190
3	12.0	cloudy	0.712	1.424	0.346
4	8.1	clear	0.207	0.333	0.222
5	10.9	partial	0.225	0.419	0.310

Dependency on incidence angle

Figure 5-2 shows the harmonic Fourier coefficients of the first, second and third Stokes parameter as a function of the incidence angle at three different wind speed values (namely 6.7, 8.6 and 10.9 m/s). The linear fits are illustrated with lines. The data collected at the two other wind speeds (8.1 and 12.0 m/s) show similar behavior; they are left out in order to improve the clarity of the illustration. Also, the data collected from the 3rd flight (wind speed 12.0 m/s) suffered from the cloudy conditions and especially first and second Stokes parameters were affected (see Table 5-3). Table 5-4 lists the slopes (vs. incidence angle) for all five experiments.

Yueh et al. presented in [65] a model for the harmonic coefficients as a function of the wind speed at three different incidence angles (45°, 55°, and 65°). This model was improved in [66] using, for example, new WindSat satellite data. The coefficients of [66] are plotted in Figure 5-2 at these incidence angles and respective wind speeds. For many harmonics, the resulted plots are similar to those obtained in this study. Especially, T_{v2}, T_{h1} and T_{32} show similar behavior. However, there are also differences, for example, in T_{v1}.

The results indicate that the harmonics of the third Stokes parameter have clear dependency on the incidence angle (Figure 5-2, Table 5-4). However, as shown in Table 5-4, the sign of the dependency for flight numbers 3 and 5 (wind speeds 12.0 and 10.9 m/s) is different from numbers 1, 2 and 4 (wind speeds 6.7, 8.6 and 8.1 m/s), which show similar behavior as the model and measurements presented in [69]. Note, that the flight numbers 3 and 5 were the ones contaminated by the clouds, which could explain the unexpected behavior. On the other hand, T_3 is in general relatively undisturbed by clouds.

The potential sources for the harmonics' differences include differences of viscosity of sea water; in the measurements conducted for this study, the water had a temperature of +2°C on average and a salinity of approximately 5 psu. Both these values are believed to be lower than the average conditions in [66]. Also, different atmospheric conditions can cause some differences, as suggested in [127]. Furthermore, the second order processing differences between this study and [66] may have caused some differences in the results; for example, we have taken advantage of mathematical methods and statistical estimates to assess atmospheric contribution, whereas [66] relied on radiometric measurement data.

The obtained dependency slopes, presented in Table 5-4, can be used for the correction of the incidence angle deviations, for example, due to aircraft motion during measurement.

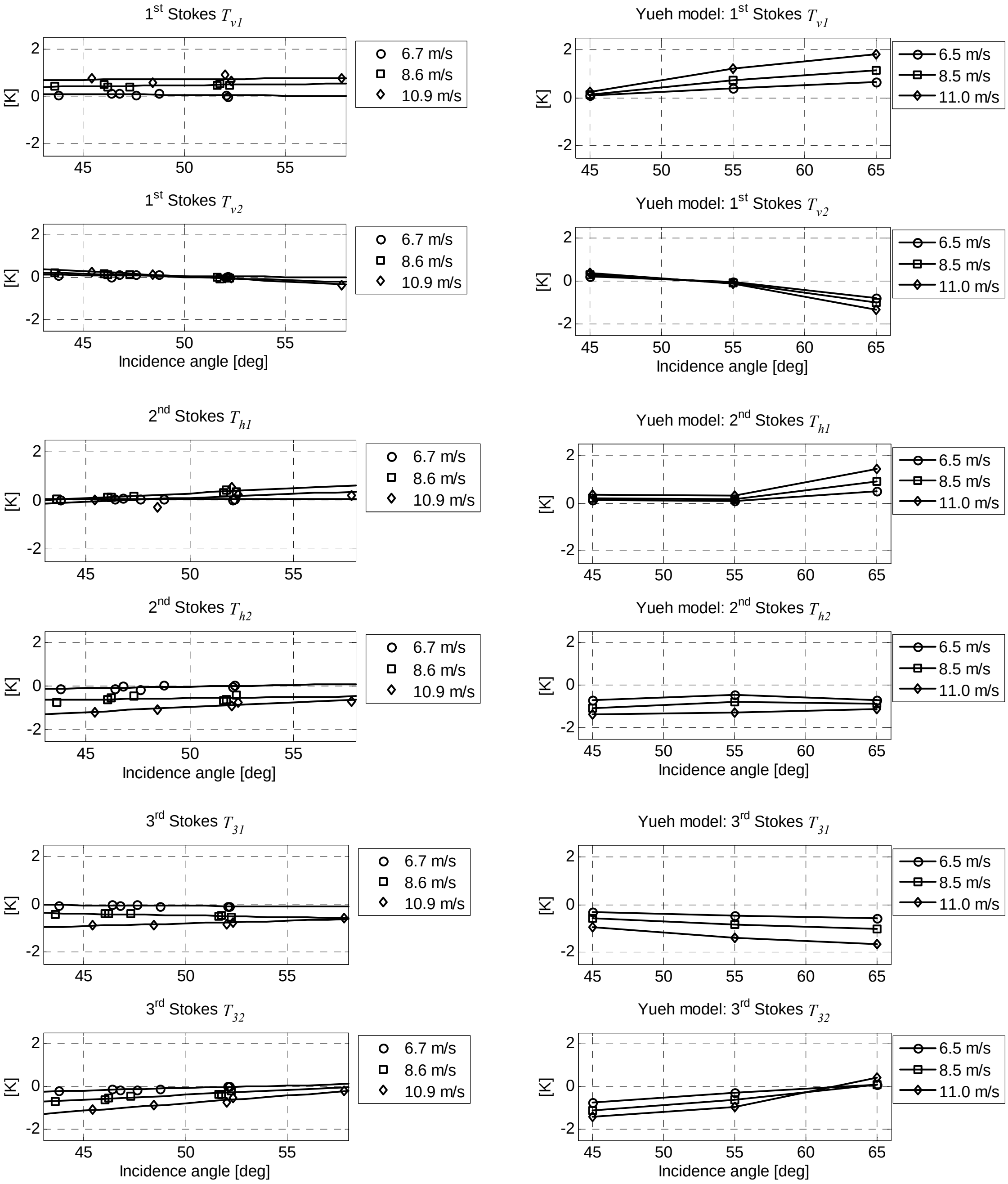

Figure 5-2. The Fourier coefficients of the first, second and third Stokes parameter as a function of the incidence angle. Left: our experimental data. Right: the values from the Yueh model [66]. In the plots of our experimental data, the lines show the linear fit to the data set at each wind speed.

Table 5-4. The slopes of the harmonic coefficients vs.incidence angle with the wind speed

WS [*m/s*]	T_{v1} [*K*/°]	T_{v2} [*K*/°]	T_{h1} [*K*/°]	T_{h2} [*K*/°]	T_{31} [*K*/°]	T_{32} [*K*/°]
6.7	-0.006	-0.009	0.002	0.015	-0.005	0.023
8.1	0.019	-0.043	-0.008	0.014	-0.011	0.053
8.6	0.009	-0.030	0.040	0.011	-0.014	0.045
10.9	0.005	-0.049	0.032	0.043	0.023	0.071
12.0	0.026	-0.017	0.004	0.078	0.008	0.067

Sensitivity to wind speed

The obtained harmonics are dependent on the wind speed. As an example, the harmonic coefficients of the third Stokes parameter are presented in Figure 5-3 as a function of wind speed. The linear fits are illustrated with dashed lines.

The harmonics are shown for incidence angles of 43° and 58°; the slopes are dependent on the incidence angles. The absolute value of the slope with respect to the wind speed, or the sensitivity of the harmonic coefficients to the wind speed, is shown in Figure 5-4 for the T_v, T_h and T_3 parameters, respectively, as a function of incidence angle.

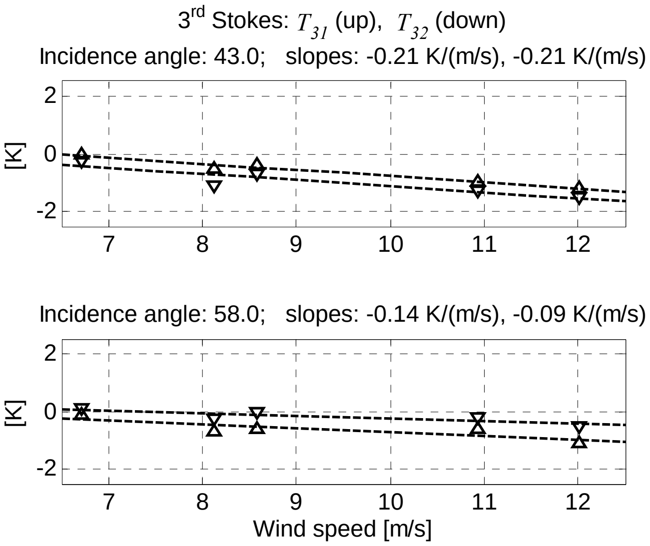

Figure 5-3. The third Stokes parameter as a function of wind speed. The upper figure shows the first and second harmonic coefficient for an incidence angle of 43 ° and the lower figure shows the first and the second harmonic coefficient for an incidence angle of 58 °.

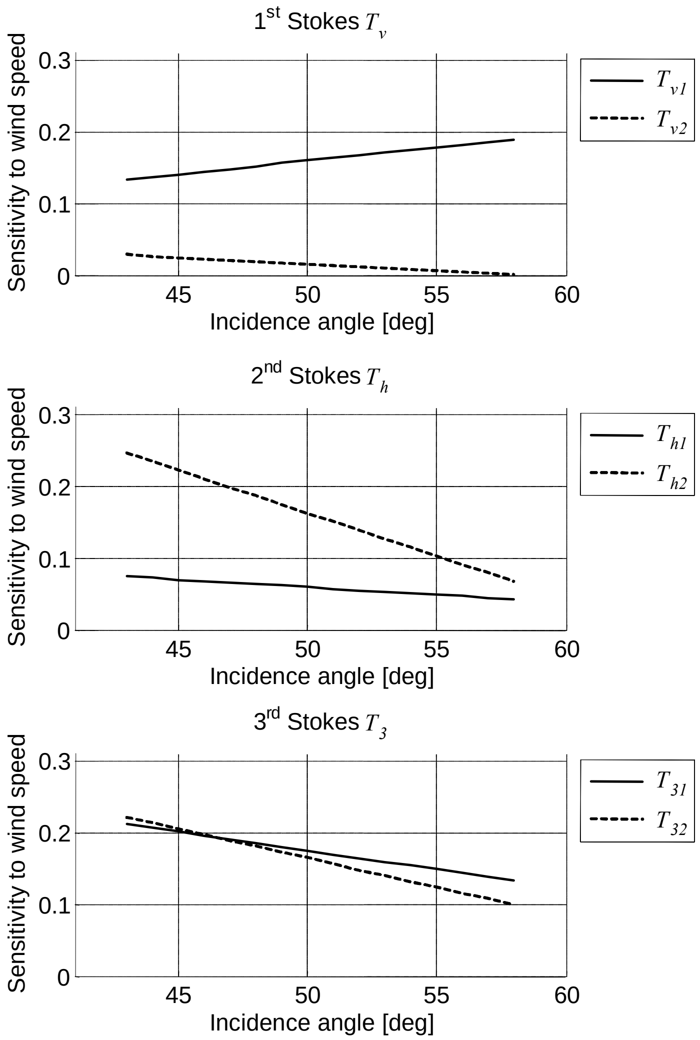

Figure 5-4. The sensitivities ($ms^{-1}K^{-1}$) of the first and second harmonic coefficients of the first three Stokes parameter to the wind speed as a function of incidence angle.

The sensitivity of all coefficients has a clear dependence on the incidence angle. In most cases the sensitivity increases with decreasing incidence angle, except in the case of T_{v1}. In the measurement range, the sensitivities of the harmonics on the wind speed have the following characteristic linear functions on incidence angle:

$$\Delta T_{v1}(\theta) = 0.0036\theta - 0.0221, \tag{5-4}$$

$$\Delta T_{v2}(\theta) = -0.0019\theta + 0.1095, \tag{5-5}$$

$$\Delta T_{h1}(\theta) = -0.0021\theta + 0.1634, \tag{5-6}$$

$$\Delta T_{h2}(\theta) = -0.0012\theta + 0.7611, \tag{5-7}$$

$$\Delta T_{31}(\theta) = -0.0052\theta + 0.4357, \tag{5-8}$$

$$\Delta T_{32}(\theta) = -0.0082\theta + 0.5732, \tag{5-9}$$

where $\theta = 43°$ to $58°$.

Wind speed model

The data set was used to develop a model for wind speed retrieval based on Equation (5-3). The harmonic coefficients of the third Stokes parameter are obviously best suited for this purpose due to their insensitivity to the clouds (see Table 5-3) and stronger dependency on the wind speed over the incidence angle range (especially the first harmonic coefficient). T_{v2} and T_{h1} are poorly suited for the use in the model due to the fact that they are very insensitive to the wind speed (see Figure 5-2).

Table 5-5 shows the coefficients of Equation (5-3) for T_{v1}, T_{h2}, T_{31} and T_{32}. T_{v2} and T_{h1} did not produce useful values due to the aforementioned reasons. Table 5-6 shows the averaged result of the model applied to all data sets and root mean square of the deviation from the ground truth. The first harmonic coefficient of the third Stokes parameter produces the best result having most of the RMS values under 1 m/s, which would indicate that this harmonic is the most accurate for wind speed retrieval over the given incidence angle range. This preliminary model can be used for the wind speed retrieval (using measurements in multiple azimuth angles) up to this accuracy. The model for T_{31} reads ($\theta = 43°$ to $58°$):

$$WS(T_{31},\theta) = (-0.19\theta + 3.3)C + 0.12\theta + 11.31. \qquad (5\text{-}10)$$

The model is to be expanded to a wider wind speed and incidence angle range as more measurement flights will be carried out. In the development process, the results given by this model can be compared to other models of other studies in order to find an optimum model.

Table 5-5. The coefficients for the wind speed model, Equation (5-3).

Harmonic	a_C	b_C	c_C	d_C
T_{v1}	-0.153	14.076	0.025	4.382
T_{h2}	-0.931	36.054	-0.254	16.763
T_{31}	-0.187	3.296	-0.115	11.310
T_{32}	-0.401	12.745	0.167	-2.100

Table 5-6. Result of the wind speed model, Equation (5-3), using the values of Table 5-5 for different harmonic coefficients, C.

Ground truth [m/s]	$C=T_{v1}$		$C=T_{h2}$		$C=T_{31}$		$C=T_{32}$	
	mean	**rms**	**mean**	**rms**	**mean**	**rms**	**mean**	**rms**
6.7	6.1	0.7	4.9	2.1	6.1	0.7	6.7	0.3
8.1	9.4	1.3	11.6	3.6	9.4	1.3	10.0	1.9
8.6	8.6	0.3	9.6	1.5	8.3	0.3	8.9	0.6
10.9	10.2	1.0	13.7	2.9	10.2	1.0	11.4	1.0
12.0	12.4	2.2	13.6	4.2	12.3	0.6	13.5	1.7

5.2 Numerical simulation of rough surface scattering

In this Section a method for efficient calculation of electromagnetic scattering from rough dielectric surface, like ocean surface, is presented. In relation to the previous part of this Chapter, this method can be used to simulate the emission from ocean surface for e.g. development of wind vector retrieval. Equations (2-13) and (2-15) give the relation between the scattering coefficients and emission. This Section focuses on presentation of the methodology of this numerical method allowing its application to the case of wind vector retrieval or other radiometer measurements in further work.

Figure 5-5 illustrates a three-dimensional (3-D) scattering problem from a two-dimensional (2-D) rough dielectric surface. The dielectric medium in region 1, which is above the interface (permittivity ε_1, permeability μ_1), and region 2, which is under (ε_2, μ_2) the interface, is assumed to be homogeneous.

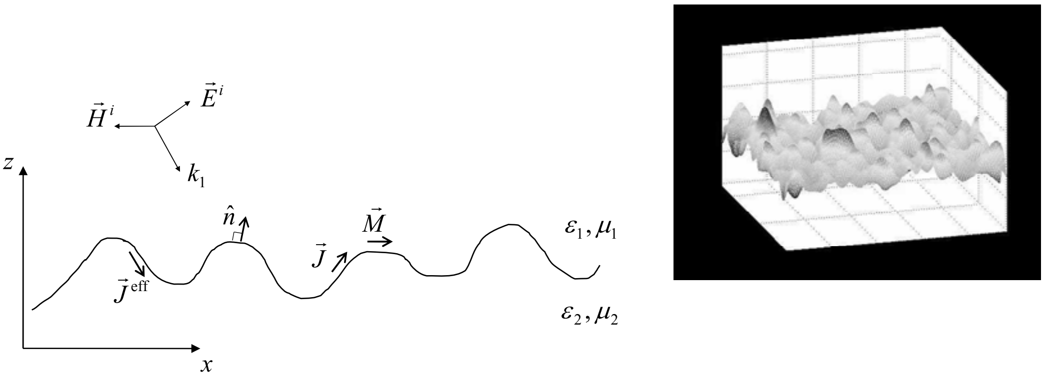

Figure 5-5. A schematic diagram of a 3-D scattering problem from a 2-D random rough surface.

In the following Sections the problem is first formulated and discretized, then FFT is applied using AIM (Adaptive Integral Method) to speed up the calculation, and finally, simulation results from sample surfaces with different roughness and size are presented.

5.2.1 Formulation and discretization

First the scattering problem is formulated using the Single Magnetic Field Integral Equation (SMFIE) [73] and discretized for the numerical calculation.

5.2.1.1 Single Integral Equation Formulation

A scattering problem can be formulated so that the total field in region 1, after the scattering, is composed of the incident and scattered fields, as follows:

$$\vec{E}_1(\vec{r}) = \vec{E}_1^{inc}(\vec{r}) - \vec{E}_1^{scat}(\vec{r}), \tag{5-11}$$

$$\vec{H}_1(\vec{r}) = \vec{H}_1^{inc}(\vec{r}) - \vec{H}_1^{scat}(\vec{r}), \tag{5-12}$$

Using Equation (2-5), this can be written as:

$$\vec{E}_1(\vec{r}) = \vec{E}_1^{inc}(\vec{r}) - \frac{1}{i\omega\varepsilon_1}\mathbf{D}_1(\vec{J})(\vec{r}) - \mathbf{K}_1(\vec{M})(\vec{r}), \tag{5-13}$$

$$\vec{H}_1(\vec{r}) = \vec{H}_1^{inc}(\vec{r}) - \frac{1}{i\omega\mu_1}\mathbf{D}_1(\vec{M})(\vec{r}) + \mathbf{K}_1(\vec{J})(\vec{r}), \tag{5-14}$$

Taking the cross product of Equation (5-14) with the unit normal vector on the surface, gives the magnetic field integral equation (MFIE):

$$-\frac{1}{i\omega\mu_1}\hat{n}\times\mathbf{D}_1(\vec{M}) + \hat{n}\times\mathbf{K}_1(\vec{J}) - \frac{1}{2}\vec{J} = -\hat{n}\times\vec{H}_1^{inc}, \tag{5-15}$$

Inside the object the fields are expressed in terms of efficient electric current, $\vec{J}^{eff}$, as

$$\vec{E}_2(\vec{r}) = -\frac{1}{i\omega\varepsilon_2}\mathbf{D}_2(\vec{J}^{eff})(\vec{r}), \tag{5-16}$$

$$\vec{H}_2(\vec{r}) = \mathbf{K}_2(\vec{J}^{eff})(\vec{r}), \tag{5-17}$$

The boundary conditions at the interface between the two media

$$\hat{n}\times\vec{E}_1 = \hat{n}\times\vec{E}_2, \tag{5-18}$$

$$\hat{n}\times\vec{H}_1 = \hat{n}\times\vec{H}_2, \tag{5-19}$$

give a relation between the currents $\vec{J}$, $\vec{M}$ and $\vec{J}^{eff}$ [73]

$$\vec{M} = \frac{1}{i\omega\varepsilon_2}\hat{n}\times\mathbf{D}_2(\vec{J}^{eff}), \tag{5-20}$$

$$\vec{J} = \hat{n}\times\mathbf{K}_2(\vec{J}^{eff}) - \frac{1}{2}\vec{J}^{eff}, \tag{5-21}$$

on the surface *S*. Substituting Equations (5-20) and (5-21) into Equation (5-15) gives SMFIE for $\vec{J}^{eff}$:

$$\hat{n}\times\vec{H}_1^{inc} = \left[\frac{1}{i\omega\mu_1}\frac{1}{i\omega\varepsilon_2}\hat{n}\times\mathbf{D}_1(n\times\mathbf{D}_2) - \left(\hat{n}\times\mathbf{K}_1 - \frac{1}{2}I\right)\left(\hat{n}\times\mathbf{K}_2 - \frac{1}{2}I\right)\right]\vec{J}^{eff}, \tag{5-22}$$

where *I* is the identity operator.

Note that SMFIE provides unambigious solution only outside the resonant frequency of the object and for conducting ojects. These requirements are met in the application of this study, which is ocean surface.

5.2.1.2 Discretization by the Method of Moments

Direct discretization of Equation (5-22) including products of integral operators with MoM (Method of Moments) is very ineffective, and therefore the discretization is done in two steps using technique similar to [73].

Formulation of system matrix

In order to model the surface geometry accurately, the triangular RWG (Rao-Wilton-Glisson) basis functions are used for expanding the currents [75]:

$$\vec{f}_j(\vec{r}\,')=\begin{cases}\dfrac{L_j}{2A_j^+}\left(\vec{r}\,'-\vec{p}_j^{\,+}\right), & \vec{r}\,'\in T_j^+,\\ \dfrac{L_j}{2A_j^-}\left(\vec{r}\,'-\vec{p}_j^{\,-}\right), & \vec{r}\,'\in T_j^-\ ,\\ \quad 0,\text{otherwise,} & \end{cases} \tag{5-23}$$

where $A_j^\pm$ is the area of the triangle $T_j^\pm$ and $p_j^\pm$ is the vertex of $T_j^\pm$ opposite to the common edge. The equations are tested with the following edge functions:

$$\vec{J}^{eff}=\sum_{i=1}^{N} I_i^{eff}\vec{f}_i(\vec{r}\,'), \tag{5-24}$$

where N is the number of interior edges of the mesh and I_i^{eff} are the unknown current coefficients. Similar equation can be written to $\vec{J}$ and I_i^e , and to $\vec{M}$ and I_i^m, respectively.

As shown in Appendix A the above discretization yields for the SMFIE the following matrix form:

$$\left[\frac{1}{i\omega\mu_1}\frac{1}{i\omega\varepsilon_2}\overline{\overline{D}}_1\overline{\overline{D}}_2+\left(\overline{\overline{K}}_1-\frac{1}{2}\overline{\overline{I}}\right)\left(\overline{\overline{K}}_2-\frac{1}{2}\overline{\overline{I}}\right)\right]\overline{I}^{eff}=\overline{b}\ . \tag{5-25}$$

The matrices $\overline{\overline{K}}$ and $\overline{\overline{D}}$ are defined as

$$\begin{aligned}K_{1,ij}&=\frac{1}{L_i}\int_{l_i}\iint_{T_j}\left(\hat{l}_i\cdot\nabla G_1\times\vec{f}_j\right)ds\,dl-\frac{\Omega_i^-}{2\pi}\delta_{ij}\\ D_{1,ij}&=k_1^2V_{1,ij}+W_{1,ij}=\frac{1}{L_i}\int_{l_i}\iint_{T_j}\left[k_1^2\left(\hat{l}_i\cdot\vec{f}_j\right)G_1+\left(\hat{l}_i\cdot\nabla G_1\right)\left(\nabla_s'\cdot\vec{f}_j\right)\right]ds\,dl\end{aligned}\ . \tag{5-26}$$

where Ω_i^- is the interior angle between triangles at edge *i* and T_j is both T_j^+ and T_j^- related to the edge *j*. Note that in the case of the second medium the interior angle is replaced by the exterior angle Ω_i^+. The elements of the excitation vector $\overline{b}$ are:

$$b_i=\frac{1}{L_i}\int_{l_i}\hat{l}_i\cdot\hat{n}\times\vec{H}^{inc}dl\,, \tag{5-27}$$

which is the average current magnitude flowing across the *i*th edge.

It should be pointed out that generally a stable discretization of $\overline{\overline{D}}_1\overline{\overline{D}}_2$ requires application of special basis and testing functions [164]. In SMFIE this term is multiplied with $1/\omega^2$ and combined with $(\overline{\overline{K}}_1 - 1/2\overline{\overline{I}})(\overline{\overline{K}}_2 - 1/2\overline{\overline{I}})$ yielding accurate results with above discretization when the frequency is high enough.

Computation of far terms

The elements of the system matrices $\overline{\overline{K}}$ and $\overline{\overline{D}}$, in which the basis and testing function do not have common edges are called here as the far terms. Figure 5-6 shows the calculation situation for the far terms; basis function is a triangular RWG function and the testing function is an edge between two RWG triangles. The calculation is a straightforward process of applying standard numerical integration on the triangles and the line.

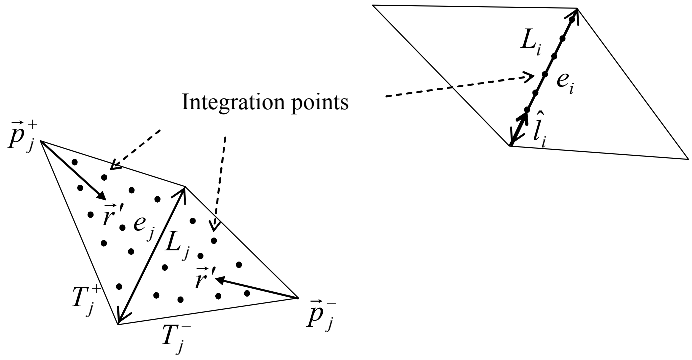

Figure 5-6. Triangular RWG function is used as the basis function and the common edge between triangles is used as the testing function. The numerical integration is performed over the surface of the triangles, in the case of the basis function, and along the edge, in the case of the testing function.

Computation of near terms

The elements of the system matrices $\overline{\overline{K}}$ and $\overline{\overline{D}}$, in which the basis and testing function has common edges are called here as the near terms. The obvious case for the near terms is when $i = j$, but there is also cases when an edge or vertex of a testing function is one of the edges or vertices of a basis function.

When $i = j$, the first term of $\overline{\overline{K}}$ vanishes and the elements are calculated simply by solving the angle between the triangles. However, elements of $\overline{\overline{V}}$ and $\overline{\overline{W}}$ withhold a singularity, which is solved, in the first case, using a transformation to the polar coordinates, and in the latter case, using Gauss divergence theorem.

The transformation to the polar coordinates is done so that the singularity is located in the origin dividing the RWG triangle into two sub-triangles. This eliminates the problem, since the singularity is of order $\sim 1/r$ [165].

For $\overline{\overline{W}}$, the Gauss divergence theorem can be applied to transform the surface integral to a boundary integral. The benefit of this treatment is the fact that the dot product of the outer normal of the edge withholding the singularity and the testing function yields zero. See Appendix A for a detailed explanation of the method. Note that e.g. in [73], [74] and [114] this term is not calculated with this kind of precision.

When $i \neq j$, but the edge of the testing function is one of the edges of the basis function these same methods are applied, including the elements of $\overline{\overline{K}}$, to which the Gauss divergence theorem is used (see Appendix A). And when $i \neq j$, but the vertices of the basis and the testing function are the same, the integration points are located so that the effect of the singularity is damped.

5.2.1.3 Application to rough surface scattering

The above treatment is made for a closed object. The simulation of surface scattering has the problem that the surface is very large and it is more practical to model it as an open surface than a closed object. Hence, the effect of the borders of the surface needs to be minimized. Figure 5-7 shows a calculation where scattering from a closed object (box of size $n\lambda \times n\lambda \times \lambda/10$, where λ is the free space wavelength) is compared to scattering from a plate (of size $n\lambda \times n\lambda$) in order to evaluate the effect of the truncation of the surface to a finite size. The surfaces are flat and the properties of the surfaces are the same as in the examples in Figure 5-9, Figure 5-10 and Figure 5-11. The results show that the truncation has no critical effect on the result. This is related to the relatively high conductivity of the surface, which attenuates the incident field toward the borders of the surface area. The high conductivity originates from the fact that the aim of the study is to simulate scattering from ocean surface.

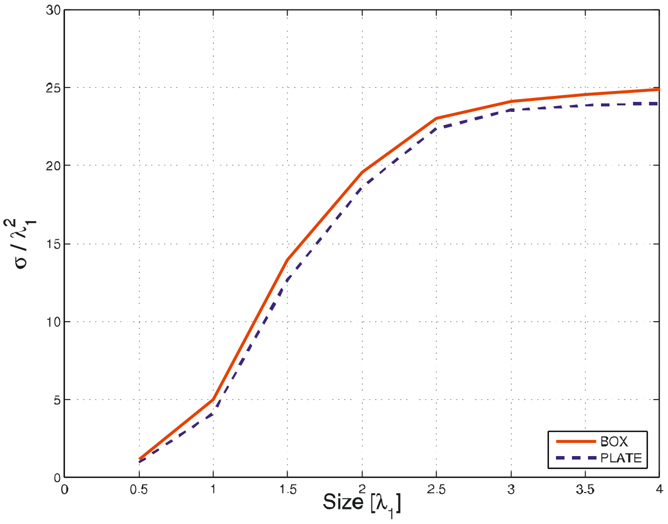

Figure 5-7. Backscattered RCS (in units of λ^2) of a dielectric box (box) with thickness $\lambda_1/10$ and of a thin box (plate) with zero thickness corresponding to a truncated surface. Horizontal axis gives the size of the box in terms of λ_1.

Furthermore, a common technique is applied in which an incident field with amplitude tapering toward the edges of the surface is used. In the simulations of this study the field presented in [71] has been used. The *x*-component of magnetic field is Gaussian tapered and the *y*-component is zero, i.e. [71]:

$$H_x^{inc} = -\frac{1}{\eta_0} e^{-\left(x^2+y^2\right)/g^2}, \qquad (5\text{-}28)$$

where g is the parameter that defines the tapering of the field amplitude on the surface. Furthermore, as the aim of the study is to simulate ocean surface scattering, the conductivity of the surface is relatively large, which attenuates the incident field toward the borders of the surface area.

5.2.2 Application of Adaptive Integral Method and Fast Fourier Transform

To decrease computational complicity of the method, FFT in 2D is applied. In order to solve a scattering problem using FFT the surface must be divided into a uniform grid, which is not the case when RWG basis functions are applied. However, the RWG basis functions can be translated to functions of a uniform grid using adaptive integral method (AIM) [76]. This approach utilizes the benefits of RWG basis functions [75] and speed of FFT.

The FFT is used to speed up the matrix-vector products of Equation (5-25). Two operators are defined in order to solve these products with FFT: $\mathcal{K}_{1/2}^{\mathcal{F}}$ and $\mathcal{D}_{1/2}^{\mathcal{F}}$, where $\mathcal{K}_{1/2}^{\mathcal{F}}\left(\overline{X}\right)$ and $\mathcal{D}_{1/2}^{\mathcal{F}}\left(\overline{X}\right)$ denote calculation of the matrix-vector products $\overline{\overline{K}}_{1/2}\overline{X}$ and $\overline{\overline{D}}_{1/2}\overline{X}$, respectively, with FFT.

$\mathcal{K}_{2}^{\mathcal{F}}\left(\overline{X}\right)$ is defined by the subsequent operations. First, the vector potential is computed with FFT:

$$\begin{aligned}
\overline{A}_{2x} &= \mathcal{F}^{-1}\left\{\mathcal{F}\{\overline{G}_2\}\cdot\mathcal{F}\left\{\overline{\overline{Q}}_x\overline{X}\right\}\right\},\\
\overline{A}_{2y} &= \mathcal{F}^{-1}\left\{\mathcal{F}\{\overline{G}_2\}\cdot\mathcal{F}\left\{\overline{\overline{Q}}_y\overline{X}\right\}\right\}, \qquad (5\text{-}29)\\
\overline{A}_{2z} &= \mathcal{F}^{-1}\left\{\mathcal{F}\{\overline{G}_2\}\cdot\mathcal{F}\left\{\overline{\overline{Q}}_z\overline{X}\right\}\right\},
\end{aligned}$$

where $\overline{G}_2$ is a $\Pi \times 1$ vector of Green's function of AIM grid of size $\Pi \times \Pi$, $\overline{\overline{Q}}_{x,y,z}$ is a $\Pi \times N$ matrix of AIM coefficients of the x, y and z components of the basis functions and $\overline{X}$ is a $N \times 1$ vector. The curl of the vector potential is then defined as

$$\vec{A}_2' = \nabla \times \vec{A}_2 = \left(\frac{\partial A_{2z}}{\partial y} - \frac{\partial A_{2y}}{\partial z}\right)\hat{x} + \left(\frac{\partial A_{2z}}{\partial z} - \frac{\partial A_{2z}}{\partial x}\right)\hat{y} + \left(\frac{\partial A_{2y}}{\partial x} - \frac{\partial A_{2z}}{\partial y}\right)\hat{z}, \qquad (5\text{-}30)$$

where x and y components yield zero in a 2-D AIM grid. The z component is solved numerically using the points of the AIM grid (approach adopted from [146]):

$$\begin{aligned}
\frac{\partial A_{2y}}{\partial x} &= \frac{A_{2y}^{(n+1)} - A_{2y}^{(n-1)}}{2\Delta x},\\
\frac{\partial A_{2x}}{\partial y} &= \frac{A_{2x}^{(n+1)} - A_{2x}^{(n-1)}}{2\Delta y},
\end{aligned} \qquad (5\text{-}31)$$

At the edge of the area the gradient is calculated between the adjacent points, i.e., with spacing Δx or Δy.

Finally, the operations are completed with multiplication by AIM coefficients of the z component of the testing function, yielding:

$$\mathcal{K}_2^{\mathcal{F}}\left(\overline{X}\right)=\overline{\overline{U}}_z\overline{A}'_{2z}+\overline{\overline{K}}{}_2^{\Delta}\overline{X}\,, \tag{5-32}$$

where $\overline{\overline{K}}{}_2^{\Delta}$ is the difference of the strong interaction elements between MoM and AIM solution of $\overline{\overline{K}}_2$ in the lower medium i.e.

$$K_{2,ij}^{\Delta}=K_{2,ij}^{AIM}-K_{2,ij}\,, \tag{5-33}$$

$\mathcal{D}_2^{\mathcal{F}}\left(\overline{X}\right)$ is defined by the subsequent operations. First, the vector potential is solved with FFT

$$\begin{aligned}\overline{v}_{2x}&=\mathcal{F}^{-1}\left\{\mathcal{F}\left\{\overline{G}_2\right\}\cdot\mathcal{F}\left\{\overline{\overline{Q}}_x\overline{X}\right\}\right\},\\ \overline{v}_{2y}&=\mathcal{F}^{-1}\left\{\mathcal{F}\left\{\overline{G}_2\right\}\cdot\mathcal{F}\left\{\overline{\overline{Q}}_y\overline{X}\right\}\right\},\\ \overline{v}_{2z}&=\mathcal{F}^{-1}\left\{\mathcal{F}\left\{\overline{G}_2\right\}\cdot\mathcal{F}\left\{\overline{\overline{Q}}_z\overline{X}\right\}\right\},\end{aligned} \tag{5-34}$$

which is then multiplied with the testing function, i.e. the AIM-coefficients of the testing function:

$$\overline{\overline{V}}_2\overline{X}=\overline{\overline{U}}_x\overline{v}_{2x}+\overline{\overline{U}}_y\overline{v}_{2y}+\overline{\overline{U}}_z\overline{v}_{2z}\,. \tag{5-35}$$

For clarity, this outcome would correspond to $\overline{\overline{V}}_2\overline{I}^{eff}$.

In order to solve the correspondence of $\overline{\overline{W}}_2\overline{I}^{eff}$ the following multiplication is performed:

$$\overline{w}_{2x}=-\mathcal{F}^{-1}\left\{\mathcal{F}\left\{\overline{G}_2\right\}\cdot\mathcal{F}\left\{\overline{\overline{Q}}_d\overline{X}\right\}\right\}, \tag{5-36}$$

where $\overline{\overline{Q}}_d$ is the AIM coefficients of the surface divergence of the basis function. Next, the gradient of w_2 is solved:

$$\overline{w}'_2=\nabla\overline{w}_2=\frac{\partial\overline{w}_2}{\partial x}\hat{x}+\frac{\partial\overline{w}_2}{\partial y}\hat{y}+\frac{\partial\overline{w}_2}{\partial z}\hat{z}\,, \tag{5-37}$$

where z component equals zero. The partial differences are solved numerically as in Equation (5-31), and the result is multiplied with the AIM-coefficients of the testing function:

$$\overline{\overline{W}}_2\overline{X}=\overline{\overline{U}}_x\overline{w}'_{2x}+\overline{\overline{U}}_y\overline{w}'_{2y}\,. \tag{5-38}$$

Now, the outcome of the operator can be written as:

$$\mathcal{D}_2^{\mathcal{F}}\left(\overline{X}\right)=k_2^2\overline{\overline{V}}_2\overline{X}+\overline{\overline{W}}_2\overline{X}+D_2^{\Delta}\overline{X}\,, \tag{5-39}$$

where D_2^{Δ} is the difference of the strong interaction elements between MoM and AIM solutions of $\overline{\overline{D}}_2$.

With the above treatment the system matrix multiplication takes the following form; see Equation (5-25):

$$A\left(I^{eff}\right)=\frac{1}{\omega^2\mu_1\varepsilon_2}\mathcal{D}_1^{\mathcal{F}}\left(\mathcal{D}_2^{\mathcal{F}}\left(I^{eff}\right)\right)+\mathcal{K}_1^{\mathcal{F}}\left(\mathcal{K}_2^{\mathcal{F}}\left(I^{eff}\right)\right), \qquad (5\text{-}40)$$

which yields the following equation for the iteration process:

$$A\left(I^{eff}\right)=\overline{b}\,, \qquad (5\text{-}41)$$

where $\overline{b}$ is the excitation vector.

5.2.3 Simulation results

In this Section, first the formulation is demonstrated using a sphere, then scattering from sample surfaces is calculated and accuracy evaluated, and finally, the efficiency is discussed.

Demonstration with sphere

The formulation was verified by computing the radar cross section (RCS) of a sphere and comparing that to the exact solution of RCS of the sphere. Figure 5-8 shows both the exact and the numerical solution. The radius of the sphere is 0.5 m, relative permittivity ε_{r2} = 4 and frequency 100 MHz. The sphere was illuminated with the plane wave traveling to the direction of *z*-axis. The electric field of the plane wave was in the direction of the y-axis and the result is plotted in the *yz*-plane. The exact and numerical solutions coincide accurately. The difference at the minimum is due to the discretization of the ball, which was divided into only 960 RWG basis functions.

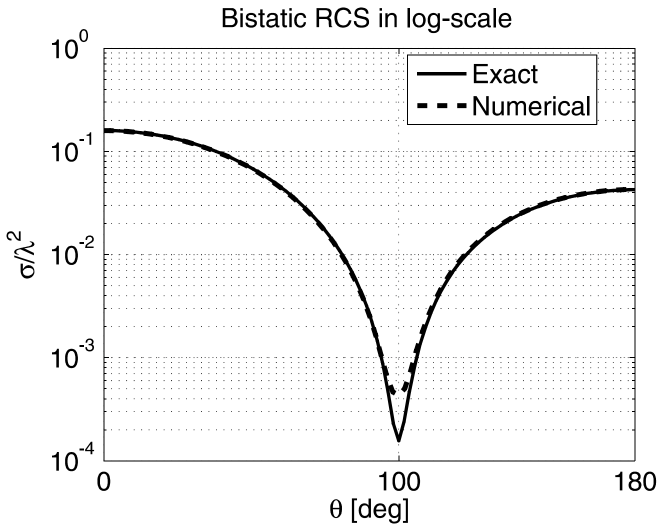

Figure 5-8. Bistatic radar cross section (RCS), in units of λ^2, of a dielectric sphere with ε_{r2} = 4.

Bistatic scattering coefficients

Bistatic scattering coefficients (BSC) were simulated with the presented method. Figure 5-9 and Figure 5-10 show the averaged scattering results in terms of BSC for the cases where the RMS roughnesses of ten realizations of surfaces are 0.1 and 0.2 wavelengths, respectively. The surfaces were created following the principles presented in [166], which allow creation of random surfaces with Gaussian or non-Gaussian roughness. The frequency in the calculation was 14 GHz and the relative permittivity of the lower medium is $\varepsilon_{r2} = 39.7 + i40.2$. The size of the surface is 16 λ^2, which is divided into 2133 edges of RWG basis functions. The surface was illuminated from the nadir direction with a Gaussian tapered beam as described in the previous Section 5.2.1.

In order to solve the scattering using the AIM a 14 by 14 grid was laid out onto the level of the mean of the surface height. The grid extends over the surface borders in *x*- and *y*-directions in order to allow the determination of the translated functions for the original functions also on the borders of the surface. The translated functions were combinations of 16 coefficients ($M = 3$). In Figure 5-10 the maximum does not point exactly to the nadir, which is due to the fact that the beam was narrow on the surface with respect to the correlation length of the surface.

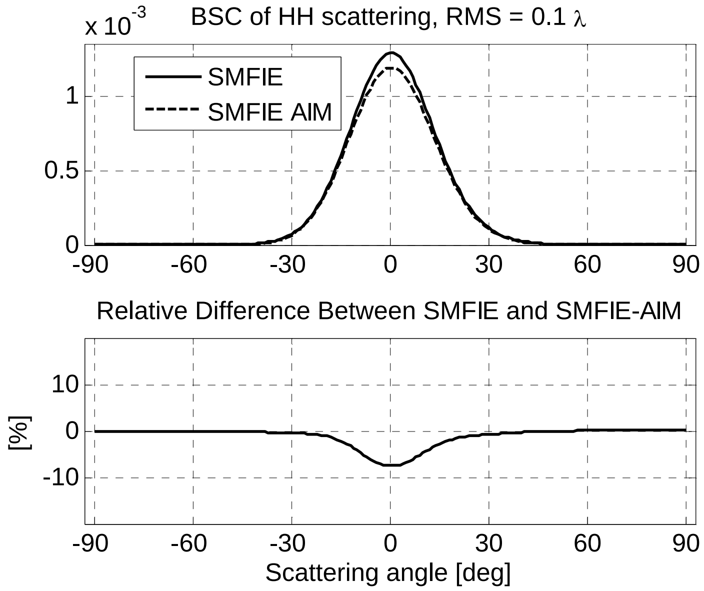

Figure 5-9. Bistatic scattering coefficient (BSC) of averaged HH scattering from ten realizations of surfaces with 0.1 λ RMS roughness and 1 λ correlation length. The surface size is 16 λ^2 and the surface is illuminated from the nadir direction.

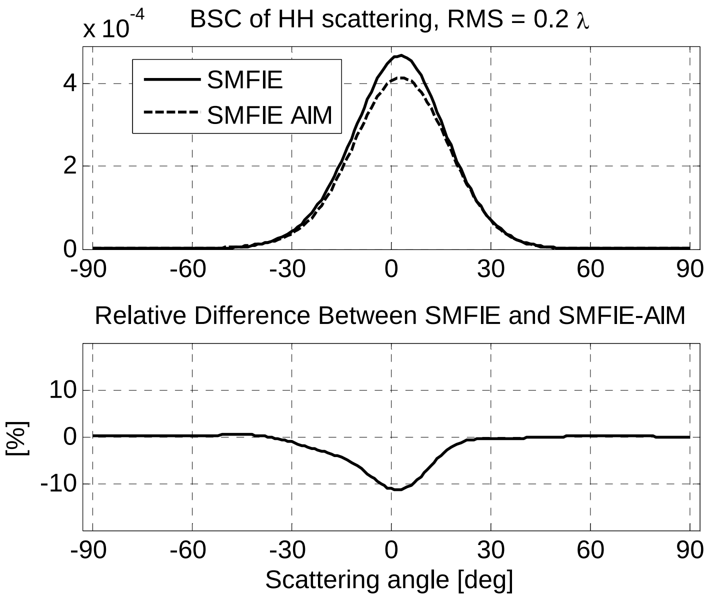

Figure 5-10. Bistatic scattering coefficient (BSC) of averaged HH scattering from ten realizations of surfaces with 0.2 λ RMS roughness and 1 λ correlation length. The surface size is 16 λ^2 and the surface is illuminated from the nadir direction.

The result shows that as the roughness increases the difference between solution using only SMFIE and the solution using SMFIE with AIM increases. This is clearly due to the fact that the AIM coefficients are evaluated on the *xy*-plane and as the roughness increases the distance of these points to the actual surface points increases causing uncertainty.

Figure 5-11 shows averaged scattering in terms of BSC from ten realizations of 100 λ^2 surface, which were divided into 18565 edges of RWG basis functions. The surface roughness was 0.2 λ RMS and the correlation length 1 λ. The shape of the scattering pattern is narrower than the one observed in Figure 7 (same roughness). This is due to the fact that as a larger surface area is illuminated, the main lobe of scattering is narrower having sidelobes with more random amplitude and phase in each scattering realization. The result shows the feasibility of the method to solve scattering from large surface areas, and therefore, the method can be utilized in the development of wind vector retrieval, or other applications, also in 36.5 GHz or 1.4 GHz range.

All results were obtained with very modest computational power; standard PC computer with one gigabyte of memory. With AIM, the computation time grows as $N \log N$ and the memory requirement as N, where N is the number of unknowns [167]. This represents state-of-the-art performance. Obtained accuracy compares well with that of other presented methods, although reports on precise accuracy values are hard to find. It is noted that an error of 10% corresponds to 0.5 dB, which commonly goes even undetected due to the use of decibel scale plots.

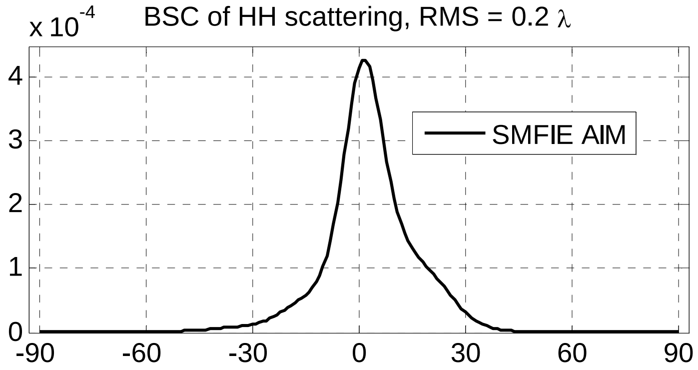

Figure 5-11. Bistatic scattering coefficient (BSC) of averaged HH scattering from ten realizations of surfaces with 0.2 λ RMS roughness and 1 λ correlation length. The surface size is 100 λ^2, and the surface is illuminated from the nadir direction.

Convergence speed

The results were calculated using generalized minimum residual method (GMRES) without preconditioner or restart. The convergence speed of GMRES for the SMFIE solution was also studied since it was indicated in [73] that the SMFIE should perform very efficiently with iterative methods. In the abovementioned cases the solution (to the accuracy of 10^{-6}) was found in 7 to 11 iterations, including the solutions to scattering from the larger surfaces. Hence, the efficiency of the SMFIE is regarded excellent and SMFIE formulation very suitable for solving this kind of problems.

5.2.4 Discussion

In general, AIM provides a straightforward and efficient way to speed up the calculation of matrix-vector product. AIM is also significantly less complex than multipole method or SMCG. In principle, these methods are optional solutions for rough surface scattering, but beyond this, AIM seems to have a wider field of applictions.

The presented method offers flexibility to apply it to any surface emission problem, as emission can be retrieved from scattering properties of a surface using Equations (2-13) and (2-15). In the context of this work, the obvious application is the simulation of polarimetric brightness temperature of the ocean surface. Using wind speed driven surface roughness models, which are continuously developed, the challenge is foreseen to be the obtaining of full understanding of the relationship between wind speed and polarimetric brightness temperature. In an optimum case, time series of exact geometry, physical temperature and permittivity of a wind driven ocean surface area could be the input of the simulation, exploiting fully the ability of the method to simulate emission from a precise geometrical structure at any azimuth and incidence angle (as opposed to the simulations using statistical input parameters).

Furthermore, for global applications, like the SMOS mission, accurate simulations of polarimetric brightness temperature at various frequencies emitted by large ocean surface areas would be very beneficial, for example, in the setting of mission goals and instrument requirements, as there are no experimental data before the launch of the mission.

However, as mentioned before, these applications of the presented methodology fall out of the scope of the work carried out within this Doctoral Thesis.

5.3 Contribution of the work to the polarimetric wind vector radiometry

The dependency and sensitivity of the Fourier harmonic coefficients of the Stokes parameters on incidence angle were presented [P5]. Especially, the behavior of the harmonics of the 3rd Stokes parameter is interesting, as it has not been studied in detail previously. Furthermore, a preliminary wind speed model as a function of the harmonics and incidence angle was presented with comparable accuracy. Furthermore, the results given as a function of incidence angle contributes to the wind vector retrieval studies, as this type of data is not common.

For the simulation of the ocean surface scattering and emission a new efficient method was developed and demonstrated [P6]. With this method, microwave emission from ocean surface, at given frequency, can be predicted deterministically for any given azimuth and incidence angle, which is very valuable for wind vector measurement technique development.

6 CONCLUSIONS

In this work the development and calibration of the polarimetric reference radiometer of the ESA's SMOS mission was presented. The SMOS mission uses an L-band interferometric synthetic aperture radiometer for measurement of soil moisture and ocean salinity. Furthermore, the work contributes to the most important application of the polarimetric radiometers, maritime wind vector retrieval, in two respects: the dependency as a function of the incidence angle was studied in detail using an airborne dataset, and an efficient method for simulation of scattering from dielectric rough surface, like ocean surface, was introduced.

It was demonstrated that the reference radiometer meets its operational requirements. This includes measurement of the internal noise source of the interferometric radiometer, and polarimetric measurement of the average brightness temperature incident to the instrument. The calibration of the instrument presents a challenge due to the fact that only one external calibration target can be used; this is overcome by very precise characterization of the front-end parts. The characterization principles were described and demonstrated. Additionally, a new method was developed and demonstrated for the calibration of the phase imbalance of the channels of the radiometer.

The wind vector retrieval as a function of the incidence angle was studied. The sensitivity of the harmonic coefficients of the Stokes parameters to the wind speed as a function of incidence angle was determined, and a wind speed model as a function of the incidence angle was finally given. These new results show promising accuracy. With respect to the wind vector retrieval, an efficient method for simulating the rough dielectric surface scattering was introduced. It presents a new combination of a known formulation for the scattering problem with another method for speed up the calculation. The simulation results show very efficient behavior with good accuracy. In combination with the study of the Stokes parameter measurements, the model presents excellent potential for investigation of wind vector retrieval development.

The work contained in this work contributes significantly to the scientific field of passive microwave remote sensing with its novel methodology related to instruments, their calibration, and applications.

7 SUMMARY OF APPENDED PAPERS

[P1]

Publication [P1] presents the calibration of a synthetic aperture radiometer, and how the operation of the reference radiometer is linked to the calibration of this instrument. In the publication the calibration approach of MIRAS with the distributed noise injection and the reference radiometer is described in detail, and the processing to the Level 1 data products is presented. The purpose of the reference radiometer is to provide the accurate measurement of the distributed noise injection and average brightness temperature of the scene. Application of these parameters to the overall calibration scheme is described.

[P2]

In publication [P2], the operational principles of the prototype of the reference radiometer are introduced. The publication includes a description of the central concept for solving the third and fourth Stokes parameter with a noise injection radiometer and digital correlator, and the measurement of the noise level of the internal calibration source of the synthetic aperture radiometer. The operational principles are described in detail and experimental results validating the polarimetric operation are presented. Additionally, self-interference issue related to the polarimetric measurement is discussed and experimental results are included.

[P3]

In publication [P3], the flight model of the reference radiometer and the full calibration programme are presented. The publication includes description of the instrument, analysis of the operation of the radiometer, calibration equations, on-ground calibration methods and results, and procedures for the calibration in the orbit. The ground calibration principles are described in detail, and an accurate method for loss measurement is demonstrated. The experimental results show that the instrument meets the requirements dictated by the measurement goal of the mission.

[P4]

Publication [P4] introduces a measurement procedure for calibrating the phase imbalance of a polarimetric radiometer. The method introduces a novel and practical way to measure the phase imbalance of a correlating polarimetric radiometer. The technique is applied to the reference radiometer. The fundamental underlying theory is introduced; the technique is based on measurement of a polarized source with two different angles with respect to the polarization plane of the antenna of the radiometer. An experiment demonstrating both robustness and accuracy of the method is finally presented.

[P5]

In publication [P5] airborne polarimetric measurements of sea surface with varying wind speed are analyzed in order to determine the incidence angle dependency of the measured signal. The retrieval of the maritime wind vector is the most important application. The goal of this publication is to contribute to the accuracy and flexibility of the method. The measurement campaigns include measurements over reasonable incidence angle and wind speed range producing a versatile data set. The publication presents the theory for the analyzing the results, and shows results with a model for incidence angle dependency of the harmonics of the Stokes parameters and, furthermore, a wind speed model as a function of incidence angle and the harmonics. The accuracy of the obtained results demonstrates the feasibility of the model.

[P6]

In Publication [P6], a numerical simulation method for rough surfaces is presented. It is based on the integral equation method derived from the Maxwell equations. The method combines a fast-convergence formulation SMFIE (Single Magnetic Field Integral Equation) with AIM (Adaptive Integral Method), which uses FFT (Fast Fourier Transform) to speed up the computation. The paper describes the theory and formulation with a demonstration, and finally, shows the efficiency of the method for the simulation of rough dielectric surface scattering.

REFERENCES

[1] T. M. Lillesand and R. W. Kiefer, “Remote Sensing and Image Interpretation, 4th Edition”, New York, USA: John Wiley & Sons, 2000

[2] T. Manninen, P. Stenberg, M. Rautiainen, P. Voipio, H. Smolander, “Leaf area index estimation of boreal forest using ENVISAT ASAR”, IEEE Trans. Geosci. Remote Sensing, vol. 43, no. 11, pp. 2627-2635, November 2005

[3] Ulaby, F.T., Moore, R. K., Fung, A. K., “Microwave Remote Sensing Active and Passive, Volume 1, Fundamentals and Radiometry”, 1981, Addison-Wesley Publishing Company, 456 pp.

[4] R. W. Newton and J. W. Rouse, Jr., “Microwave radiometer measurements of soil moisture content”, IEEE Trans. Antennas Propagat., vol. 28, pp. 680-686, 1980

[5] W. L. Crosson, A. S. Limaye, C. A. Laymon, “Parameter sensitivity of soil moisture retrievals from airborne L-band radiometer measurements in SMEX02”, IEEE Trans. Geosci. Remote Sensing, vol. 43, no. 7, pp. 1517-1528, July 2005

[6] W. L. Crosson, A. S. Limaye, C. A. Laymon, “Parameter sensitivity of soil moisture retrievals from airborne C- and X-band radiometer measurements in SMEX02”, IEEE Trans. Geosci. Remote Sensing, vol. 43, no. 12, pp. 2842-2853, December 2005

[7] J. Grandell, J. Pulliainen, and M. Hallikainen, “Sub-pixel land use classification of retrieval of forest stem volume in the boreal forest zone by employing SSM/I data”, Remote Sensing of Environment, vol. 63, no. 1, pp. 140-154, March 1998

[8] G. C. Thomann, “Experimental results of the remote sensing of sea-surface salinity at 21-cm wavelength”, IEEE Trans. Geosci. Electron., vol. GE-14, pp. 198-214, 1976

[9] C. T. Swift, “Microwave radiometer measurements of the Cape Cod canal,” Radio Sci., vol. 9, pp. 641-653, 1974

[10] S. H. Yueh, W. J.Wilson, F. K. Li, S.V. Nghiem, and W. B. Ricketts, “Polarimetric brightness temperatures of sea surface measured with aircraft K- and Ka-band radiometers”, IEEE Trans. Geosci. Remote Sensing, vol. 35, no. 5, pp. 1177-1187, September 1997.

[11] M. Hallikainen, “Retrieval of snow water equivalent from Nimbus-7 SMMR data: Effect of land-cover categories and weather conditions”, IEEE J. Oceanic Eng., vol. 9, no. 5, pp. 372-376, December 1984

[12] J. T. Pulliainen, J. Grandell, and M. T. Hallikainen, “HUT snow emission model and its applicability to snow water equivalent retrieval”, IEEE Trans. Geosci. Remote Sensing, vol. 37, no. 3, pp. 1378-1390, May 1999

[13] C. T. Swift “An algorithm to measure sea ice concentration with microwave radiometers”, J. Geophys. Res., vol. 90, pp. 1087-1099, 1985

[14] R. Meneghini, H. Kumagai, J. Wang, T. Iguchi, T. Kozu, “Microphysical Retrievals over Stratiform Rain Using Measurements from an Airborne Dual-Wavelength Radar-Radiometer,” IEEE Trans. Geosci. Rem. Sens, vol 35, no. 3, 1997.

[15] M. T. Hallikainen, P. Halme, M. Takala, J. Pulliainen, “Combined active and passive microwave remote sensing of snow in Finland“, Proc. 2003 IEEE Int. Geosci. Remote Sensing Symposium 2003, IGARSS’03, vol. 2, pp. 830-832, Toulouse, France, July 21-25, 2003

[16] R. H. Dicke, “The measurement of thermal radiation at microwave frequencies”, Rev. Scientific Instruments, vol. 17, no. 7, pp. 268-275, July 1946

[17] R. H. Dicke, R. Beringer, R. L. Kyhl, and A. B. Vane, “Atmospheric absorption measurements with a microwave radiometer”, Phys. Rev., vol. 70, pp. 340-348, September 1946

[18] A. W. Straiton, C. W. Tolbert, and C. O. Britt, “Apparent temperature distributions of some terrestrial materials and the Sun at 4.3 mm wavelength”, J. Appl. Phys., vol. 29, pp. 776-782, 1958

[19] J-P. Hach, “A very sensitive airborne microwave radiometer using two reference temperatures”, IEEE Trans. Microwave Theory Tech., vol. 16, no. 9, pp. 629-636, September 1968

[20] W. Nordberg, J. Conaway, and P. Thaddeus, “Microwave observation of sea state from aircraft”, Quart. J. Roy. Meteorol. Soc., vol. 95, pp. 408-413, 1969

[21] M. C. Hoover and R. P. Moore, “Am airborne Ka-band microwave radiometric measurement mapping system, “ Proc. SPIE, vol. 27, pp. 147-156, 1971

[22] A. S. Gurvich and V. V. Demin, “Determination of the total moisture content in the atmosphere from measurements on the Cosmos 243 satellite”, Bull. (Izv.) Acad. Sci. USSR, Atmospheric and Oceanic Physics, vol. 6, no. 8, pp. 771-779, 1970

[23] A. Ishimaru, “Wave Propagation and Scattering in Random Media, Volume 1, Single Scattering and Transport Theory”, 1978, Academic Press, 250 pp.

[24] C. H. Mayer, T. P. McCullough, and R. M. Sloanaker, “Evidence for polarized radio radiation from the Crab nebula”, Astrophysical J., vol. 126, pp. 468-470, 1957

[25] K. Akabane, “A polarimeter in the microwave region”, Proc. IRE, pp. 194-197, January 1958

[26] M. S. Dzura, V. S. Etkin, A. S. Khrupin, M. N. Pospelov, and M. D. Raev, “Radiometers-polarimeters: principles of design and application for sea surface microwave emission polarimetry”, Proc. 1992 IEEE Int. Geosci. Remote Sensing Symposium 1992, IGARSS’92, pp. 1432-1434, Houston, Texas, USA, May 26-29, 1992

[27] A. J. Gasiewski, D. B. Kunkee, “Calibration and applications of polarization-correlating radiometers”, IEEE Trans. Microwave Theory Tech., vol. 41, no. 5, pp. 767-773, May 1993

[28] S. H. Yueh, W. J.Wilson, F. K. Li, S.V. Nghiem, and W. B. Ricketts, “Polarimetric measurements of sea surface brightness temperatures using an aircraft K-band radiometer”, IEEE Trans. Geosci. Remote Sensing, vol. 33, pp. 85-92, January 1995.

[29] P. W. Gaiser, et al, “The WindSat spaceborne polarimetric microwave radiometer: sensor description and early orbit performance,” IEEE Trans. Geosci. Remote Sens., vol. 42, no. 11, pp. 2347-2361, November 2004.

[30] C. Ruf, C. T. Swift, A. B. Tanner, D. M. Le Vine, “Interferometric Synthetic Aperture Microwave Radiometry for the Remote Sensing of the Earth”, IEEE Trans. Geosci. Remote Sensing, vol. 26, no. 5, pp. 597-611, September 1988

[31] D. M. Le Vine, “Synthetic aperture radiometer systems”, IEEE Trans. Microwave Theory Tech., vol. 47, no. 12, pp. 2228-2236, December 1999

[32] J. D. Kraus, ”Radio Astronomy”, New York: McGraw-Hill, 1966

[33] P. J. Napier et al, “The very large array: design and performance of a modern synthesis radio telescope”, Proc. IEEE, vol. 71, no. 11, pp. 1295-1320, November 1983

[34] D. M. Le Vine, M. Kao, C. T. Swift, A. Griffis, A. B. Tanner, ”Initial results in the development of a synthetic aperture microwave radiometer”, IEEE Trans. Geosci. Remote Sensing, vol. 28, iss. 4, pp. 614-619, July 1990

[35] D. M. Le Vine, A. J. Griffis, C. T. Swift, T. J. Jackson, “ESTAR: a synthetic aperture microwave radiometer for remote sensing applications, Proc. IEEE, vol. 82, no. 12, pp. 1787-1801, December 1994

[36] J. Kainulainen, K. Rautiainen, S. Tauriainen, T. Auer, J. Kettunen, M. Hallikainen, “First 2-D Interferometric Radiometer Imaging of the Earth from an Aircraft”, IEEE Geosci. Remote Sensing Letters, in press 2007

[37] S. Ribo, M. Martin-Neira, I. Cabeza, S. Tauriainen, N. Duffo, “MIRAS Airborne Demonstrator” Proc. IEEE MicroRad 2006, pp. 45-49, San Juan, Puerto Rico, February 28-March 3, 2006

[38] M. Martin-Neira and J.M. Goutoule, “A two-dimensional aperture synthesis radiometer for soil moisture and ocean salinity observations”, ESA Bulletin, no. 92, pp. 95-104, November 1997

[39] P. Silvestrin, M. Berger, Y. Kerr and J. Font, “ESA’s second Earth Explorer Opportunity Mission: The Soil Moisture and Ocean Salinity mission - SMOS”,IEEE Geoscience and Remote Sensing Newsletter, no. 118, pp. 11-14, March 2001

[40] A. B. Tanner, W. J. Wilson, B. H. Lambrigtsen, S. J. Dinardo, S. T. Brown, P. P. Kangaslahti, T. C. Gaier, C. S. Ruf, S. M. Gross, B. H. Lim, S. Musko, S. Rogacki, J. R. Piepmeier, “Initial Results of the Geostationary Synthetic Thinned Array Radiometer (GeoSTAR) Demonstrator Instrument” IEEE Trans. Geosci. Remote Sensing, vol. 45, no. 7, pp. 1947-1957, July 2007

[41] J. Christiansen, A. Carlström, Hans Ekström, A. Emrich, Johan Embertsen, Peter de Maagt, A. Colliander, “GEO: the Geostationary Atmospheric Sounder”, Proc. 2007 IEEE Int. Geosci. Remote Sensing Symposium, IGARSS’07, Barcelona, Spain, July 23-27, 2007

[42] A. R. Harvey, A. H. Greenway, A. Camps, I. Corbella, F. Torres, J. Bará, M. Martin-Neira, “Millimetre-wave aperture synthesis radiometry for snow and ice mapping”, Proc. 1999 IEEE Int. Geosci. Remote Sensing Symposium, IGARRS'99, vol. 1, pp. 419-421, Hamburg, Germany, June 28-July 2,1999

[43] W. J. Wilson, A. B. Tanner, B. H. Lambrigtsen, T. A. Doiron, J.R. Piepmeier, C. S. Ruf, ”STAR concept for passive microwave temperature sounding from middle Earth orbit (MeoSTAR)”, Proc. 2004 IEEE Int. Geosci. Remote Sensing Symposium, IGARSS’04, vol. 2, pp. 789-790, Anchorage, Alaska, USA, September 20-24, 2004

[44] Y. H. Kerr, P. Waldteufel, J-P. Wigneron, J. Martinuzzi, J. Font, M. Berger, “Soil moisture retrieval from space: the Soil Moisture and Ocean Salinity (SMOS) mission”, IEEE Trans. Geosci. Remote Sensing, vol. 39, no. 8, pp. 1729-1735, August 2001

[45] J. Font, G.S.E. Lagerloef, D.M. Le Vine, A. Camps, O.-Z. Zanife, “The determination of surface salinity with the European SMOS space mission”, IEEE Trans. Geosci. Remote Sensing, vol. 42, iss. 10, pp. 2196-2205, October 2004

[46] A. B. Tanner, C. T. Swift, ”Calibration of a synthetic aperture radiometer”, IEEE Trans. Geosci. Remote Sensing, vol. 31, no. 1, pp. 257-267, January 1993

[47] F. Torres, A. Camps, J. Bara, I. Corbella, R. Ferrero, “On-board phase and modulus calibration of large aperture synthesis radiometers: study applied to MIRAS”, IEEE Trans. Geosci. and Remote Sensing, vol. 34, no. 4, pp. 1000-1009, July 1996

[48] I. Corbella, N. Duffo, M. Vall-llossera, A. Camps, F. Torres, “The visibility function in interferometric aperture synthesis radiometry”, IEEE Trans. Geosci. Remote Sensing, vol. 42, no. 8, pp. 1677-1682, August 2004

[49] A. Camps, I. Corbella, F. Torres, M. Vall-llossera, N. Duffo, “Polarimetric formulation of the visibility function equation including cross-polar antenna patterns”, IEEE Geosci. Remote Sensing Letters, vol. 2, no. 3, pp. 292-295, July 2005

[50] F. Torres, I. Corbella, A. Camps, N. Duffo, M. Vall-llosera, S. Beraza, C. Gutiérrez, M. Martín-Neira, “Denormalization of Visibilities for In-Orbit Calibration of Interferometric Radiometers”, vol. 44, no. 10, pp. 2679-2686, October 2006

[51] L. Tsang, J. A. Kong, and R. T. Shin, “Theory of Microwave Remote Sensing“, New York, USA: John Wiley & Sons, 1985

[52] J. Lahtinen, A. J. Gasiewski, M. Klein, I. S. Corbella, “A calibration method for fully polarimetric microwave radiometers”, IEEE Trans. Geosci. Remote Sensing, vol. 41, no. 3, pp. 588-602, March 2003

[53] J. B. Hagen and D. T. Farley, “Digital-correlation techniques in radio science,” Radio Sci., vol. 8, no. 8-9, pp. 775–784, 1973.

[54] J.R. Piepmeier, A.J. Gasiewski, ”Digital Correlation Microwave Polarimetry: Analysis and Demonstration"”, IEEE Trans. Geosci. Remote Sensing, vol. 39, no. 11, pp. 2392-2410, November 2001.

[55] C. S. Ruf, J. Li, “A Correlated Noise Calibration Standard for Interferometric, Polarimetric, and Autocorrelation Microwave Radiometers”, IEEE Trans. Geosci. Remote Sensing, vol. 41, no. 10, pp. 2187-2196, October 2003

[56] J. R. Piepmeier and A. J. Gasiewski, “High-resolution passive polarimetric microwave mapping of ocean surface wind vector fields”, IEEE Trans. Geosci. Remote Sensing, vol. 39, no. 3, pp. 606-622, March 2001.

[57] B. Laursen and N. Skou, “Wind direction over ocean determined by an airborne, imaging, polarimetric radiometer system”, IEEE Trans. Geosci. Remote Sensing, vol. 39, no. 7, pp. 1547-1555, July 2001.

[58] J. Lahtinen, J. Pihlflyckt, I. Mononen, S. Tauriainen, M. Kemppinen, and M. Hallikainen, “Fully polarimetric microwave radiometer for remote sensing”, IEEE Trans. Geosci. and Remote Sensing, vol. 41, no. 8, pp. 1869-1878, August 2003.

[59] M. H. Freilich and B. A. Vanhoff, “The Accuracy of preliminary WindSat vector wind measurements: comparison with NDBC Bouys and QuickSCAT“, IEEE Trans. Geosci. Remote Sensing, vol. 44, no. 3, pp. 622-637, March 2006

[60] S. V. Nghiem, M. E. Veysoglu, J. A. Kong, R. T. Shin, K. O’Neill, and A. W. Lohanick, “Polarimetric passive remote sensing of a periodic soil surface: microwave measurements and analysis,” J. Electromag. Waves Appl., vol. 5, no. 9, pp. 997-1005, 1991.

[61] S. Sobjaerg and N. Skou, “Polarimetric signature from crop covered land surface measured by an L-band polarimetric radiometer,” Proc. 2003 IEEE Int. Geosci. Remote Sensing Symposium, IGRASS’03, pp. 2626-2628, Toulouse, France, July 21-25, 2003.

[62] P. S. Narvekar, T. J. Jackson, R.Bindlish, L. Li, “Observations of Land Surface Passive Polarimetry with WindSat”, Proc. IEEE MicroRad 2006, pp. 160-164, San Juan, Puerto Rico, February 28-March 3, 2006

[63] S. L. Chuang and J. A. Kong, “Wave scattering from a periodic dielectric surface for a general angle of incidence,” Radio Sci., vol. 17, no. 3, pp. 545-557, 1982

[64] J. T. Johnson, J. A. Kong, R. T. Shin, D. H. Staelin, K. O'Neill, A. W. Lananick, “Third Stokes parameter emission from a periodic water surface”, IEEE Trans. Geosci. Remote Sensing, vol. 31, no. 5, pp. 1066-1080, September 1993

[65] S. H. Yueh, W. J. Wilson, S. J. Dinardo, and F. K. Li, “Polarimetric microwave brightness signatures of ocean wind directions”, IEEE Trans. Geosci. Remote Sensing, vol. 37, no. 2, pp. 949-959, March 1999.

[66] S. H. Yueh, W. J. Wilson, S. J. Dinardo, S. V. Hsiao, “Polarimetric Microwave Wind Radiometer Model Function and Retrieval Testing for WindSat”, IEEE Trans. Geosci. Remote Sensing, vol. 44, no. 3, pp. 584-596, March 2006

[67] F. J. Wentz, “A model function for ocean microwave brightness temperature”, J. Geiphys. Res., vol. 88, no. C3, pp. 1892-1907, 1983

[68] S. L. Durden, J. F. Vesecky, “A physical radar cross-section model for a wind-driven sea with swell”, IEEE J. Oceanic Eng., vol. OE-10, no. 4, pp. 445-451, October 1985

[69] S. H. Yueh, “Modeling of wind direction signals in polarimetric sea surface brightness temperatures”, IEEE Trans. Geosci. Remote Sensing, vol. 35, no. 6, November 1997

[70] D. R. Lyzenga, J. F. Vesecky, ”Two-scale polarimetric emissivity model: efficiency improvements and comparisons with data”, Prog. Electromagn. Res. PIER, vol. 37, pp. 205-219, 2002

[71] J.T. Johnson, R.T. Shin, J.A. Kong, L. Tsang, and K. Pak, “A Numerical Study of Ocean Polarimetric Thermal Emission”, IEEE Transactions on Geoscience and Remote Sensing, vol. 37, no. 1, pp. 8-20, January 1999.

[72] A. J. Poggio, and E. K. Miller, “Integral equation solutions of three-dimensional scattering problems”, Computer Techniques for Electromagnetics, R. Mittra, Ed. New York, USA: Pergamon, 1973

[73] M. S. Yeung, “Single Integral Equation for Electromagnetic Scattering by Three-Dimensional Homogeneous Dielectric Objects”, IEEE Transactions on Antennas and Propagation, vol. 47, no. 10, pp. 1615-1622, October 1999.

[74] M. S. Yeung, “Solution of electromagnetic scattering problems involving three dimensional homogeneous dielectric objects by the single integral equation method”, SIAM Journal of Scientific Computing, Vol. 15, No. 1, pp. 1 - 17, 2000.

[75] S. M. Rao, D.R. Wilton and A.W. Glisson, “Electromagnetic Scattering by Surfaces of Arbitrary Shape”, IEEE Transactions on Antennas and Propagation, vol. AP-30, no. 3, pp. 409-418, May 1982.

[76] E. Bleszynski, M. Bleszynski and T. Jaroszewicz, “AIM: Adaptive Integral Method for Solving Large-Scale Electromagnetic Scattering and Radiation Problems”, Radio Science, vol. 31, pp. 1225-1251, September-October 1996

[77] M. Planck, “On the Law of Distribution of Energy in the Normal Spectrum”, Annalen der Physik, vol. 4, p. 553 ff, 1901

[78] J. C. Maxwell, “A Dynamical Theory of the Electromagnetic Field”, Philosophical Transactions of the Royal Society of London 155, 459-512, 1865

[79] W. H. Peake, “Interaction of Electromagnetic Waves with Some Natural Surfaces”, IRE Trans. Ant. Prop, vol. 7, no. 5, pp. 324-329, December 1959

[80] M. E. Tiuri, “Radio Astronomy receivers”, IEEE Trans. Antennas and Propagation, vol. 12, pp. 931-938, December 1964

[81] E. Salonen, “A polarization measurement system for radio astronomical observations at the millimeter wave range”, Licentiate Thesis (in Finnish). Espoo, Finalnd: Helsinki University of Technology, 1986

[82] K. Akabane, “A polarimeter in the microwave region”, Proc. IRE, pp. 194-197, January 1958

[83] J. P. Bobak, B. C. Hicks, L. A. Rose, N. R. McGlothlin, S. R. Quinn, D. J. Dowgiallo, T. E. von Rentzell, “APMIR: an airborne polarimeter designed for high accuracy”, OCEANS 2003, Proceedings, vol. 1, pp. 211-216, 2003

[84] N. Skou, B. Laursen, S. S. Sobjarg, “Polarimetric radiometer configurations: potential accuracy and sensitivity”, IEEE Trans. Geosci. Remote Sensing, vol. 37, no. 5, pp. 2165-2171, September 1999

[85] O. Koistinen, J. Lahtinen, M. Hallikainen, ”Comparison of analog continuum correlators for remote sensing and radio astronomy”, IEEE Trans. Intr. Meas., vol. 51, no. 2, pp. 227-234, April 2002

[86] National Oceanic and Atmospheric Administration, Environmental Technology Laboratory (NOAA/ETL), “Polarimetric Scanning Radiometer” [online]. Colorado, USA [cited Jan. 18, 2007]. Available HTTP: http://www.etl.noaa.gov/technology/psr

[87] J. H. Van Vleck and D. Middleton, “The spectrum of clipped noise,” Proc. IEEE, vol. 54, no. 1, pp. 2–19, January 1966.

[88] D. M. Le Vine, “The sensitivity of synthetic aperture radiometers for remote sensing applications from space”, Radio Sci., vol. 25, no. 4, pp. 441-453, July-August 1990

[89] C. S. Ruf, “Error analysis of image reconstruction by a synthetic aperture interferometric radiometer”, Radio Sci., vol. 26, no. 6, pp. 1419-1434, November-December 1991

[90] N. Skou, “Microwave radiometer linearity measured by simple means”, Proc. 2002 IEEE Int. Geosci. Remote Sensing Symposium, IGARSS'02, vol. 6, pp. 3664-3667, Toronto, Canada, June 24-28, 2002

[91] A. Camps, J. Bará, F. Torres, I. Corbella, J. Romeo, “Impact of antenna errors on the radiometric accuracy of large aperture synthesis radiometers”, Radio Sci., vol 32., no. 2, pp. 657-668, March-April 1997

[92] A. Camps, N. Skou, F. Torres, I. Corbella, N. Duffo, Mercè Vall-llosera, “Considerations about antenna pattern measurements of 2-D aperture synthesis radiometers”, IEEE Geosci. Remote Sensing Letters, vol. 3, no. 2, pp. 259-261, April 2006

[93] A. Camps, F. Torres, I. Corbella, J. Bará, P. de Paco, “Mutual coupling effects on antenna radiation pattern: An experimental study applied to interferometric radiometers”, Radio Sci., vol. 33, no. 6, pp. 1543-1552, November-December 1998

[94] A. Camps, F. Torres, I. Corbella, J. Bara, J. A. Lluch, “Threshold and timing errors of 1 bit/2 level digital correlators in Earth observation synthetic aperture radiometry”, Electronics letters, 24th April 1997, Vol. 33, No. 9

[95] F. Torres, A. Camps, J. Bará, I. Corbella, “Impact of receiver errors on the radiometric resolution of large two-dimensional aperture synthesis radiometers”, Radio Sci., vol. 32, no 2., pp. 629-641, March-April 1997

[96] I. Corbella, A. Camps, F. Torres, and J. Bará, “Analysis of noise-injection networks for interferometric radiometer calibration,” IEEE Trans. Microw. Theory Tech., vol. 48, no. 4, pp. 545–552, April 2000.

[97] A. Camps, F. Torres, J. Bara, I. Corbella, F. Monzon, "Automatic Calibration of Channels Frequency Response in Interferometric Radiometers", Electronics Letters, Vol. 35 No 2, pp 115-116, 21 January 1999

[98] P. Piironen, "PMS offset determination using an IF attenuator". Technical note, ESA-ESTEC, 16 May 2002

[99] F. Torres, N. Duffo, I. Corbella, A. Camps, M. Vall-llossera, S. Ribó, "MIRAS-SMOS: The Relative Instrumental Error Calibration Approach", Proc. 8th Specialist Meeting on Microwave Radiometry and Remote Sensing Applications, MicroRad'04, Rome, Italy, 2004

[100] S. S. Söbjärg, "Polarimetric Radiometers and their Applications", Doctoral Thesis, Örstedt, Denmark: Technical University of Denmark, 2002

[101] A. E. Lipton, "Polarization of measurement for microwave temperature sounding of the mesosphere", IEEE Trans. Geosci. Remote Sensing, vol. 40, no. 8, pp. 1669-1681, August 2002

[102] B. G. Kutuza, G. K. Zagorin, A. Hornbostel, A. Schroth, "Physical modeling of passive polarimetric microwave observations of the atmosphere with respect to the third Stokes parameter", Radio Sci. ,vol. 33, no. 3, pp. 677-695, May-June 1998

[103] A. Hornbostel, A. Schroth, A. Sobachkin, "Passive and active vector measurements of microwave emission and scattering by precipitation", Proc. 1999 IEEE Int. Geosci. Remote Sensing Symposium, IGARRS'99, vol. 4, pp. 2078-2080, Hamburg, Germany, June 28-July 2,1999

[104] A. Schroth, A. Hornbostel, "Utilization of the first three Stokes parameters for the determination of precipitation characteristics", Proc. 1998 IEEE Int. Geosci. Remote Sensing Symposium, IGARRS'98, vol. 1, pp. 141-143, Seattle, Washington, USA, July 6-10, 1998

[105] I. S. Ashcraft, D. G. Long, "Azimuth variation in microwave backscatter over the Greenland ice sheet", Proc. 2001 IEEE Int. Geosci. Remote Sensing Symposium, IGARRS'01, vol. 4, pp. 1779-1781, Sydney, Australia, July 9-13, 2001

[106] I. S. Ashcroft, D. G. Long, "Observation and characterization of radar backscatter over Greenland", IEEE Trans. Geosci. Remote Sensing, vol. 43, no. 2, February 2005

[107] S. H. Yueh, S. V. Nghiem, R. Kwok, "Polarimetric emission from anisotropic media for passive remote sensing of sea ice", Proc. 1992 IEEE Int. Geosci. Remote Sensing Symposium, IGARRS'92, vol. 2, pp. 966-968, Houston, Texas, USA, May 26-29, 1992

[108] J. P. Hollinger, "Passive microwave measurements of sea surface roughness", IEEE Trans. Geosci. Electron., vol. GE-09, pp. 165-169, July 1971

[109] S. H. Yueh, R. Kwok, F. K. Li, S. V. Nghiem, and W. J. Wilson, “Polarimetric passive remote sensing of ocean wind vectors”, Radio Sci., vol. 29, no. 4, pp. 799-814, July-August 1994

[110] A. J. Gasiewski and D. B. Dundee, “Polarized microwave emission from water waves”, Radio Sci., vol. 29, no. 6, pp. 1449-1466, November-December 1994

[111] G. Pan, J. T. Johnson, “A numerical study of the modulation of short sea waves by longer waves”, IEEE Trans. Geosci. Remote Sensing, vol. 44, no. 10, pp. 2880-2889, October 2006

[112] J. R. Apel, “An improved model of the ocean surface wave vector spectrum and its effects on radar backscatter”, J. Geophys. Res., vol. 99, no. C8, pp. 16269-16291, August 1994

[113] R.L. Wagner, J. Song, and W.C. Chew, “Monte Carlo Simulation of Electromagnetic Scattering from Two-Dimensional Random Rough Surface”, IEEE Transactions on Antennas and Propagation, vol. 45, pp. 235-245, January 1997.

[114] M.Y. Xia, C.H. Chan, S.Q. Li, B. Zhang and L. Tsang, “An Efficient Algorithm for Electromagnetic Scattering from Rough Surfaces Using a Single Integral Equation and Multilevel Sparse-Matrix Canonical-Grid Method”, IEEE Transactions on Antennas and Propagation, vol. 51, no. 6, pp. 1142-1149, June 2003.

[115] J. R. Piepmeier, “Calibration of passive microwave polarimeters that use hybrid coupler-based correlators”, IEEE Trans. Geosci. Remote Sensing, vol. 42, no. 2, pp. 391-400, February 2004

[116] A. B. Tanner, W. J. Wilson, F. A. Pellerano, “Development of a high stability L-band radiometer for ocean salinity measurements”, Proc. 2003 IEEE Int. Geosci. Remote Sensing Symposium, IGARRS'03, vol. 2, pp. 1238-1240, Toulouse, France, July 21-25, 2003

[117] J. Rotboll, S. S. Sobjarg, N. Skou, ”L-band polarimetric correlation radiometer with subharmonic sampling”, Proc. 2001 IEEE Int. Geosci. Remote Sensing Symposium, IGARRS'01, vol. 4, pp. 1571-1574, Sydney, Australia, July 9-13, 2001

[118] T. J. Jackson, A. J. Gasiewski, A. Oldak, M. Klein, E. G. Njoku, A. Yevgrafov, S. Christiani, R. Bindlish, ”Soil moisture retrieval using the C-band polarimetric scanning radiometer during the Southern Great Plains 1999 experiment”, IEEE Trans. Geosci. Remote Sensing, vol. 40, no. 10, pp. 2151-2161, October 2002

[119] J. Lahtinen, M. Hallikainen, “A low-cost polarimetric radiometer for real time Stokes parameter measurement”, Proc. 1997 IEEE Int. Geosci. Remote

Sensing Symposium, IGARSS’97, vol. 4, pp. 1597-1599, Singapore, August 3-8, 1997

[120] J. R. Piepmeier, A. J. Gasiewski, “Polarimetric scanning radiometer for airborne microwave imaging studies”, Proc. 1996 IEEE Int. Geosci. Remote Sensing Symposium, IGARSS’96, vol. 2, pp. 1120-1122, May 27-31, Lincoln, Nebraska, USA, 1996

[121] P. Chang, P. W. Gaiser, K. St. Germain, L. Li, “Multi-frequency polarimetric microwave ocean wind direction retrievals”, Proc. 1997 IEEE Int. Geosci. Remote Sensing Symposium, IGARSS’97, vol. 2, pp. 1009-1011, Singapore, August 3-8, 1997

[122] J. Lahtinen, M. T. Hallikainen, “HUT fully polarimetric calibration standard for microwave radiometry”, IEEE Trans. Geosci. Remote Sensing, vol. 41, no. 3, March 2003

[123] N. Skou and B. Laursen, “Measurement of ocean wind vector by an airborne, imaging polarimetric radiometer”, Radio Sci., vol. 33, no. 3, pp. 669-675, May-June 1998

[124] V. S. Etkin, A. V. Kuzmin, M. N. Pospelov, A. I. Smirnov, V. V. Yakolev, ”The determination of sea surface wind and temperature with airborne radiometric data”, Proc. 1993 IEEE Int. Geosci. Remote Sensing Symposium, IGARSS’93, vol. 4, pp. 1622-1624, Tokyo, Japan, August 18-21, 1993

[125] A. V. Kuzmin and M. N. Pospelov, “Measurements of sea surface temperature and wind vector by nadir airborne microwave instruments in joint United States/Russia internal waves remote sensing experiment JUSREX'92”, IEEE Trans. Geosci. Remote Sensing, vol. 37, no.4, July 1999

[126] S. T. Brown, C. S. Ruf, D. R. Lyzenga, “An Emissivity-based wind vector retrieval algorithm for the WindSat polarimetric radiometer”, IEEE Trans. Geosci. Remote Sensing, vol. 44, no. 3, March 2006

[127] M. N. Pospelov, “Surface wind speed retrieval using passive microwave polarimetry: The dependence on atmospheric stability”, IEEE Trans. Geosci. Remote Sensing, vol. 34, pp. 1166-1171, September 1996

[128] R. D. West, S. H. Yueh, “Atmosphere effects on the wind retrieval performance of satellite radiometers”, Proc. 1996 IEEE Int. Geosci. Remote Sensing Symposium, IGARRS'96, vol. 3, pp. 1727-1729, Lincoln, Nebraska, USA, May 27-31, 1996

[129] L. A. Rose, W. E. Asher, S. C. Reising, P. W. Gaiser, K. M. St. Germain, D. J. Dowgiallo, K. A. Horgan, G. Farquharson, E. J. Knapp, “Radiometric Measurements of the Microwave Emissivity of Foan”, IEEE Trans. Geosci. Remote Sensing, vol. 40, no. 12, pp. 2619-2625 , December 2002

[130] S. Padmanabhan, S. C. Reising, W. E. Asher, L. A. Rose, P. W. Gaiser, "Effects of foam on ocean surface microwave emission inferred from radiometric observations of reproducible breaking waves", IEEE Trans. Geosci. Remote Sensing, vol. 44, no. 3, March 2006

[131] L. A. Rose, J. P. Bobak, P. W. Gaiser, M. D. Anguelova, D. J. Dowgiallo, W. E. Asher, "Azimuthal variation of the emissivity of foam from C and X band polarimetric measurements", Proc. 2006 MicroRad 2006, pp. 125-130, San Juan, Puerto Rico, February 28-March 3, 2006

[132] J. P. Bobak, D. J. Dowgiallo, N. R. McGlothlin, T. E. von Rentzell, "Calibration and validation activities of the airborne polarimetric microwave imaging radiometer", Proc. 2004 IEEE Int. Geosci. Remote Sensing Symposium IGARSS'04, vol. 5, pp. 3286-3287, Anchorage, Alaska, USA, September 20-24, 2004

[133] J. P. Bobak, D. J. Dowgiallo, T. E. von Rentzell, N. R. McGlothlin, "Satellite calibration and validation utilizing the airborne polarimetric microwave imaging radiometer (APMIR)", Proc. 2005 MTS/IEEE OCEANS 2005, pp. 352-354, September 17-23, 2005

[134] J. T. Johnson, "An efficient two-scale model for the computation of thermal emission and atmospheric reflection from the sea surface", IEEE Trans. Geosci. Remote Sensing, vol. 44, no. 3, March 2006

[135] L. Tsang, C.H. Chan and K. Pak, "Monte Carlo Simulation of Large-Scale Problems of Random Rough Surface Scattering and Applications to Grazing Incidence with the BMIA/canonical Grid Method", IEEE Transactions on Antennas and Propagation, vol. 43, pp. 851-859, August 1995.

[136] K. Pak, L. Tsang, J.T. Johnson, "Numerical simulations and backscattering enhancement of electromagnetic waves from two-dimensional dielectric random rough surfaces with the sparse-matrix canonical grid method", J. Opt. Soc. Am. A, vol. 14, no. 7, pp. 1515-1529, July 1997

[137] L. Zhou, L. Tsang, V. Janshyala, Q. Li, C.H. Chan, "Emissivity simulations in passice microwave remote sensing with 3-D numerical solutions of Maxwell equations", IEEE Trans. Geosci. Remote Sensing, vol. 42, no. 8, August 2004

[138] P. Wang, M. Y. Xia and L. Z. Zhou, "Analysis of scattering by composite conducting and dielectric bodies using the single integral equation method and multilevel fast multipole algorithm", Microwave and Optical Technology Letters, Vol. 48, No. 6, pp. 1055 - 1059, June 2006.

[139] Y. Juan, B. Shanker and L. C. Kempel, "Fast multipole augmented analysis of scattering from dielectric objects using the single integral equation", 20th Annual Review of Progress in Applied Computational Electromagnetics, April 19-23, Syracuse NY, USA, 2004.

[140] A. J. Poggio, E. K. Millar, “Integral equation solutions of three-dimensional scattering problems”, Computer Techniques for Electromagnetics, R. Mittra, Ed. New York: Pergamon, 1973.

[141] E. Marx, “Single integral equation for wave scattering”, J. Math Phys., vol. 23, pp. 1057-1065, 1982

[142] E. Marx, “Integral equation for scattering by a dielectric”, IEEE Trans. Antennas Propagat., vol. AP-32, pp. 167-172, Feb. 1984.

[143] J. R. Mautz, R. F. Harrington, “H-field, E-field and combined-field solutions for conducting bodies of revolution”, Archi Elecktronik Übertragungstechnik (AEU), Germany, vol. 32, pp. 157-164, 1978.

[144] Y. Saad, M.H. Schultz, "GMRES: A generalized minimal residual algorithm for solving nonsymmetric linear systems", SIAM J. Sci. Stat. Comput., vol. 7, no. 3, 856-869, 1986

[145] T. K. Sarkar, E. Arvas, S. M. Rao, ”Application of FFT and the conjugate gradient method for the solution of electromagnetic radiation from electrically large and small conducting bodies”, IEEE Trans. Ant. Propag., vol. AP-34, no. 5, May 1986

[146] X.-C. Nie, L.-W. Li, N. Yuan, “Precorrected-FFT Algorithm for Solving Combined Field Integral Equations in Electromagnetic Scattering”, J. of Electromagn. Waves and Appl., Vol. 16, No. 8, pp. 1171-1187, 2002

[147] T. Schmugge, P. E. O'Neill, and J. R. Wang, “Passive microwave soil moisture research”, IEEE Trans. Geosci. Remote Sensing, vol. 24, no. 1, pp. 12-22, 1986.

[148] H.-J. C. Blume, B. M. Kendall, and J. C. Fedors, “Measurement of ocean temperature and salinity via microwave radiometry”, Boundary-Layer Meteorology, vol. 13, pp. 295-308, 1978.

[149] J. Lemmetyinen, J. Uusitalo, K. Rautiainen, J. Kainulainen, N. Fabritius, M. Levander, V. Kangas, H. Greus, J. Pihlflyckt, A. Kontu, S. Kemppainen, M. Hallikainen and J. Lahtinen, “SMOS Calibration Subsystem”, Proc. 2006 IEEE Int. Geosci. Remote Sensing Symposium, IGARRS'06, vol. 5, pp. 2309-2312, Colorado, Denver, USA, July 31-August 4, 2006

[150] I. Corbella, F. Torres, A. Camps, N. Duffo, M. Vall-llossera, K. Rautiainen, M. Martín-Neira, A. Colliander, “Analysis of Correlation and Total Power Radiometer Front-Ends Using Noise Waves”, IEEE Trans. Geosci. Remote Sensing, vol. 43, no. 11, pp. 2452-2459, November 2005.

[151] S.W. Wedge and D.B. Rutledge, ``Wave techniques for noise modeling and measurement", IEEE Trans. Microw. Theory Tech., vol. 40, no. 11, pp. 2004-2012, November 1992.

[152] A. Colliander, “Noise Injection Radiometer Test Specifications and Requirements”, Master’s Thesis, Espoo, Finland: Helsinki University of Technology, 2002

[153] D. Le Vine, S. Abraham, “Galactic Noise and Passive Microwave Remote Sensing from Space at L-Band”, IEEE Trans. Geosci. Remote Sensing, vol. 42, no. 1, pp. 119-129, January 2004

[154] H. Bosma, “On the theory of linear noisy systems,” Doctoral Thesis, Eindhoven, The Netherlands: Technische Hogeschool Te Eindhoven, 1967.

[155] A. Colliander, S. Tauriainen, T. Auer, J. Uusitalo, M. Toikka, M. T. Hallikainen, ”Evaluation of in-orbit temperature variation on performance of MIRAS prototype noise injection radiometer”, Proc. 2004 IEEE Int. Geosci. Remote Sensing Symposium, IGARSS’04, vol. 2, pp. 781-784, Anchorage, Alaska, USA, September 20-24, 2004

[156] R. Vilaseca, “PMS linearity setup improvement”, Mier Comunicaciones, Spain, Project report: SMOS PLM Phase C/D - LICEF 3, SO-RP-MIER-LIC-0233-02, June 20, 2005

[157] A. Colliander, J. Suomela, L. Ruokokoski, V. Kangas, A. Aalto, J. Lahtinen, M. Hallikainen, ”Temperature variation compensation in engineering model of MIRAS reference radiometer”, Proc. 2005 IEEE Int. Geosci. Remote Sensing Symposium, IGARSS’05, vol. 8, pp. 5558-5561, Seoul, South-Korea, July 25-29, 2005

[158] T. Larsen, “A Survey of the Theory of Wire Grids,” IEEE Trans. Microwave Theory and Techniques, Volume 10, Issue 3, May 1962, pp. 191 - 201

[159] T. Manabe, A. Murk, “Transmission and Reflection Characteristics of Slightly Irregular Wire-Grids With Finite Conductivity for Arbitrary Angles of Incidence and Grid Rotation,” IEEE Trans. Antennas and Propagation, vol. 53, no. 1, January 2005.

[160] M. Hallikainen, M. Kemppinen, J. Pihlflyckt, I. Mononen, T. Auer, K. Rautiainen, and J. Lahtinen, “HUTRAD: airborne multifrequency microwave radiometer”, Proc. ESA Workshop on Millimetre Wave Technology and Applications: antennas, circuits and systems, Espoo, Finland, pp. 115-120, 1998.

[161] S. D. Smith, “Coefficients for sea surface wind stress, heat flux, and wind profiles as a function of wind speed and temperature,” J. Geophys. Res., vol. 93, no. C12, pp. 15467-15472, December 1988.

[162] P. Schluessel and H. Luthard, “Surface wind speeds over the North Sea from special sensor microwave/imager observations”, J. Geophys. Res., vol. 96, no. C3, pp. 4845-4853, 1991.

[163] M. Zhang and J. T. Johnson, “Comparison of modeled and measured second azimuthal harmonics of ocean surface brightness temperature”, IEEE Trans. Geosci. Remote Sensing, vol. 39, no. 2, February 2001

[164] R. J. Adams, N. J. Champagne, II, “A Numerical Implementation of a Modified Form of the Electric Field Integral Equation”, IEEE Trans. Ant. Propagat., vol. 52, no. 9, pp. 2262-2266, September 2004

[165] C. Schwab and W. L. Wendland, “On numerical cubatures of singular surface integrals in boundary element methods”, Numerische Mathematik, Vol. 62, pp. 343-369, 1992.

[166] S.C. Wu, M.F. Chen, and A.K. Fung, “Non-Gaussian Surface Generation”, IEEE Trans. Geosci. Remote Sensing, vol. 26, no. 6, pp. 885-888, November 1988

[167] F. Ling, C.F. Wang, and J.M. Jin, “Application of adaptive integral method to scattering and radiation analysis of arbitrarily shaped planar structures”, J. Electromagnetic Waves Appl., vol. 12, pp. 1021-1038, August 1998

[168] J. Jin, “The Finite Element Method in Electromagnetics”, 2nd Edition, John Wiley & Sons, Inc., New York, 2002

APPENDIX A: INTEGRAL EQUATION AND ADAPTIVE INTEGRAL METHOD

In this Appendix, first the integral operators for electromagnetic field are defined, then the treatment of the near term integration for the scattering problem is described, and finally, the basic idea of adaptive integral method (AIM) is presented.

A.1 Integral operators

The integral operators $\mathbf{K}_l$ and $\mathbf{D}_l$ are defined as (l=1,2):

$$\mathbf{K}_l\left(\vec{F}\right)\!\left(\vec{r}\right)=\int_S \nabla G_l(\vec{r},\vec{r}\,')\times\vec{F}(\vec{r}\,')dS'\,, \tag{A-1}$$

and

$$\mathbf{D}_l\left(\vec{F}\right)\!\left(\vec{r}\right)=k_l^2\int_S G_l(\vec{r},\vec{r}\,')\vec{F}(\vec{r}\,')dS'+\nabla\int_S G_l(\vec{r},\vec{r}\,')\nabla_S'\cdot\vec{F}(\vec{r}\,')dS'\,, \tag{A-2}$$

where

$$G_l(\vec{r},\vec{r}\,')=\frac{e^{ik_l|\vec{r}-\vec{r}\,'|}}{4\pi|\vec{r}-\vec{r}\,'|}\,, \tag{A-3}$$

is the homogeneous space Green's function of domain D (so that $\vec{r}$ is the location where the field is evaluated due to the current distribution at $\vec{r}\,'$); $k_l=\omega\sqrt{\mu_l\varepsilon_l}$ is the wave number, and $\nabla_S'\cdot$ denotes the surface divergences with respect to the primed coordinates.

A.2 Integration of the near terms

In this Appendix the application of the Gauss divergence theorem in order to avoid the integration over the singularity is introduced. The Gauss divergence theorem can be used to transform the surface integral to a boundary integral, which eliminates the integration over the singularity for the near terms of $\overline{\overline{W}}$, as is shown next.

Writing only the essential part of an element of $\overline{\overline{W}}$ and dividing it into tangential and normal components yields (see Figure A-1):

$$\int_{l_i}\int_{T_j}\nabla G_1\cdot\hat{l}_i\,ds\,dl=\int_{l_i}\int_{T_j}(\nabla_T+\nabla_N)G_1\cdot\hat{l}_i\,ds\,dl\,. \tag{A-4}$$

Since the normal component of the two triangles and the direction of the edge are perpendicular to each other, the normal component vanishes. Now, by applying the Gauss divergence theorem gives:

$$\int_{l_i}\int_{T_j}\nabla_T G_1\cdot\hat{l}_i\,ds\,dl=-\int_{l_i}\oint_{C_j}G_1\left(\hat{l}_i\cdot\hat{m}_j\right)dc\,dl=-\int_{l_i}\sum_{q=1}^{4}\oint_{C_j^q}G_1\left(\hat{l}_i\cdot\hat{m}_j^q\right)dc\,dl\,. \tag{A-5}$$

where $\hat{m}_j^q$ is a unit vector of the outer normal of the boundary C_j^q of jth basis function (see Figure A-1). The singularity withholding edge is left out, since

$$\hat{m}^{+}\cdot\hat{l}_{i}=\hat{m}^{-}\cdot\hat{l}_{i}=0\,, \tag{A-6}$$

as is evident from Figure A-1. This way the integration of these terms becomes very accurate.

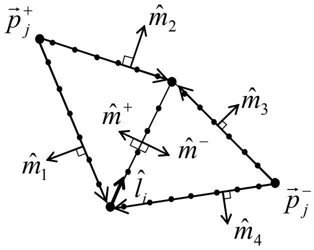

Figure A-1. Integration of an element of W, which has the same basis and testing function. The integration over the singularity is overcome by applying Gauss divergence theorem.

When the edge of the testing function is one of the other edges of the triangles of an RWG basis function, the method can also be applied to the elements of $\overline{\overline{K}}$. In this case, the tangential component of the triangle vanishes directly, and the normal component through the Gauss theorem, since $\hat{l}\times\vec{f}$ is in the direction of the normal of the triangle. This way the integral over the triangle, where the testing edge resides, vanishes altogether.

A.3 Basic idea of Adaptive Integral Method

Conventionally, adaptive integral method (AIM) is applied to a discretization using Galerkin method (same basis and testing function). Here, AIM is applied on the discretization with different basis and testing functions, which, however, does not cause any extra problems. In this Section, the formulation is presented explicitly.

Figure A-2 shows a schematic diagram of a piece of a surface. The rectangular grid is the grid laid out for the AIM and the triangles denote the actual surface discretized using triangular RWG basis functions. The height of the surface varies in *z*-direction. The AIM grid is positioned at *z*-axis so that it is at the mean level of the surface height.

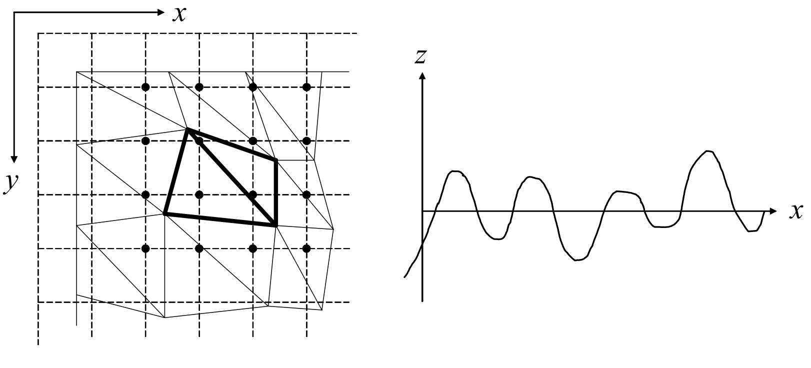

Figure A-2. Piece of the surface divided into triangle shaped patches and the grid for AIM. The dots indicate the grid points for which the coefficients are solved in order to determine the translated basis function of the highlighted RWG-basis function.

The idea of the AIM is as follows [76],[168]: consider matrix element of MOM equation with a basis function ψ_j and a testing function φ_i having the following form:

$$z_{ij} = \int_{l_i}\iint_{T_j} \psi_j(\vec{r}) G(\vec{r},\vec{r}\,') \varphi_i(\vec{r}\,') ds' dl \,, \tag{A-7}$$

where G is the Green's function; see Equation (A-3). The basis and testing functions can be translated from a triangular grid onto a uniform rectangular grid by approximating them with a combination of the Dirac delta functions on a rectangular grid as follows

$$\psi_j(\vec{r}) \approx \hat{\psi}_j(\vec{r}) = \sum_{u=1}^{(M+1)^2} Q_{ju} \delta(\vec{r} - \vec{r}_u), \tag{A-8}$$

where Q_{ju} is the expansion coefficient for the basis function $\psi_j(\vec{r})$, M is the expansion order and $\vec{r}_u$ is the vector for the grid location. The matrix element z_{ij} can now be approximated with the translated basis and testing functions, Q_j and U_i, as follows

$$\hat{z}_{ij} = \sum_{u=1}^{(M+1)^2} \sum_{v=1}^{(M+1)^2} Q_{ju} \delta(\vec{r}_u, \vec{r}_v) U_{iv} \,, \tag{A-9}$$

to which FFT can be applied due to the uniform distribution of calculation points along the geometry.

One way of solving the translated functions is based on the multipole moment approximation. The goal is that the translated function produces the same multipole moments as those of the original basis (or testing) function. This can be solved from the following [168]

$$\sum_{u=1}^{(M+1)^2} (x_u - x_0)^{q1} (y_u - y_0)^{q2} Q_{ju} = \iint_S \psi_j(\vec{r})(x_u - x_0)^{q1} (y_u - y_0)^{q2} dS, \tag{A-10}$$
$$0 \le q_1, q_2 \le M,$$

where the reference point $\vec{r}_0 = (x_0, y_0)$ is chosen as the center of the basis (or testing) function. Note that this approach does not directly apply to the matrices $\overline{\overline{W}}$ and $\overline{\overline{K}}$ including the derivates of the Green's function. Application of AIM to these terms is considered in Section 5.2.2.

In Figure A-2, the dots indicate the grid points for which the coefficients are solved in order to determine the translated function of the highlighted RWG-basis function. In the case of the figure, M = 3 yielding 16 coefficients for each translated function. Note also that AIM can be applied only to the far interaction terms and the near terms have to be calculated with standard MoM.

APPENDIX B: ADDITIONAL DETAILS OF THE REFERENCE RADIOMETER

The purpose of this Appendix is to present the complete list of the reference planes of the reference radiometer, or the NIR, the plane transformations needed in modulus term calculations and also the operational equations derived for the prototype of the NIR.

B.1 Reference planes

Figure B-3 shows the front-end connections and reference planes of the space flight model of the NIR. Some of these planes are accessible only before certain step of the integration and some non-accessible altogether. Table B-1 lists the planes and their descriptions.

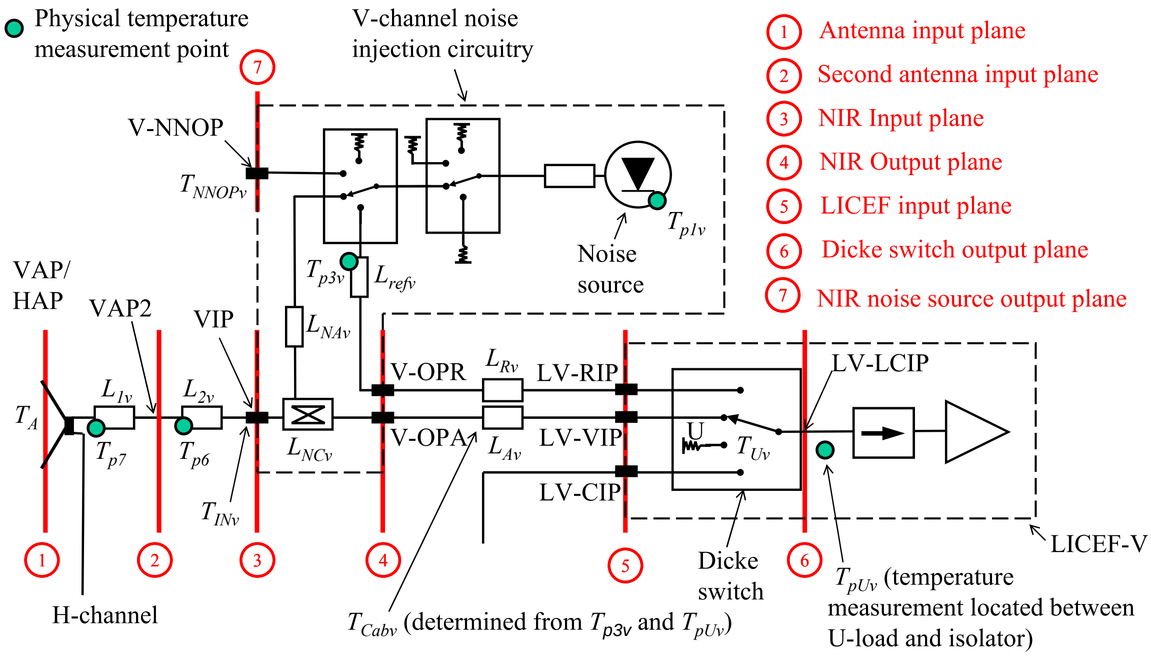

Figure B-3. The reference planes and connections of the NIR Flight Model. See also Table B-1.

Table B-1. The reference planes of the NIR.

Acronym	Plane	Description
VAP	V-pol Antenna Plane	V-input to the antenna patch
VAP2	V-pol Antenna Plane 2	V-input to the intermediate layer[1]
VIP	V-pol Input plane	V-channel: antenna input connector
V-OPR	V-pol R-Output plane	V-channel: output reference connector
V-OPA	V-pol antenna output plane	V-channel: output connector
LV-RIP	LICEF-V, R-Input Plane	R input in LICEF-V (reference branch)
LV-VIP	LICEF-V, V-Input Plane	V input in LICEF-V (antenna branch)
LV-CIP	LICEF-V, C-Input Plane	C input in LICEF-V (CAS input)
LV-LCIP	LICEF-V, Common Input Plane	LICEF-V Switch Output[2]
HAP	H-pol Antenna Plane	H-input to the antenna patch
HAP2	H-pol Antenna Plane 2	H-input to the intermediate layer[1]
HIP	H-pol Input plane	H-channel: antenna input connector
H-OPR	H-pol R-Output plane	H-channel: output reference connector
H-OPA	H-pol antenna output plane	H-channel: output connector
LH-RIP	LICEF-H, R-Input Plane	R input in LICEF-H (reference branch)
LH-HIP	LICEF-H, H-Input Plane	H input in LICEF-H (antenna branch)
LH-CIP	LICEF-H, C-Input Plane	C input in LICEF-H (CAS input)
LH-LCIP	LICEF-H, Common Input Plane	LICEF-H Switch Output[2]

1) Non-accessible point

2) Non-accessible point after LICEF integration.

B.2 Plane transformation of injection and receiver noise temperatures

For the calculation of the modulus terms of the blind correlation, the injection and receiver noise temperatures need to be known at the antenna input plane.

In Equation (4-11), the noise injection temperature is solved at the input of the controller (VIP or HIP in previous Section) for the determination of the antenna temperature. This is transferred to the antenna input plane (VIP or HIP in previous Section) using the losses of the antenna and its equivalent noise temperatures as follows (e.g. [3]):

$$T''_{NA} = L_1 L_2 T_{NA} - L_1 T_{L2} - T_{L1}, \tag{B-1}$$

where L_1 is the loss of the antenna patch; L_2 is the loss of the intermediate layer of the antenna; T_{NA} is the injection noise temperature at the controller input, and the equivalent noise temperatures of the antenna losses are solved as (e.g. [3]):

$$T_{L1} = (L_1 - 1)T_{p7}, \tag{B-2}$$

in which T_{L1} is the equivalent noise temperature due to loss L_1, and T_{p7} is the physical temperature associated with L_1. T_{L2} is solved correspondingly using L_2 and T_{p6}.

During the NIR calibration, the warm, T_{warm}^{CIP}, and hot, T_{hot}^{CIP}, noise levels of CAS are used to solve the receiver temperature at the CAS input plane (LV- or LH-CIP in previous Section). This is done using the voltage output (PMS) of the NIR in LICEF-LC and LICEF-LC2 modes, yielding the following voltages: v_1 and v_2 corresponding to the warm and hot level, respectively, when IF-attenuator is off, and v_3 and v_4 corresponding to the warm and hot level, respectively, when the IF-attenuator is on.

First the receiver noise temperature is solved at CAS input plane using the so-called four-point method (introduced in [98] and explained e.g. in [99]):

$$T_{rec}^{CIP} = \frac{aT_{warm}^{CIP} - T_{hot}^{CIP}}{1-a}, \tag{B-3}$$

where

$$a = \frac{v_2 - v_{off}}{v_1 - v_{off}}, \tag{B-4}$$

in which

$$v_{off} = \frac{v_2 v_3 - v_1 v_4}{(v_2 - v_4) - (v_1 - v_3)}. \tag{B-5}$$

Now, using the S-parameters of the LICEF front-end, obtained in the LICEF ground calibration campaign, the receiver noise temperature can be transferred to the LICEF input of the antenna branch (LV-VIP or LH-HIP in previous Section):

$$T_{rec}^{A} = \frac{|S_{LA}|^2}{|S_{LC}|^2} T_{rec}^{CIP} + \left(\frac{|S_{LA}|^2}{|S_{LC}|^2} - 1 \right) T_{pU}, \tag{B-6}$$

where S_{LA} and S_{LC} are the S21-parameter of the antenna branch and CAS paths of the LICEF front-end switch, respectively, and T_{pU} is the physical temperature of the LICEF front-end. Using the losses and equivalent noise temperatures of the antenna branch from LICEF input to the antenna input (VAP or HAP in previous Section) and Friis' formula (e.g. [3]), the receiver noise temperature at the antenna plane can be solved:

$$T_{rec} = T_{L1} + L_1 T_{L2} + L_1 L_2 T_{LNC} + L_1 L_2 L_{NC} T_{LA} + L_1 L_2 L_{NC} L_A T_{rec}^{A}, \tag{B-7}$$

where L_{NC} and L_A are the losses of the NIR controller and the cable between the controller and LICEF, respectively, and the equivalent noise temperatures of these sections are solved as shown in Equation (B-2) and physical temperatures of the controller, T_{p3}, and cable T_{cab}, see Equation (4-10).

B.3 Operational equations for the prototype

This Section presents the operational equations used for the prototype of the reference radiometer. The equations of the space flight model are shown in Section 4.1.

Equations for antenna temperature measurement and calibration

The equation for antenna temperature is derived starting from the balancing equation of the NIR-A mode as follows: the balancing equation can be written as

$$T_U = \tau T_{A|ON}^{LCIP} + (1-\tau) T_{A|OFF}^{LCIP} , \tag{B-8}$$

where T_U is the noise temperature of the internal load, $T_{A|ON}^{LCIP}$ is the antenna temperature at the receiver input when the noise injection is on, and $T_{A|OFF}^{LCIP}$ is the antenna temperature at the input of the receiver when the noise injection is off. The antenna temperature at the input of the receiver can be written as

$$T_A'' = \frac{T_A' + T_{N2}'}{L_{NC}} + \left(1 - \frac{1}{L_{NC}}\right) T_{p5} , \tag{B-9}$$

where T_A' is the antenna temperature at the input of the directional coupler, T_{N2} is the injection noise in the antenna branch, L_{NC} is the loss of the directional coupler, and T_{p5} is the physical temperature of the directional coupler. The antenna temperature at the input of the directional coupler can be written as

$$T_A' = \frac{T_A}{L_A} + \left(1 - \frac{1}{L_A}\right) T_{p5} , \tag{B-10}$$

where T_A is the antenna temperature and L_A is the loss of the connection from the antenna to the coupler. The injection noise in the antenna branch is calculated as

$$T_{N2}' = \frac{T_{N2} - T_A'}{F_{NC}} , \tag{B-11}$$

where T_{N2} is the injection noise at the injection input of the directional coupler and F_{NC} is the coupling factor of the directional coupler. When the noise injection is on, T_{N2} can be written as

$$T_{N2|ON} = \frac{T_N}{L_{NA} L_{ON}} + \left(1 - \frac{1}{L_{NA} L_{ON}}\right) T_{p3} , \tag{B-12}$$

where T_N is the output of the noise source, L_{NA} is the attenuation of the attenuator in the injection channel, and T_{p3} is its physical temperature and L_{ON} is the insertion loss of the switch controlling the noise injection. When the noise injection is off, T_{N2} can be written as

$$T_{N2|OFF} \approx T_{p3} , \tag{B-13}$$

since the effect of the noise leaking through the switch (L_{OFF}) and the directional coupler can be considered negligible.

Now, using the balancing equation and the results above, an equation for the antenna temperature can be obtained:

$$T_A = a\tau + b , \tag{B-14}$$

where

$$a = \frac{L_A}{1-F_{NC}}\left(\frac{T_N + T_{p3}}{L_{NA}L_{ON}}\right), \tag{B-15}$$

and

$$b = \frac{F_{NC}L_A}{F_{NC}-1}\left\{L_{NC}T_U - \frac{T_{p3}}{F_{NC}} - \left[\left(1+\frac{1}{F_{NC}}\right)\left(1-\frac{1}{L_{NC}}\right) + L_{NC} - 1\right]T_{p5}\right\}. \tag{B-16}$$

And the noise injection temperature is retrieved as:

$$T_N = L_{NA}L_{ON}\left[\frac{F_{NC}-1}{L_A}\left(b - T_A\right)\right]\frac{1}{\tau} - T_{p3}. \tag{B-17}$$

Equations for NDN temperature measurement and calibration

The equation for NDN noise temperature measurement is derived starting from the balancing equation of the NIR-R mode as follows: the balancing equation can be written as

$$T_{NDN} = \tau\, T^{LCIP}_{ref|ON} + \left(1-\tau\right)T^{LCIP}_{ref|OFF}, \tag{B-18}$$

where the noise temperature of the reference branch when the noise injection is on is defined as

$$T''_{ref|ON} = \frac{T_N}{L_{ON}L_{ref}} + \left(1 - \frac{1}{L_{ON}L_{ref}}\right)T_{p3}, \tag{B-19}$$

and the noise temperature of the reference branch when the noise injection is off is defined as

$$T''_{ref|OFF} = \frac{T_N}{L_{OFF}L_{ref}} + \left(1 - \frac{1}{L_{OFF}L_{ref}}\right)T_{p3}, \tag{B-20}$$

in which T_N is the output of the noise source, L_{OFF} is the isolation of the noise injection switch, and L_{ref} is the attenuation of the attenuator in the reference branch. Now, using the balancing equation and the expressions above the noise temperature level can be determined as:

$$T_{NDN} = \tau\left(\frac{T_N - T_{p3}}{L_{ON}L_{ref}} + T_{p3}\right) + \left(1-\tau\right)\left(T_{p3} + \frac{T_N - T_{p3}}{L_{OFF}L_{ref}}\right). \tag{B-21}$$

For the calibration of the NIR-R mode, first the noise level in the antenna branch during the noise injection is solved using the NIR-A mode. The balancing equation of the NIR-A mode can be written as

$$T_U = \tau\, T_{Aref} + \left(1-\tau\right)T''_{A|OFF}, \tag{B-22}$$

where T_{Aref} is the noise level in the antenna branch when the noise injection is on, and $T''_{A|OFF}$ is the same as in Equation (B-8). From this it yields

$$T_{Aref} = \frac{T_U}{\tau} + \left(1 - \frac{1}{\tau}\right)T''_{A|OFF}, \tag{B-23}$$

from which it follows:

$$T_{Aref} = \frac{T_U}{\tau} + \left(1 - \frac{1}{\tau}\right)\left\{\frac{F_{NC} - 1}{F_{NC} L_{NC}}\left[\frac{T_A}{L_A} + \left(1 - \frac{1}{L_A}\right)T_{p5}\right] + \frac{T_{p3}}{F_{NC} L_{NC}} + \left(1 - \frac{1}{L_{NC}}\right)T_{p5}\right\}, \tag{B-24}$$

Now, the noise source output can be determined using REF-CAL mode, the balancing equation of which can be written as

$$T_{Aref} = \tau\, T_{ref|ON}^{LCIP} + (1 - \tau) T_{ref|OFF}^{LCIP}\,, \tag{B-25}$$

which yields

$$T_{Aref} = \tau\left(\frac{T_N - T_{p3}}{L_{ON} L_{ref}} + T_{p3}\right) + (1 - \tau)\left(T_{p3} + \frac{T_N - T_{p3}}{L_{OFF} L_{ref}}\right), \tag{B-26}$$

from which T_N can be solved yielding:

$$T_N = \frac{L_{ref}}{1/L_{ON} + (1/\tau - 1)1/L_{OFF}}\left\{\frac{T_{Aref} - T_{p3}}{\tau} + \frac{T_{p3}}{L_{ref}}\left(\frac{1}{L_{ON}} + \frac{1 - \tau}{\tau\, L_{OFF}}\right)\right\}, \tag{B-27}$$

Note that the same noise source output T_N is solved in two ways for both NIR-A and NIR-R modes separately. This is due to the fact that the accuracy in which the attenuations L_{NA} and *Lref* are known is limited. However, using noise source output for retrieving the antenna and NDN noise temperatures yields the best results despite the inaccuracy of the attenuations.